

A Global 86 GHz VLBI Survey of Compact Radio Sources

Sang-Sung Lee¹, Andrei P. Lobanov¹, Thomas P. Krichbaum¹, Arno Witzel¹, Anton Zensus¹, Michael Bremer², Albert Greve², and Michael Grewing²

ABSTRACT

We present results from a large 86 GHz global VLBI survey of compact radio sources. The main goal of the survey is to increase by factors of 3–5 the total number of objects accessible for future 3-mm VLBI imaging. The survey observations reach the baseline sensitivity of 0.1 Jy and image sensitivity of better than 10 mJy/beam. The total of 127 compact radio sources have been observed. The observations have yielded images for 109 sources, extending the database of the sources imaged at 86 GHz with VLBI observation by a factor of 5, and only 6 sources have not been detected. The remaining 12 objects have been detected but could not be imaged due to insufficient closure phase information. Radio galaxies are less compact than quasars and BL Lacs on sub-milliarcsecond scale. Flux densities and sizes of core and jet components of all imaged sources have been estimated using Gaussian model fitting. From these measurements, brightness temperatures have been calculated, taking into account resolution limits of the data. The cores of 70% of the imaged sources are resolved. The core brightness temperatures of the sources peak at $\sim 10^{11}$ K and only 1% have brightness temperatures higher than 10^{12} K. Cores of Intraday Variable (IDV) sources are smaller in angular size than non-IDV sources, and so yield higher brightness temperatures.

Subject headings: BL Lacertae objects: general — galaxies: active — galaxies: jets — quasars: general — radio continuum: galaxies — surveys

1. Introduction

Very long baseline interferometry (VLBI) at millimeter wavelengths offers the best tool for imaging compact radio structures on scales of several dozens of microarcseconds. The first detection of single-baseline interference fringes in an 89 GHz (3.4 mm) VLBI observation was reported by Readhead et al. (1983), demonstrating the feasibility of 3-mm-VLBI. After that, many VLBI observations at 86 GHz have been made, probing the most compact regions in active galactic nuclei (AGN). However, the number of objects detected and imaged at 86 GHz remained small, compared with the number of objects imaged with VLBI at lower frequencies.

¹Max-Planck-Institut für Radioastronomie, Auf dem Hügel 69, 53121 Bonn, Germany

²Institut de Radio Astronomie Millimétrique, 300 rue de la Piscine, 38406 Saint Martin d'Hères, France

Sensitive VLBI observations at 86 GHz have been made for several sources, including 3C 111 (Doeleman & Claussen 1997), 3C 454.3 (Krichbaum et al. 1995, 1999; Pagels et al. 2004), NRAO 150 (Agudo et al. 2007), NRAO 530 (Bower et al. 1997), M87 (Krichbaum et al. 2006), 3C 273 and 3C 279 (Attridge 2001). In order to increase the number of objects imaged at 86 GHz, four detection and imaging surveys were conducted during the 1990s, with a total of 124 extragalactic radio sources observed (see Beasley et al. 1997; Lonsdale et al. 1998; Rantakyro et al. 1998; Lobanov et al. 2000). In these surveys, fringes were detected of 44 objects, but only 24 radio sources have been successfully imaged. Table 1 gives an overview of these surveys. The low detection and imaging rates of the previous 86 GHz surveys were caused by the relatively poor baseline sensitivities, small numbers of telescopes and short observing times.

The results of the survey of a larger number of sources can be used to investigate the innermost region of compact jets and to observationally test inner jet models (Marscher 1995): accelerating and decelerating jet models. In the accelerating jet model, the jet accelerates hydrodynamically from the base of the jet, and as the internal energy of the jet plasma is converted into the kinetic energy of bulk flow, the jet Lorentz factor increases along the jet. In this model, an ultra relativistic neutral beam is generated from the central engine and then the neutrons decay into protons and electrons which form a relativistically flowing plasma. In the decelerating jet model, the central engine produces a highly collimated beam of ultra relativistic electron-positron pair plasma that scatters photons produced outside the jet (particle cascade). The scattered photons emit X-rays and γ -rays, which decelerates the beam and so decreases the Lorentz factor along the jet.

The theoretical prediction from the jet models leads to the fact that the intensity profiles along the jet are different from each other and have a distinctive shape in each of these models. The resulting brightness temperature can be used to probe the difference. The intrinsic brightness temperature of a distribution of observed brightness temperatures can be determined from a statistical modeling (Lobanov et al. 2000). By estimating the brightness temperature at several frequencies (e.g., 15 GHz, 43 GHz, and 86 GHz) and determining the intrinsic brightness temperatures, we would be able to constrain the physical conditions (e.g., dynamics and compositions) of the innermost region of the compact sources. Moreover the dependence of the intrinsic brightness temperatures on the observing frequencies will tell about the feasibility of VLBI at higher frequencies (e.g., 150 GHz, 215 GHz, etc).

A large global 86 GHz VLBI survey of compact radio sources was carried out from 2001 October to 2002 October using the Coordinated Millimeter VLBI Array (CMVA) (Rogers et al. 1995), which is succeeded by the Global Millimeter VLBI Array (GMVA)¹. The main aim of this VLBI survey is to increase the total number of objects accessible for future 3 mm-VLBI imaging by factors of 3–5, and to provide the database for the subsequent statistical modeling in order to test the inner jet models.

¹See <http://www.mpifr-bonn.mpg.de/div/vlbi/globalmm/index.html>.

2. Observation

2.1. Source Selection

The source selection of this survey is based on the results from the VLBI surveys at 22 GHz (Moellenbrock et al. 1996) and 15 GHz (Kellermann et al. 1998), and on flux density measurements from the multi-frequency monitoring programs at Metsähovi at 22, 37, and 86 GHz (Teraesranta et al. 1998) and at Pico Veleta at 90, 150, and 230 GHz (Ungerechts, priv. comm.). Using these databases, we selected the sources with an expected flux density above 0.3 Jy at 86 GHz. We excluded some of the brightest sources already imaged at 86 GHz, and focused on those sources which had not been detected or imaged in the previous surveys. Objects in the southern sky with low declinations ($\delta \leq -40^\circ$) were rejected, in order to optimize the uv -coverage of the survey data.

According to the aforementioned selection criteria, a total of 127 compact radio sources was selected and observed, consisting of 88 quasars, 25 BL Lac objects, 11 radio galaxies, 1 star (Cyg X-3), and 2 unidentified sources. Table 2 lists the general information of the observed sources, with the columns corresponding to (1) source, (2) name, (3) epoch, (4) Right Ascension (J2000), (5) Declination (J2000), (6) status, (7) redshift, (8) optical class, (9) optical magnitude, and (10) total flux density $S_{86\text{GHz}}$. In Figure 1, the sky-distribution of the observed sources is shown.

2.2. Observational Strategy

The survey observations were conducted during three sessions of the Co-ordinated (global) millimeter VLBI array (CMVA/GMVA) on 2001 October, 2002 April and 2002 October, as summarized in Table 3. Table 3 shows the log of the survey observations, with the columns corresponding to (1) epoch, (2) code of each epoch, (3) bit rate, (4) frequency channels, (5) sampling mode, (6) total observing bandwidth, (7) number of sources, and (8) participating telescopes.

Table 4 lists the technical information of the participating telescopes, with the columns for (1) name, (2) abbreviation of the telescope name, (3) diameter, (4) typical zenith gain, (5) system temperature, (6) aperture efficiency, (7) typical zenith SEFD obtained from the formula, $SEFD = T_{\text{sys}}/G$, (8) baseline sensitivity on baseline to Pico Veleta, assuming a recording rate 256 Mbps and a fringe-fit interval of 30 seconds, and (9) 7σ detection threshold. The participation of the large and sensitive European antennas (the 100-m radio telescope at Effelsberg, the 30-m radio telescope at Pico Veleta, the 6×15 -m interferometer telescopes on Plateau de Bure) and the 8 VLBA¹ antennas available at 86 GHz resulted in a typical single baseline sensitivity of ~ 0.1 Jy and an image sensitivity of better than 10 mJy beam^{-1} .

¹The Very Long Baseline Array (VLBA) is an instrument of the National Radio Astronomy Observatory, which is a facility of the National Science Foundation operated under cooperative agreement by Associated Universities, Inc.

Every source in the sample was observed for 3-4 scans of 7-minute duration (*snapshot* mode). Although the *uv*-coverage of such an experiment limits the dynamic range and structural sensitivity of images, the large number of the participating antennas gives a sufficient *uv*-coverage of the sources at low and high declinations (Figure 2). The data were recorded either with 128-MHz or 64-MHz bandwidth using the MkIV VLBI system with 1- and 2-bit sampling adopted at different epochs. The observations were made in lefthand circular polarization (LCP). Three to four scans per hour were recorded, using the time between the scans for antenna focusing, pointing and calibration. The data were correlated using the MkIV correlator of the Max-Planck-Institut für Radioastronomie (MPIfR) in Bonn (Alef & Müskens 2001).

3. Data Processing

In this section, we describe the post-correlation processing of the 3 mm-VLBI survey datasets. Fringes were searched in two steps using HOPS (Haystack Observatory Postprocessing System) and AIPS (The NRAO Astronomical Image Processing System). In the first step, the HOPS task *fourfit* was used to precisely determine phase-residuals. The first *fourfit* was run with a wide search window (e.g. a width of 1 μ sec for singleband delay, 2 μ sec for multiband delay and 500 psec sec^{-1} for delay rate) centered at zero in delay. Since the *fourfit* produces baseline-based fringe solutions, the mean and standard deviation of the detected fringe solutions on each baseline were estimated and served as the offset and width of the search window for the second *fourfit*. The detected fringe solutions from the second run were used to interpolate the offset of the singleband delay for non-detected scans. In the final run of *fourfit*, an *interpolated* search window was used with a width of 0.02 μ sec for the singleband delay and centered at the offset interpolated for each non-detected scan. After this first step of the fringe search, the total number of fringe detections for the survey data was improved by up to 20%. In the second step of the fringe search, the baseline-based fringe solutions were imported into AIPS using a modified AIPS task MK4IN (Alef & Graham 2002). We then made an antenna-based fringe fit to the data using the AIPS task FRING. Pico Veleta (PV) was chosen as reference antenna for most of the data. When PV was not available, Fort Davis (Fd) was selected as an alternative reference antenna. The antenna-based fringe fitting was done with the solution interval of 7 minutes in order to achieve higher signal-to-noise ratio. Fringe solutions for strong sources were used to define coarse search windows for the fringe solutions for nearby weaker sources. With the fringe fit of *fourfit* and FRING, 121 out of 127 observed sources have yielded fringe detections with $\text{SNR} \geq 6$. Figure 3 shows the SNR distribution of the fringe detection in the entire survey data. Only 6 sources (0710+439, 1458+718 (3C 309.1), 1749+701 (4C 09.57), 2021+614, 2030+407 (Cyg X-3), and 2031+405 (MWC 349)) are not detected. The highest SNRs of 425 is measured on the “Pico Veleta–Plateau de Bure” baseline for 1741-038 and the “Effelsberg-Pico Veleta” baseline for 1633+382.

The fringe fitted data were amplitude calibrated using regular measurements of the system temperatures and antenna gains and the weather information for each station made during the

observations. Where possible, time-dependent factors in the antenna power gains were accounted for by applying atmospheric opacity corrections. The AIPS task APCAL was used to calibrate the amplitudes. As a check of the accuracy and consistency of the amplitude calibration, we have investigated (independently for each of the detected sources) the calibrated visibility amplitudes using the best fit Gaussian component models obtained from the data (the corresponding models are given in Table 7). For each of the sources, the antenna gains were allowed to be scaled by a constant factor so as to optimize the fit by the Gaussian model.

The obtained corrections are within 20% for most of sources, which is also reflected in the average correction factors listed in Table 5. On average, the gain factors for Pico Veleta, Onsala, North Liberty, Owens Valley, and Los Alamos remained within 10% in all three observing sessions. The average gains for Effelsberg did not change much except for the session C. Fort Davis and Mauna Kea required average corrections by more than 20%. Time-dependent errors may still be present in the calibrated data. Therefore we expect overall calibration accuracy of $\sim 20\text{--}30\%$

From the phase- and amplitude-calibrated data, the images were made using the Caltech DIFMAP software (Shepherd et al. 1994). After averaging in frequency, the uv -data were averaged in time over 30 seconds and were edited for deviant data points.

The uv -data were then fitted with a simple Gaussian model. First, a single circular Gaussian component was applied to fit the data. In case that the single-component model did not represent the data satisfactorily, a multiple-component model was applied. Self-calibration and CLEAN deconvolution were applied to produce final images of the detected sources.

The noise in the final image can be expressed quantitatively by the quality ξ_r of the residual noise. Suppose that a residual image has an rms σ_r and the maximum absolute flux density $|s_r|$. For Gaussian noise with a zero mean, the expectation of s_r is

$$|s_{r,\text{exp}}| = \sigma_r \left[\sqrt{2} \ln \left(\frac{N_{\text{pix}}}{\sqrt{2\pi}\sigma_r} \right) \right]^{1/2}, \quad (1)$$

where N_{pix} is the total number of pixels in the image. The quality of the residual noise is given by

$$\xi_r = s_r / s_{r,\text{exp}}. \quad (2)$$

When the residual noise approaches Gaussian noise, $\xi_r \rightarrow 1$. If $\xi_r > 1$, not all the structure has been adequately recovered; if $\xi_r < 1$, the image model has an excessively large number of degrees of freedom (Lobanov et al. 2006). The values of ξ_r of the images in the survey are presented in Column (14) of Table 6 and the distribution of them is shown in Figure 4, implying that the images adequately represent the structure detected in the visibility data.

The initial CLEAN cycles for the region around the core component are conducted with using natural weighting and without using uv -tapering. Once the CLEAN models satisfactorily fit the visibility at the longest baselines, uv -tapering was applied to the data on long baselines in order to recover faint emission further out from the core component. We did not modify the visibility

amplitudes, except for introducing an overall, time-constant gain correction factor wherever it was required for improving the agreement between the CLEAN model and the data. In addition to the check for the antenna gain corrections described above, we investigated the changes of the visibility amplitudes with and without introducing the time-constant gain correction factor, by using the correlated flux densities S_S , S_L , at the shortest and longest baselines B_S , B_L , (presented in Columns 4–7 in Table 6), for each of the sources. The correlated flux densities $S_{S,L}$ obtained after introducing the antenna gain corrections are compared with the flux densities S'_S and S'_L before the gain corrections. As shown in Figure 5 for the distributions of the ratios $R_S = S_S/S'_S$ and $R_L = S_L/S'_L$, the visibility amplitudes on the shortest and longest baselines for each of the sources were not changed for most of the sources during the hybrid imaging. For a small number of peculiar sources, the ratios of the visibility amplitudes fall within a range of 0.75–1.25. This analysis shows again that the amplitude calibration error of this survey observations is 20%–30%.

We introduce a zero-baseline flux to recover a faint structure in the extended region by adding a fake visibility at the point of origin in the Fourier plane (*uv*-plane). Since the shortest baseline of this survey observations is about 50–100 M λ , this may result in the faint structures of the extended regions appearing to be negative because the flux in every pixel of the map is offset by a small negative amount. The effect may be countered to some extent by adding the fake visibility at the origin of the *uv*-plane. The measured total flux density of each source S_{86} (listed Column 3 in Table 6) is used as the zero-baseline flux.

4. Estimating Parameters

In order to extract quantitative information from the images, circular Gaussian-component models were used to fit the self-calibrated *uv*-data yielding the following parameters: total and peak flux densities, positions, and sizes of each component. Uncertainties of the models were estimated, based on the signal-to-noise ratio (SNR) of detection of a given model fit component, using an analytical (first order) approximation (Fomalont 1999). The general fit parameters of a component in VLBI images of radio sources are S_{tot} - total flux density, S_{peak} - peak flux density, σ_{rms} - post-fit rms, d - size, r - radial distance (for jet components), θ - position angle (measured for jet components, with respect to the location of the core component). The uncertainties of the fit parameters can be estimated by adopting approximations given by Fomalont (1999):

$$\sigma_{\text{peak}} = \sigma_{\text{rms}} \left(1 + \frac{S_{\text{peak}}}{\sigma_{\text{rms}}} \right)^{1/2}, \quad \sigma_{\text{tot}} = \sigma_{\text{peak}} \left(1 + \frac{S_{\text{tot}}^2}{S_{\text{peak}}^2} \right)^{1/2}, \quad (3)$$

$$\sigma_d = d \frac{\sigma_{\text{peak}}}{S_{\text{peak}}}, \quad \sigma_r = \frac{1}{2} \sigma_d, \quad \sigma_\theta = \text{atan} \left(\frac{\sigma_r}{r} \right), \quad (4)$$

where σ_{peak} , σ_{tot} , σ_d , σ_r , and σ_θ are the uncertainties of total flux density, peak flux density, post-fit rms, size, and radial distance of a component, respectively. When the size, d , of a component was

determined, the resolution limits (Lobanov 2005) should be taken into account. So, the minimum resolvable size of a component in an image is given by

$$d_{\min} = \frac{2^{1+\beta/2}}{\pi} \left[\pi ab \ln 2 \ln \frac{SNR}{SNR - 1} \right]^{1/2}, \quad (5)$$

where a and b are the axes of the restoring beam, SNR is the signal-to-noise ratio, and β is the weighting function, which is 0 for natural weighting or 2 for uniform weighting. When $d < d_{\min}$, the uncertainties should be estimated with $d = d_{\min}$.

We use the results of the model fitting to estimate brightness temperatures of the core and jet components. The rest frame brightness temperature T_b of the emission region represented by a Gaussian component is

$$T_b = \frac{2 \ln 2}{\pi k} \frac{S_{\text{tot}} \lambda^2}{d^2} (1 + z), \quad (6)$$

where λ is the wavelength of observation, z is the redshift, and k is the Boltzmann constant. Practically, the brightness temperature can be calculated by simplifying (6):

$$T_b = 1.22 \times 10^{12} \frac{S_{\text{tot}}}{d^2 \nu^2} (1 + z) \text{ K}, \quad (7)$$

where the total flux density S_{tot} is measured in Jy, the size of the circular Gaussian component d in mas, and the observing frequency ν in GHz. If $d < d_{\min}$, then the lower limit of T_b is obtained with $d = d_{\min}$.

5. Results

Out of 127 sources, 109 sources have been imaged and model fitted. The first 3 mm-VLBI maps for 90 sources were made in this survey, increasing the number of sources ever imaged with 3 mm-VLBI observations up to 110.

In Figure 6, we present two plots and one contour map for each source at each epoch. In the left panel, the plot of the visibility amplitudes against uv -radius is shown. The corresponding uv -sampling distribution is given in the inset. The X-axis of the plot of the visibility amplitude represents the uv -radius which is the length of the baseline used to obtain the corresponding visibility point. The uv -radius is given in the units of $10^6 \lambda$, where λ is the observing wavelength. The Y-axis of the plot shows the amplitude of each visibility point (i.e., correlated flux density) in units of Jy. The uv -sampling distribution in the inset of the left panel describes the overall distribution of the visibility in the uv -plane, whose maximum scale equals that of the uv -radius. In the right panel, the contour map of each source is shown, with the X- and Y-axis in the units of milliarcsecond. For each source, the source name and the observation data are given in the upper left corner of the map. The lowest contour level is identified in the lower right corner of the map. The shaded ellipse represents the FWHM of the restoring beam in the image. In all of the images, the contours have a

logarithmic spacing and they are drawn at -1, 1, 1.4,...,1.4ⁿ of the lowest flux density level. For 12 sources (0133+476, 0149+218, 0212+735, 0234+285, 0238-084, 0316+413, 0355+508, 0415+379, 0430+052, 0716+714, 1928+738, and 2255-282), multi-epoch images are presented. Most sources are centered on the brightest component (VLBI core), but for some sources with a larger structure, we have shifted the center to fit the image in the box.

In Table 6, parameters of the images presented in Figure 6 are summarized. For each image, Table 6 lists the source name, the observing epoch, the total flux density, S_{86} , obtained from pointing and calibration measurements made at Pico Veleta during the observation, the correlated flux densities, $S_{S,L}$, measured on the shortest and longest baselines, $B_{S,L}$, the parameters of the restoring beam (the size of the major axis, B_a and the minor axis, B_b , and the position angle of the beam, B_{PA}), the total flux, S_t , the peak flux density, S_p , the off-source RMS, σ , and the quality of the residual noise in the image.

Table 7 lists the parameters of each model-fit component: the total flux, S_{tot} , peak flux density, S_{peak} , size, d , radius, r (only for jet components), position angle, θ (the location of the jet component with respect to the core component), and measured brightness temperature, T_b . For sources with multiple components, parameters of the core component are followed by those of jet components. For sources observed at multiple epochs, individual epochs are marked. The estimated uncertainties are given next to each parameter. The upper limits of size, d , and the lower limits of brightness temperature, T_b , are in italic with brackets.

6. Discussion

6.1. Source compactness

For all imaged sources, we discuss the source compactness, showing the distributions of the total flux density S_{86} , the CLEAN flux density S_{CLEAN} , and the correlated flux densities $S_{S,L}$ measured on the shortest and longest baselines, listed in Table 6. In Figure 7, we present the distributions of the flux densities and source compactness. The distribution of the total flux density S_{86} (*top left panel*) peaks at 1.3 Jy, and shows that almost all sources are brighter than 0.3 Jy, which corresponds to the flux limit of our source selection. The median value of the CLEAN flux density S_{CLEAN} (*middle left panel*) is 0.6 Jy and the peak of the distribution is around 0.5 Jy, indicating that much of the emission at 86 GHz from the compact radio sources is resolved out at milliarcsecond scales. The source compactness on milliarcsecond scales S_{CLEAN}/S_{86} is also shown in Figure 7 (*top right panel*). The median compactness on milliarcsecond scales of our sample is 0.51.

While the median correlated flux density at the longest baseline S_L is 0.22 Jy (*bottom left panel*), quite a few sources have considerable flux at long baselines (e.g., Pico Veleta and Kitt Peak). Among 95 sources whose correlated flux density can be measured at projected baselines longer than 2000 Mλ, 82 sources have a correlated flux density greater than 0.1 Jy. From the

distribution of the source compactness on sub-milliarcsecond scales S_L/S_S (*middle right panel*) we can see that most of the imaged sources are resolved. A few sources have a slightly greater flux density on the longest baseline than on the shortest baseline, since they are very compact and faint, giving a large scatter of visibility points on the long baselines. Although most of the imaged sources are resolved, they are highly core-dominated in flux (*bottom right panel*). Some of the extremely compact sources have the core dominance index $S_{\text{core}}/S_{\text{CLEAN}}$ larger than unity due to the uncertainty of the model fit and CLEAN flux.

The overall sample of imaged sources consist of 78 quasars, 22 BL Lac objects, and 8 radio galaxies. Despite the significant difference in the number of sources between the optical classes, the dependence of sub-milliarcsecond scale compactness S_L/S_S on the optical class is apparent in the distribution. Quasars and BL Lacs have similar distributions (the average is 0.54 for quasars and 0.48 for BL Lacs, and the median is 0.48 for quasars and 0.42 for BL Lacs), and radio galaxies have a relatively different distribution (the average is 0.38 and the median is 0.41). The dependence is also evident in Figure 8, which shows the normalized mean visibility function in terms of uv -radius, averaged for Quasars, BL Lacs, and radio galaxies. The normalized mean visibility amplitudes for radio galaxies are, on average, lower than those for quasars and BL Lacs. At long uv -radii ranging from $700 M\lambda$ to $2500 M\lambda$, the amplitudes for the radio galaxies are quite distinct from those of the quasars and BL Lac objects in the sample. Overall, the radio galaxies are less compact than the others, but BL Lacs and quasars are similar in compactness. According to the unification paradigm of AGN (Urry & Padovani 1995), it is expected that quasars and BL Lacs on sub-milliarcsecond scales are still more compact than radio galaxies since the former are seen at smaller viewing angle and brightened by Doppler boosting. Our results from the 86 GHz VLBI survey are consistent with this.

6.2. Brightness temperature T_b

Figure 9 shows the distributions of flux density and angular size for the core components. Most of the cores are smaller than 0.1 mas in angular size. The cores of 77 sources are resolved and 32 sources have unresolved core components. Most of the unresolved sources are quasars (23), and a few sources are BL Lacs (7) and radio galaxies (2).

Figure 10 shows the distributions of the measured core brightness temperatures in the source frame. The median value of these brightness temperatures is 7×10^{10} K. The tail of the distribution extends up to 5×10^{12} K. Only about 1 % of the imaged sources yield brightness temperatures greater than 1.0×10^{12} K, which is the maximum value of the inverse Compton limit (Kellermann & Pauliny-Toth 1969), and about 8 % have brightness temperatures higher than 3.0×10^{11} K, which corresponds to the equipartition limit (Readhead 1994). This distribution shows brightness temperatures lower by a factor of 10 than those derived from the VSOP survey at 5 GHz (see Horiuchi et al. 2004) and VLBA 2 cm Survey (see Kovalev et al. 2005). Higher brightness temperatures of compact radio sources can be explained by Doppler boosting, transient non-equilibrium events, coherent

emission, emission by relativistic protons, or a combination of these effects (see Kardashev 2000; Kellermann et al. 2003). Such a substantial decrease in the brightness temperatures measured at 86 GHz may be caused by two reasons. Most of the extragalactic radio sources may be resolved at 86 GHz, as indicated by the compactness index derived in this paper. Alternatively, opacity and other physical conditions can change along the jet, causing observations at 86 GHz to probe regions of the flow in which the brightness temperature is intrinsically lower (due to gradients in the physical conditions in the flows, see e.g., Marscher 1995). Both these possibilities will be investigated in a follow-up paper.

6.3. Intraday variable sources

In order to identify intraday variable (IDV) sources in our sample, we used the list of IDV sources compiled in Kovalev et al. (2005, see references therein). Clear identifications can be made for most of the objects except 6 sources: 1044+719, 1150+497, 1842+681, 1923+210, 2013+370, and 2023+336. From the references given in Kovalev et al. (2005), we identify them as “non-IDV” sources. In total, 26 sources are identified as “IDV” sources in our sample.

Figure 11 shows the distributions of the correlated flux density at the longest baseline S_L (*top left panel*), and the core flux density S_{core} (*top right panel*), as well as the distributions of the size d_{core} (*middle right panel*) and brightness temperature T_b (*bottom right panel*) of the cores. The source compactness on sub-milliarcsecond scales S_L/S_S (*middle left panel*) and the core dominance $S_{\text{core}}/S_{\text{CLEAN}}$ (*bottom left panel*) are also compared for the IDV and non-IDV sources. The statistics of the distributions are summarized in Table 8.

The IDV and non-IDV sources have different mean values (0.36 Jy and 0.31 Jy) median values (0.26 Jy and 0.21 Jy) of the correlated flux densities at the longest baselines, S_L . The Kolmogorov-Smirnov (K-S) test shows that there is a 17% chance that the IDV and non-IDV samples are derived from a common distribution. This is a somewhat inconclusive result due to a few points at higher flux densities in the non-IDV sample, which affects strongly the statistical results. If we exclude those outliers, then the mean of the non-IDV sample gets smaller than that of the IDV sample and the probability decreases to 15%. However, it is difficult to conclude that IDV sources have a higher flux density S_L than non-IDV sources in our sample.

The distributions of the compactness index S_L/S_S for IDV and non-IDV sources have means of 0.53 and 0.51 with medians of 0.46 and 0.44. The K-S test shows that a common parent distribution for IDV and non-IDV sources is acceptable at a 100% level. In Figure 12, it is shown that the sub-milliarcsecond compactness S_L/S_S for the IDV sources is, on average, similar to the non-IDV sources.

For the core dominance $S_{\text{core}}/S_{\text{CLEAN}}$, the K-S test implies a single parent population for IDV and non-IDV sources with the K-S probability at a 80% level. We conclude therefore that IDV sources are similar to non-IDV sources in core-dominance.

We find different results for the core parameters such as the core flux density, the core size, and the core brightness temperature of IDV and non-IDV sources. The distributions of the core flux density S_{core} for IDV and non-IDV sources have means of 0.70 Jy and 0.62 Jy, with medians of 0.42 Jy and 0.46 Jy. They have a 34% probability of being derived from a common population. This is quite distinctive from the results for the other parameters. The distributions of the core sizes d_{core} for IDV and non-IDV sources have means of 0.039 mas and 0.057 mas with medians of 0.035 mas and 0.043 mas. The cores of IDV sources are smaller in angular size than those of non-IDV sources. The K-S test also yields a probability of less than 4% that the core size has the same parent distribution for IDV and non-IDV sources. The mean values of the core brightness temperature for IDV and non-IDV sources are $10^{11.1 \pm 0.1}$ K and $10^{10.8 \pm 0.1}$ K, and the respective median values are $10^{11.1}$ K and $10^{10.8}$ K, respectively. A common parent population of the core brightness temperature for IDV and non-IDV sources is rejected at the 92% level. This implies that, although IDV sources have similar core flux densities to those of non-IDV sources, their brightness temperatures are higher than those of the non-IDV sources due to the smaller angular core size.

7. Summary

We have conducted the largest global 86 GHz VLBI survey of compact radio sources during three GMVA sessions in 2001 October, 2002 April, and 2002 October. Participation of sensitive European telescopes augmented by the VLBA antennas ensured high baseline and image sensitivities. The total of 121 out of 127 sources observed have been detected at least on one baseline and 109 sources have been imaged with a typical dynamic range exceeding 50. The survey observations have resulted in an increase by a factor of five of the total number of sources imaged at 86 GHz with VLBI.

We have used two-dimensional, circular Gaussian components to fit the observed visibilities and parameterize the source structure. Using the results of these fits, the source compactness and brightness temperatures have been derived.

We find that almost all of the survey objects are resolved and the cores of about 70% of the imaged sources are resolved. Radio galaxies are less compact than quasars and BL Lacs. BL Lacs are similar to quasars in the compactness at sub-milliarcsecond scales.

The distribution of the core brightness temperatures peaks at $\sim 10^{11}$ K and only 1% of the cores have brightness temperatures higher than 10^{12} K. This shows apparently lower brightness temperatures than those derived from other VLBI surveys at lower frequencies (e.g., 5 GHz and 15 GHz).

IDV sources in our sample are similar to non-IDV sources in compactness at sub-milliarcseconds. The cores of IDV sources are smaller in angular size and so yield a higher brightness temperature than non-IDV sources, since the core flux densities of both samples are similar to each other.

We thank David Graham for his constant support for the mm-VLBI observation and correlation. We gratefully thank the staff of the observatories participating in the GMVA; the MPIfR Effelsberg 100-m telescope, the IRAM Plateau de Bure Interferometer, the IRAM 30-m telescope, the Metsähovi Radio Observatory, the Onsala Space Observatory, and the VLBA. IRAM is supported by INSU/CNRS (France), MPG (Germany) and IGN (Spain). The VLBA is an instrument of the National Radio Astronomy Observatory, which is a facility of the National Science Foundation operated under cooperative agreement by Associated Universities, Inc. This research has made use of the NASA/IPAC Extragalactic Database, which is operated by the Jet Propulsion Laboratory, California Institute of Technology, under contract with the National Aeronautics and Space Administration. S.-S.L. would like to acknowledge support from Korea Science and Engineering Foundation under grant M06-2004-000-10009.

REFERENCES

- Agudo, I., et al. 2007, Exploring the Cosmic Frontier, ESO Astrophysics Symposia European Southern Observatory, Volume . ISBN 978-3-540-39755-7. Springer, 2007, p. 179, 179
- Alef, W., & Graham, D. A. 2002, Proceedings of the 6th EVN Symposium, 31
- Alef, W., & Müskens, A. 2001, Proceedings of the 15th Workshop Meeting on European VLBI for Geodesy and Astrometry. Institut d'Estudis Espacials de Catalunya, Consejo Superior de Investigaciones Científicas, Barcelona, Spain, September 07-08, 2001. Edited by Dirk Behrend and Antonio Rius., p.46, 46
- Attridge, J. M. 2001, ApJ, 553, L31
- Beasley, A.J., Dhawan, V., Doeleman, S., & Phillips, R.B. 1997, Millimeter-VLBI Science Workshop, ed. R. Barvainis & R.B. Phillips, MIT-Haystack Observatory, p. 53
- Bower, G. C., Backer, D. C., Wright, M., Forster, J. R., Aller, H. D., & Aller, M. F. 1997, ApJ, 484, 118
- Doeleman, S. S., & Claussen, M. 1997, Millimeter-VLBI Science Workshop, 37
- Horiuchi, S., et al. 2004, ApJ, 616, 110
- Fomalont, E. B. 1999, Synthesis Imaging in Radio Astronomy II, 180, 301
- Kardashev, N. S. 2000, Astronomy Reports, 44, 719
- Kellermann, K. I., & Pauliny-Toth, I. I. K. 1969, ApJ, 155, L71
- Kellermann, K. I., Vermeulen, R. C., Zensus, J. A., & Cohen, M. H. 1998, AJ, 115, 1295

- Kellermann, K. I., Lister, M. L., Homan, D. C., Ros, E., Zensus, J. A., Cohen, M. H., Russo, M., & Vermeulen, R. C. 2003, High Energy Blazar Astronomy, 299, 117
- Kovalev, Y. Y., et al. 2005, AJ, 130, 2473
- Krichbaum, T. P., Britzen, S., Standke, K. J., Witzel, A., Schalinski, C. J., & Zensus, J. A. 1995, Proceedings of the National Academy of Science, 92, 11377
- Krichbaum, T. P., Witzel, A., & Zensus, J. A. 1999, 2nd millimeter-VLBI science workshop : IRAM, Granada, Spain, 27-29 May 1999 / edited by A. Greve and T.P. Krichbaum. IRAM, St. Martin d'Héres, France, p.5
- Krichbaum, T. P., Graham, D. A., Bremer, M., Alef, W., Witzel, A., Zensus, J. A., & Eckart, A. 2006, Journal of Physics Conference Series, 54, 328
- Lobanov, A. P., et al. 2000, A&A, 364, 391
- Lobanov, A. P. 2005, ArXiv Astrophysics e-prints, arXiv:astro-ph/0503225
- Lobanov, A. P., Krichbaum, T. P., Witzel, A., & Zensus, J. A. 2006, PASJ, 58, 253
- Lonsdale, C. J., Doebleman, S. S., & Phillips, R. B. 1998, AJ, 116, 8
- Marscher, A. P. 1995, Proceedings of the National Academy of Science, 92, 11439
- Moellenbrock, G. A., et al. 1996, AJ, 111, 2174
- Pagels, A., et al. 2004, European VLBI Network on New Developments in VLBI Science and Technology, 7
- Rantakyro, F. T., et al. 1998, A&AS, 131, 451
- Readhead, A. C. S. 1994, ApJ, 426, 51
- Readhead, A. C. S., et al. 1983, Nature, 303, 504
- Rogers, A. E. E., Phillips, R. B., & Lonsdale, C. J. 1995, BAAS, 27, 1300
- Shepherd, M. C., Pearson, T. J., & Taylor, G. B. 1994, BAAS, 26, 987
- Teraesranta, H., et al. 1998, A&AS, 132, 305
- Urry, C. M., & Padovani, P. 1995, PASP, 107, 803
- Véron-Cetty, M.-P., & Véron, P. 2006, A&A, 455, 773

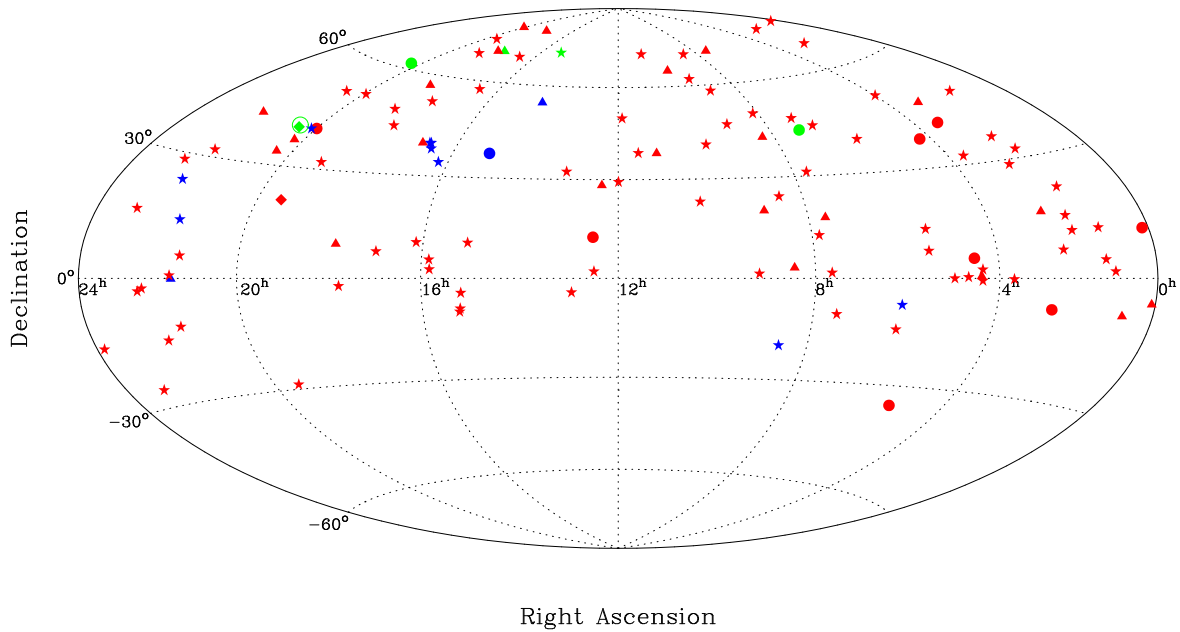


Fig. 1.— The sky-distribution of 86 GHz VLBI sources: 109 detected and imaged sources (red), 12 detected and non-imaged sources (blue) and 6 non-detected sources (green). Symbols: stars are quasars (Q), triangles are BL Lac objects (B), circles are galaxies (G), diamonds are unidentified sources (U) and a single open star represents a star, Cyg X-3 (S).

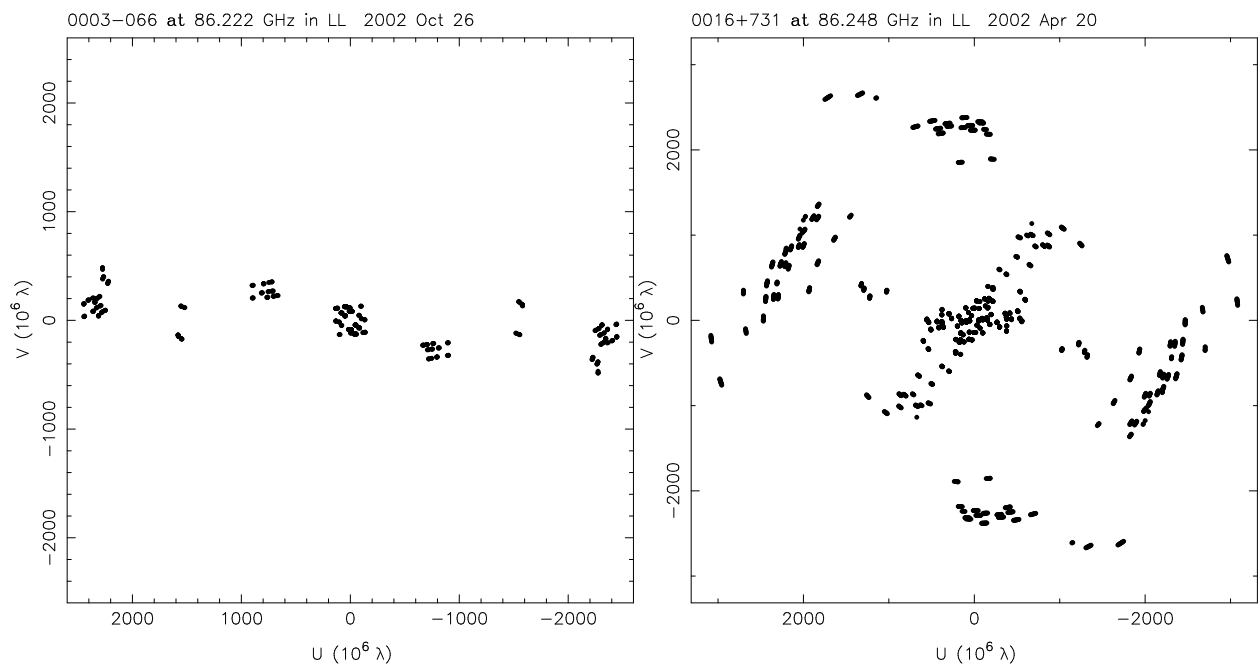


Fig. 2.— *uv*-plots of 0003-066 and 0016+731 at low and high declinations of -06 and 73 degrees, respectively.

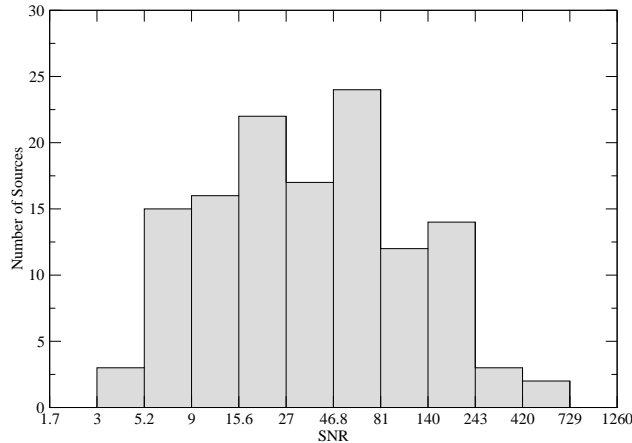


Fig. 3.— Distribution of fringe detection SNR of the sources. The highest SNRs are 425 for 1741-038 on the baseline with Pico Veleta - Plateau de Bure and for 1633+382 with Effelsberg - Pico Veleta. The X-axis is in logarithmic scale of $\sqrt{3}$. The labels on the X-axis are corresponding to $\sqrt{3}^1$, $\sqrt{3}^2$, ... $\sqrt{3}^{13}$.

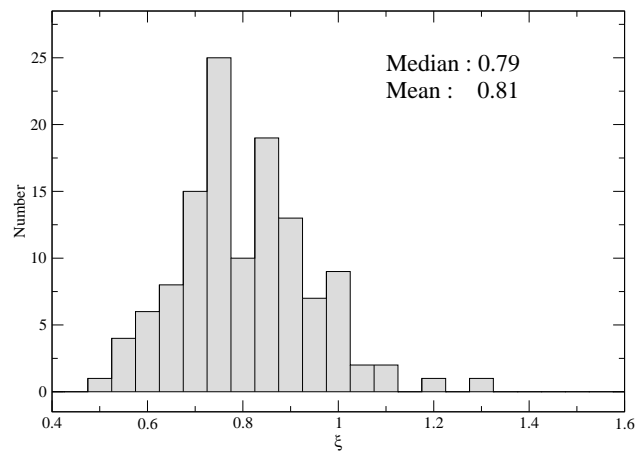


Fig. 4.— Distribution of the image quality factor ξ_r . The median and mean of the distribution are presented.

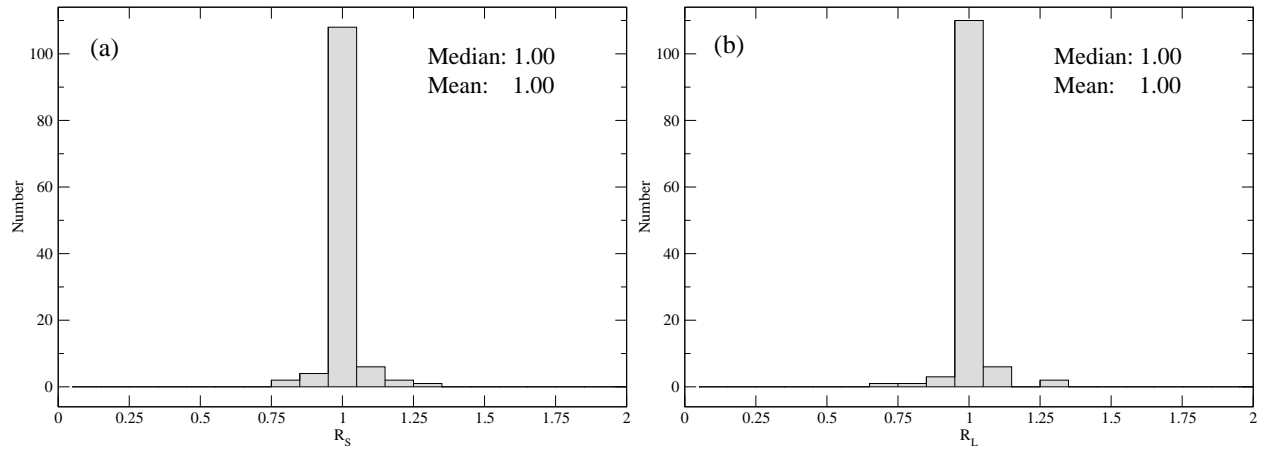


Fig. 5.— Distributions of the correlated flux density ratios (a) $R_S (= S_S / S'_S)$ and (b) $R_L (= S_L / S'_L)$. The means and medians for the distributions are presented in each panel. The correlated flux densities $S_{S,L}$ are listed in Table 6.

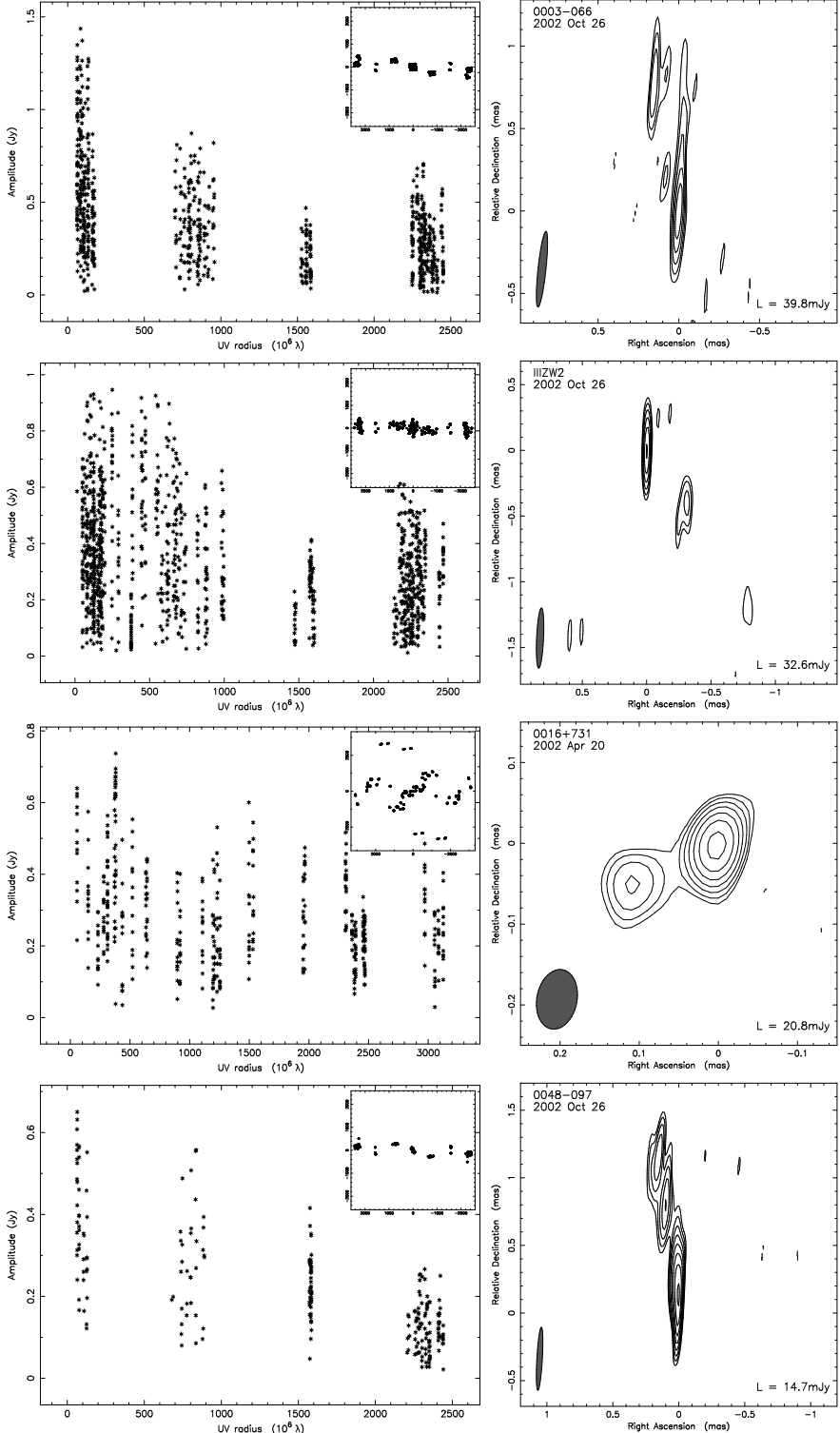


Fig. 6.— 123 contour maps of 109 sources with the distributions of the *uv*-sampling and of the visibility amplitude against *uv*-radius. In the left panel, the X-axis represents the visibility amplitude (correlated flux density) in Jy, averaged over 30 seconds, and the Y-axis shows the *uv*-distance in $10^6 \lambda$. The corresponding *uv*-sampling distribution is given in the inset. In the right panel, a contour map of the CLEANed image is shown. The axes of the maps show the relative offset from the center of image in milliarcsecond. Minimum contour level is shown in the lower-right corner of each map. The contours have a logarithmic spacing and are drawn at $-1, 1, 1.4, \dots, 1.4^n$ of the

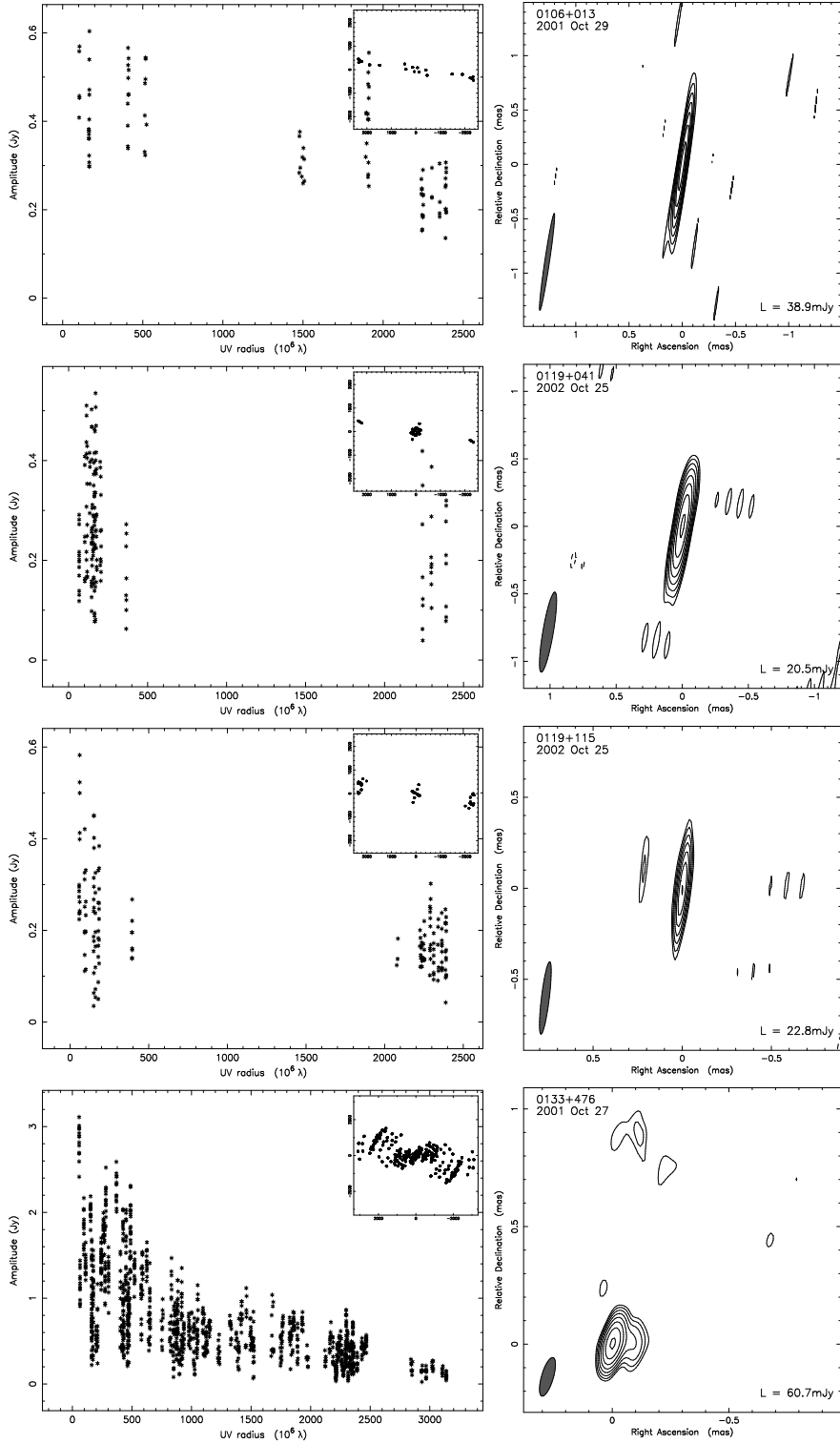


Fig. 6.— *continued.*

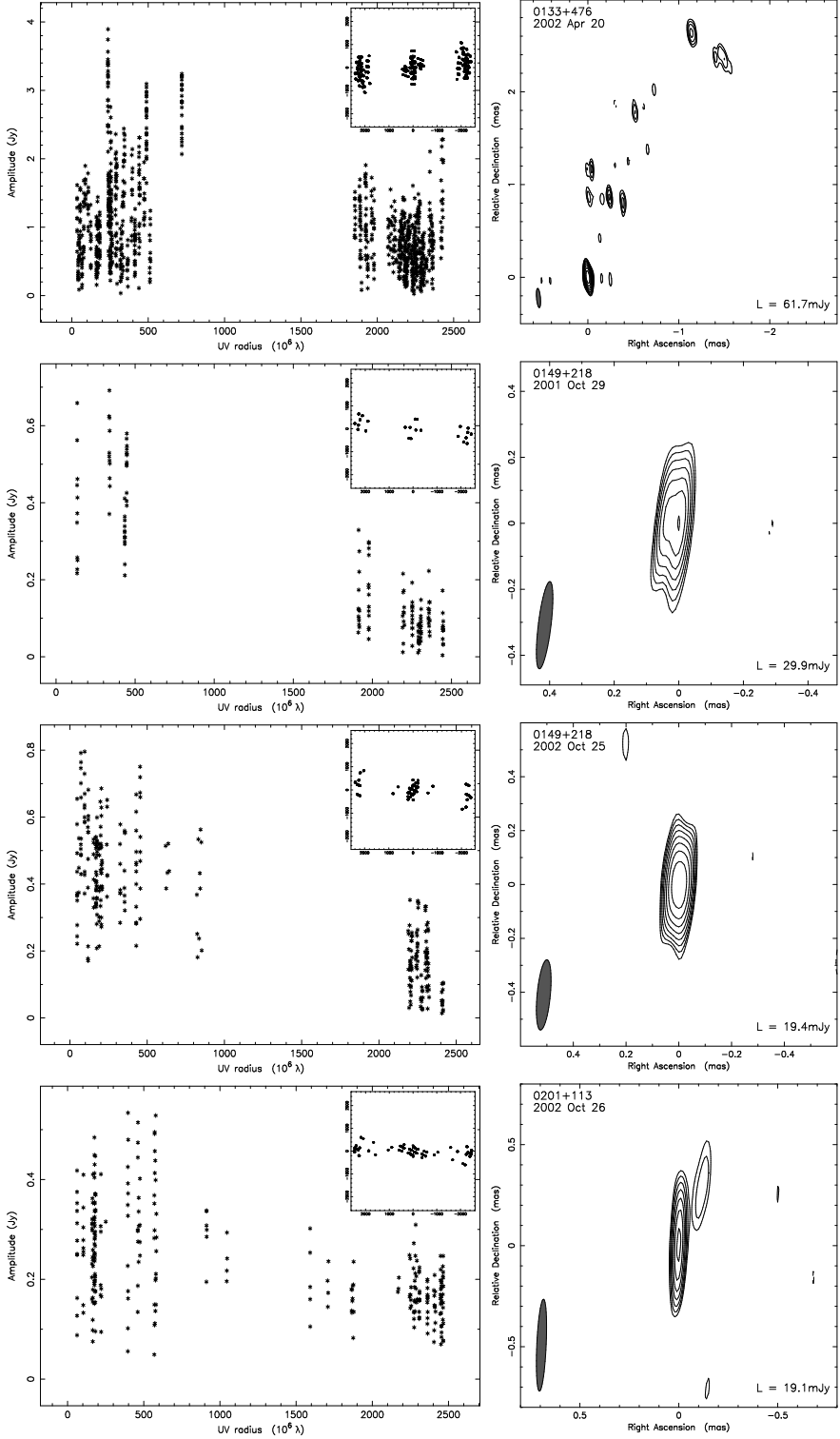


Fig. 6.— *continued.*

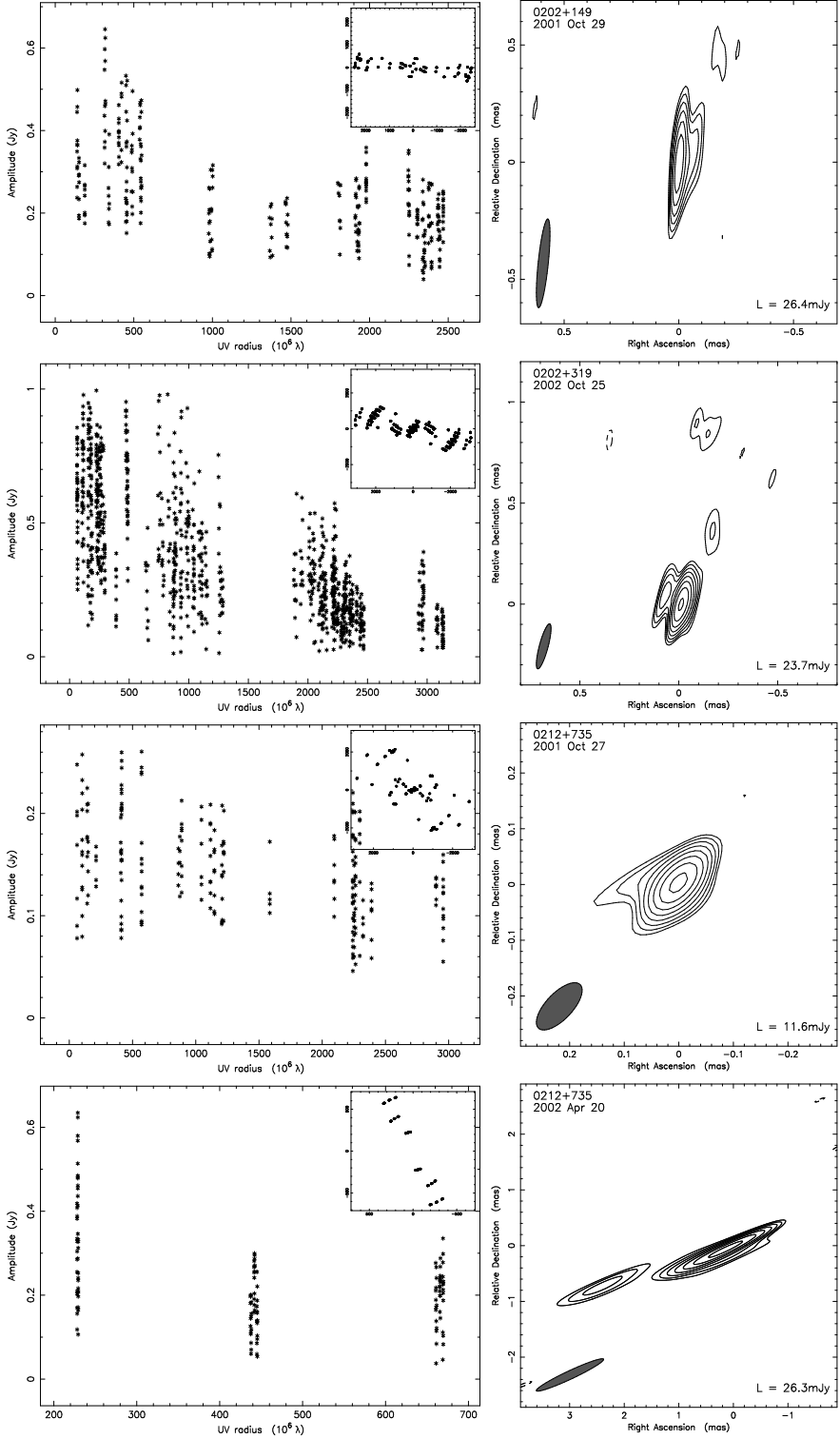


Fig. 6.— *continued.*

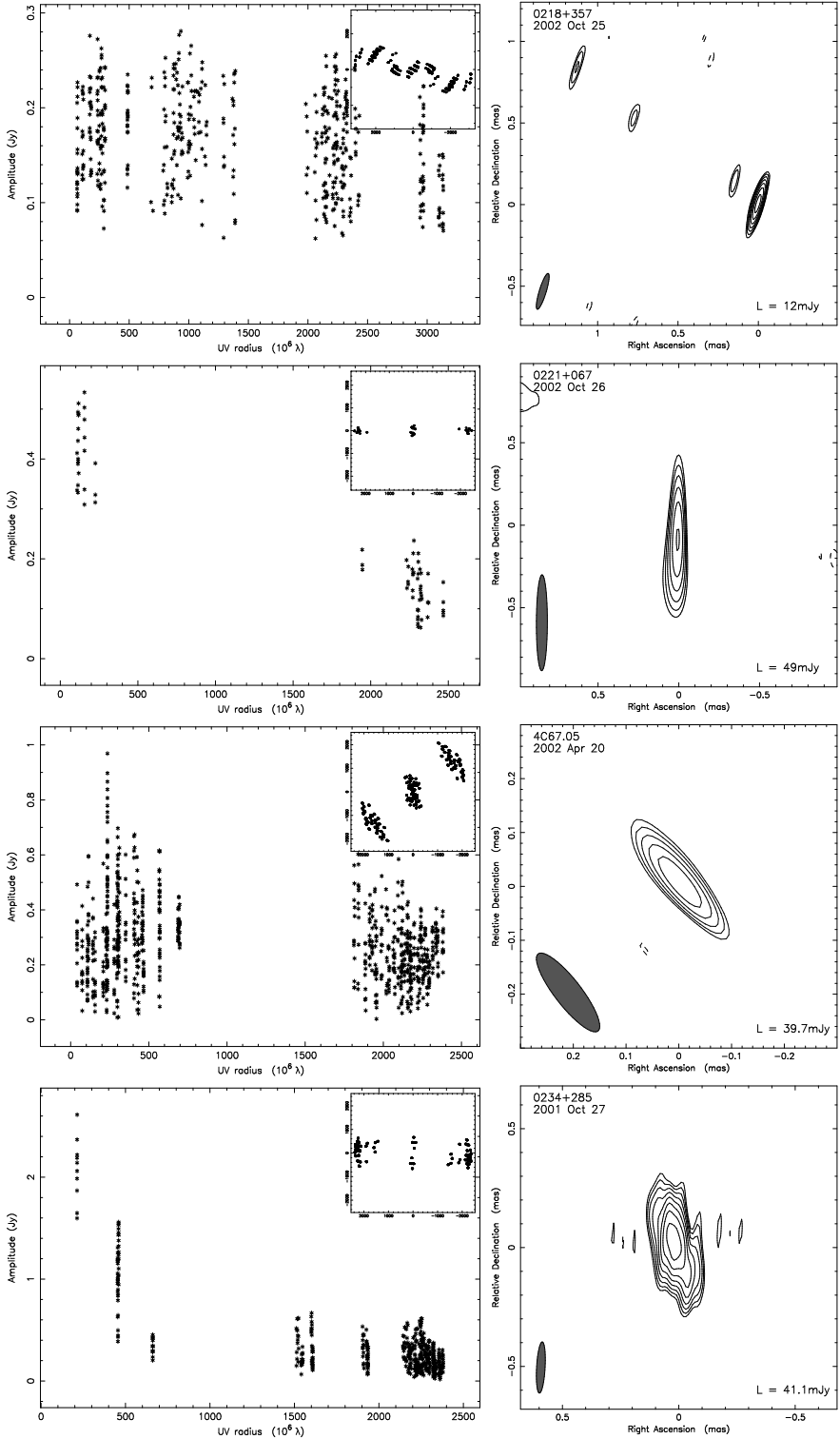


Fig. 6.— *continued.*

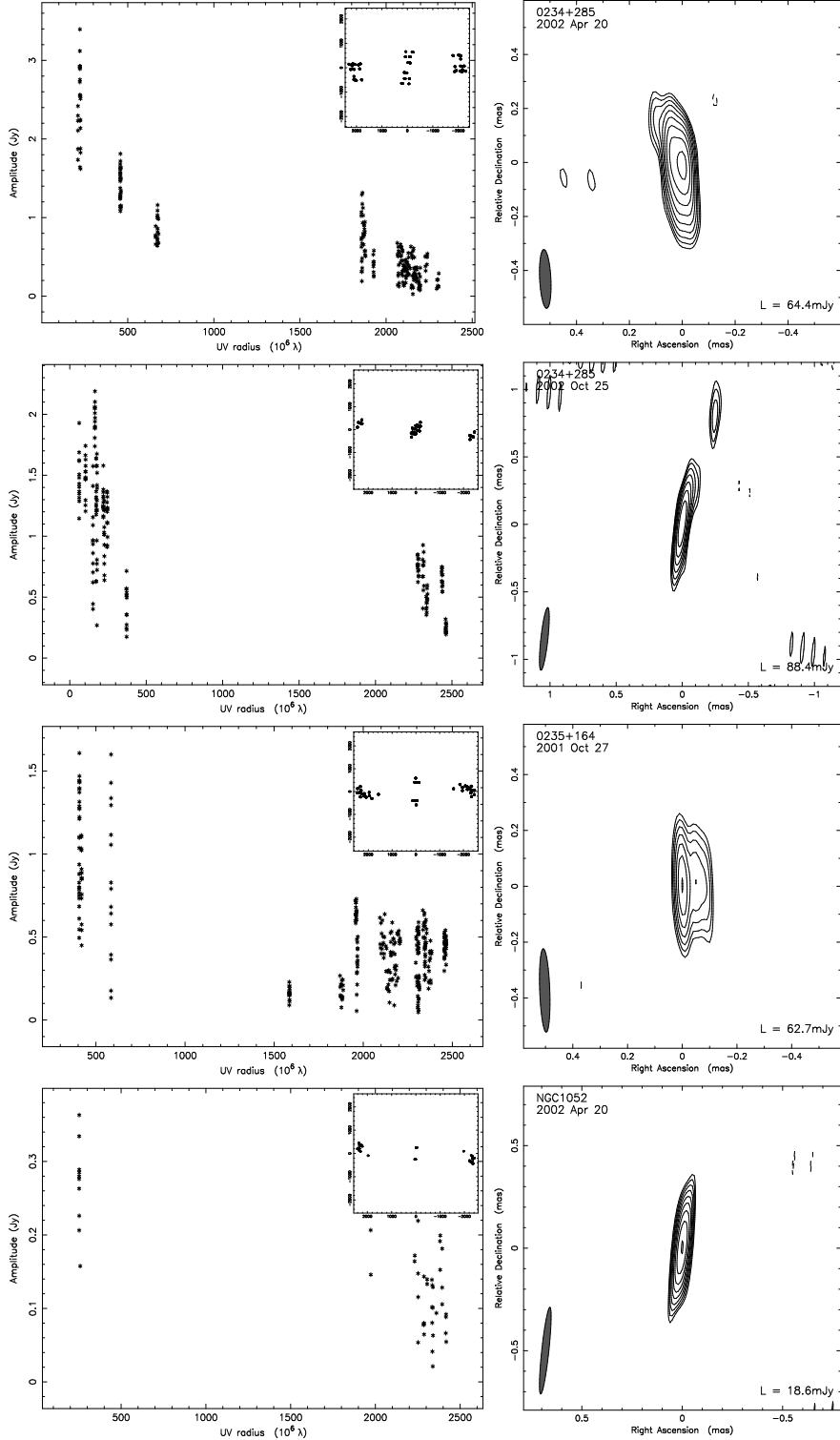


Fig. 6.— *continued.*

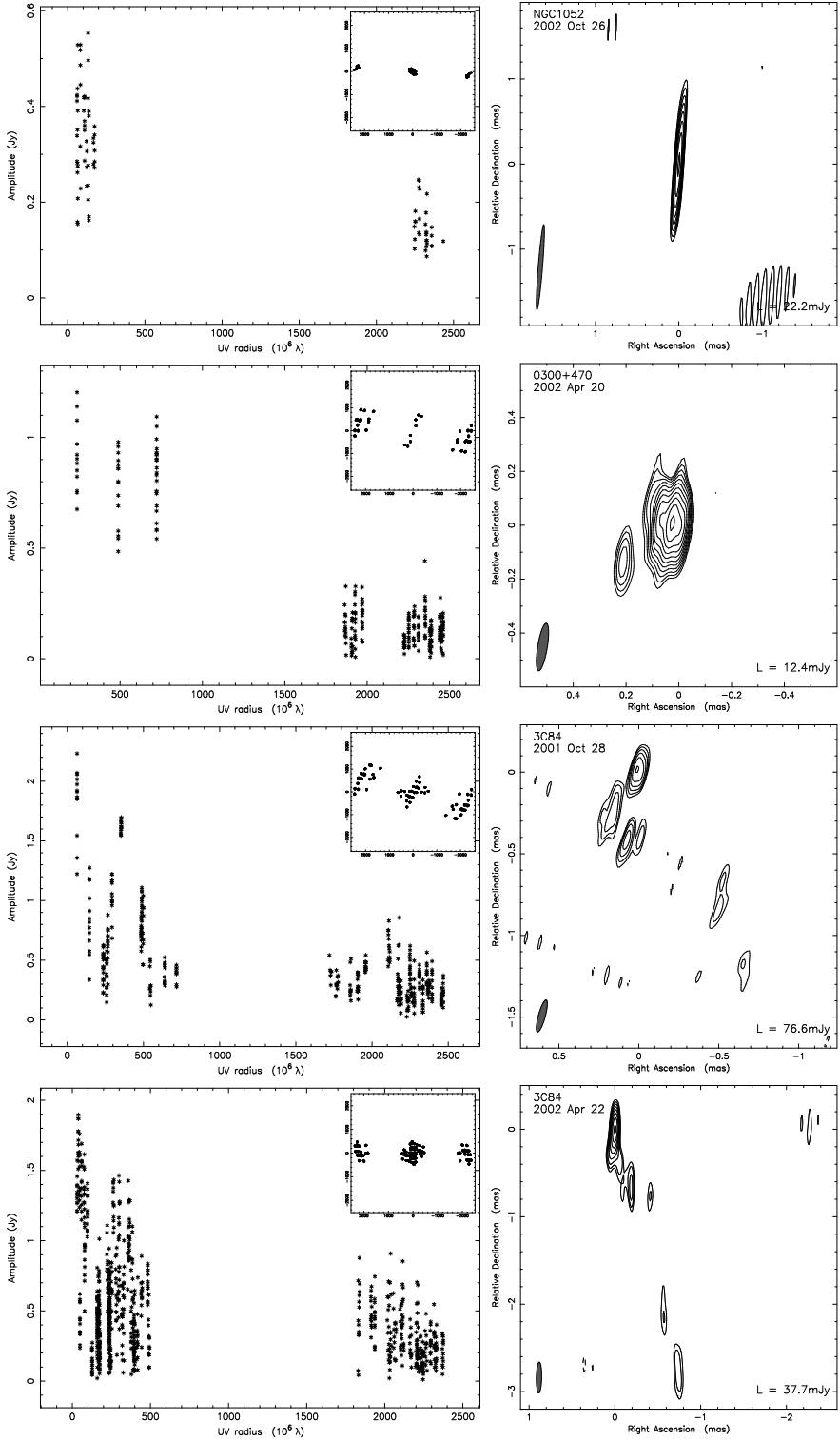


Fig. 6.— *continued.*

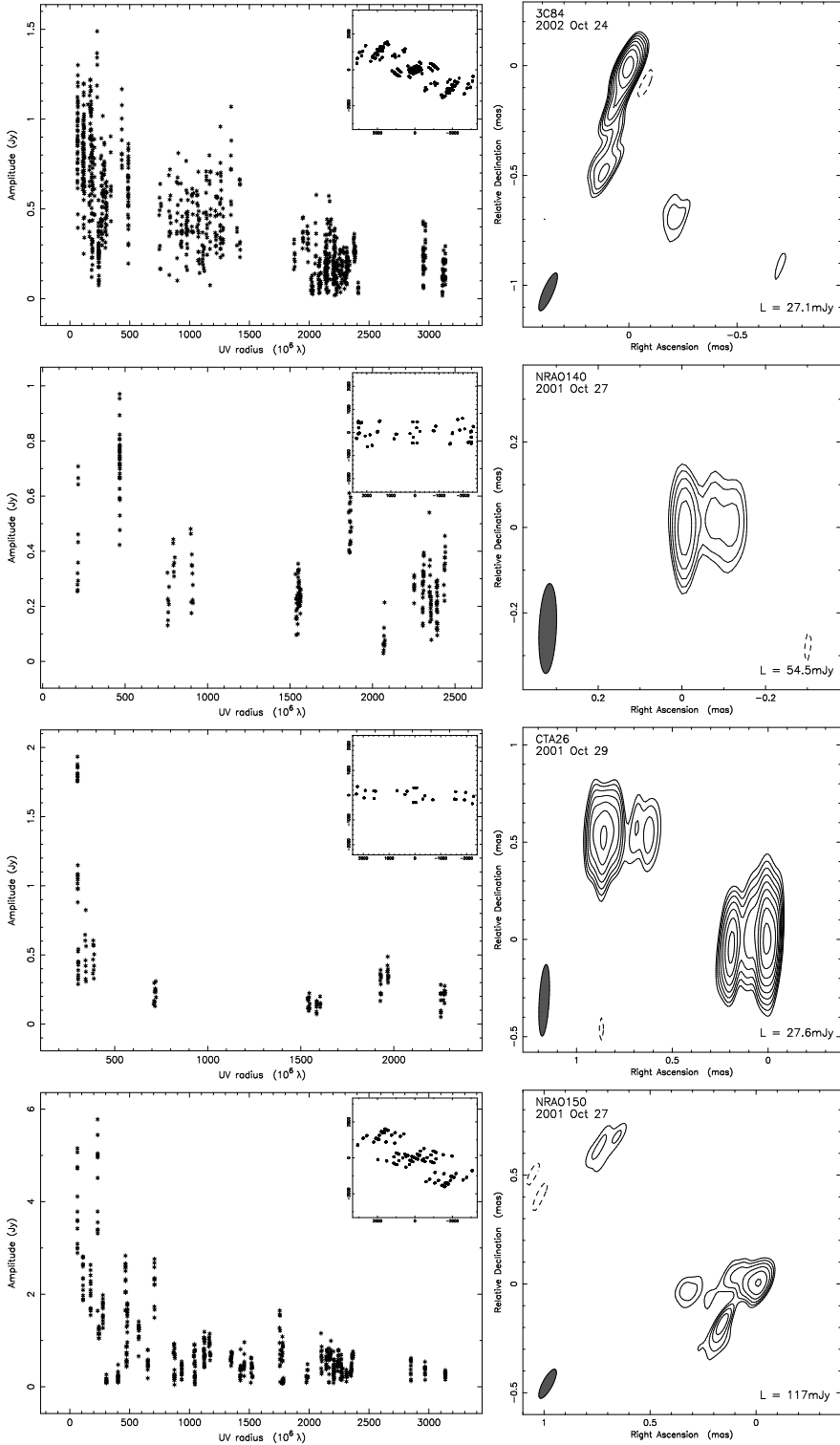


Fig. 6.— *continued.*

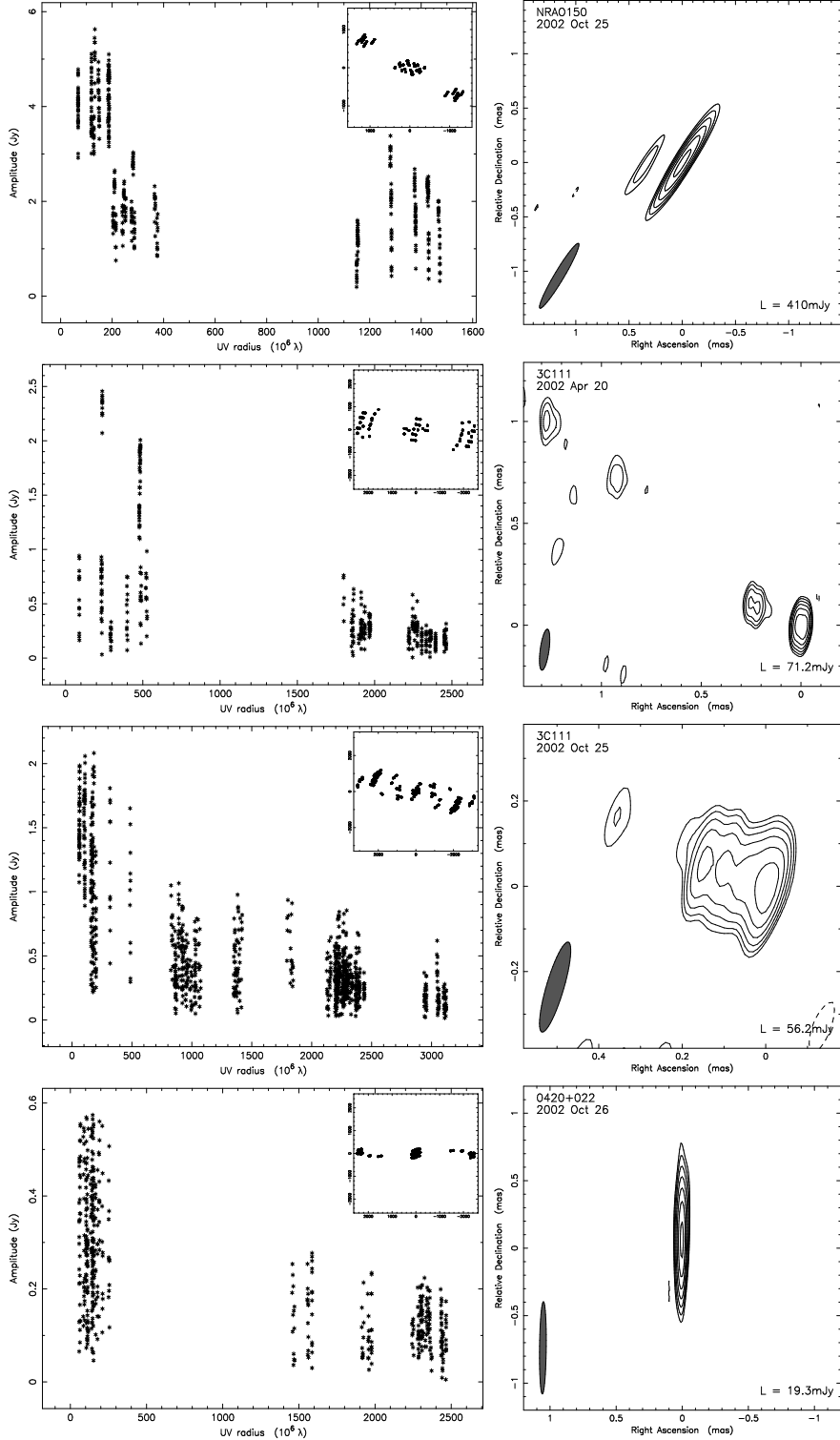


Fig. 6.— *continued.*

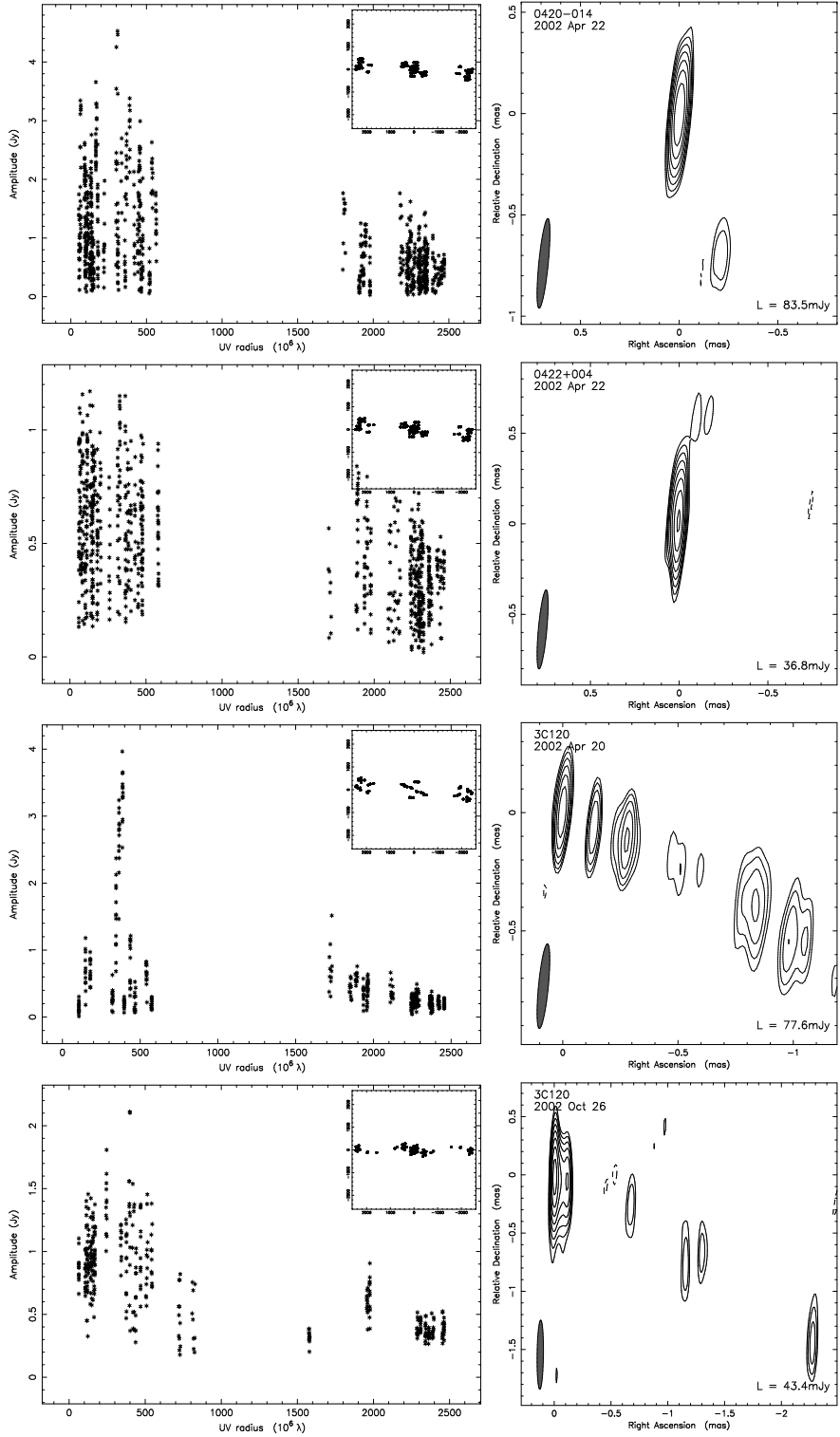


Fig. 6.— *continued.*

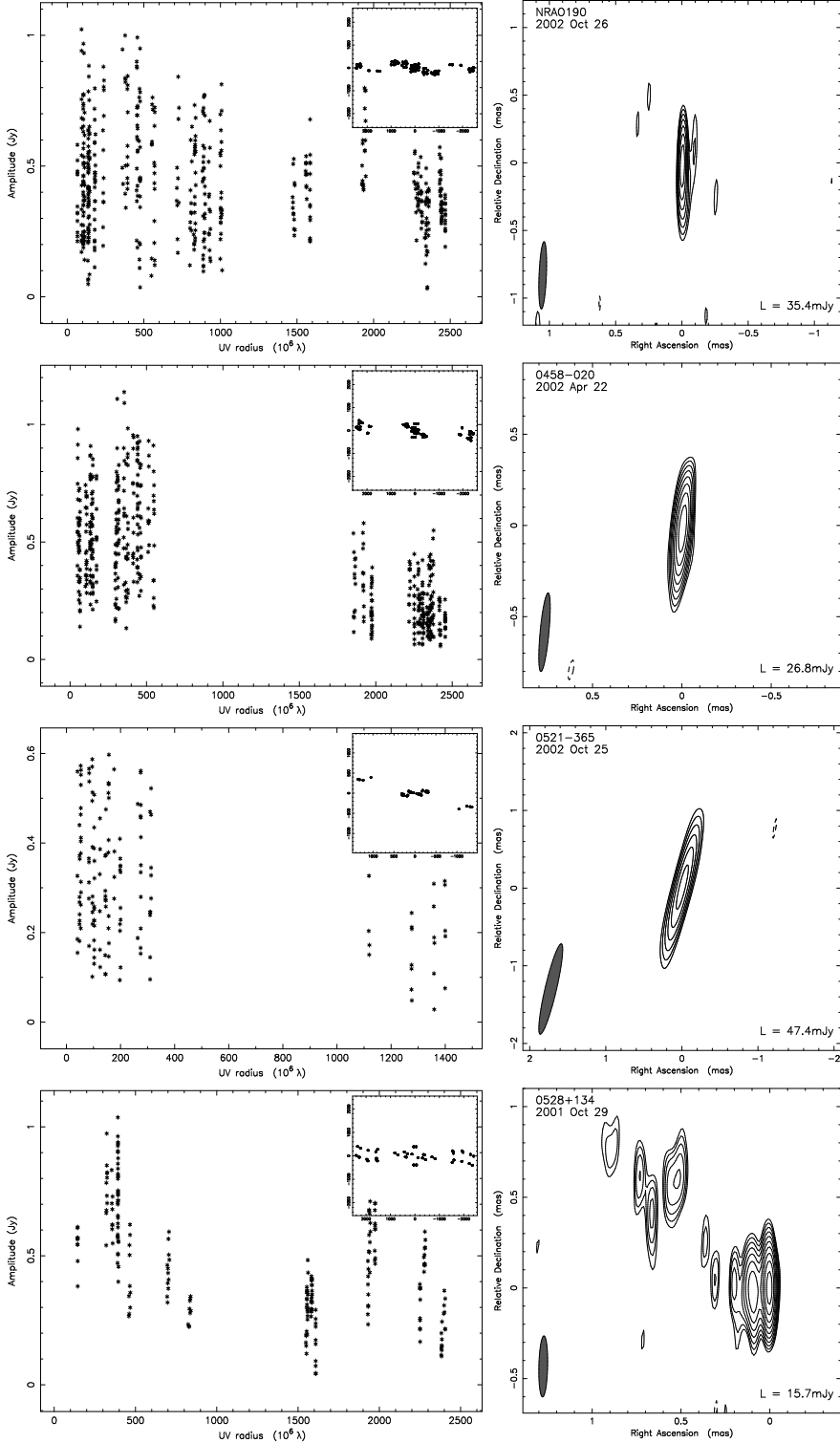


Fig. 6.— *continued.*

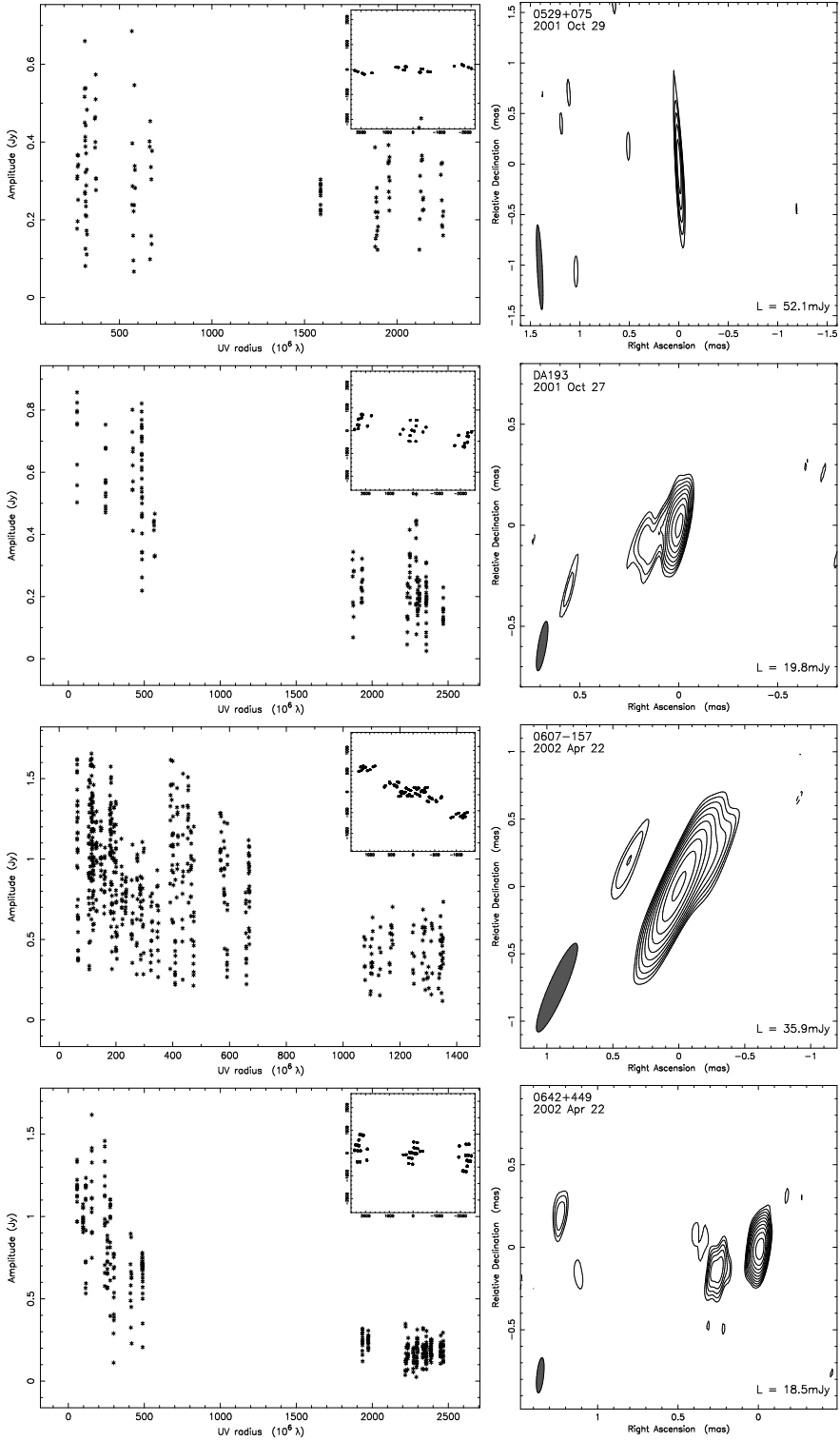


Fig. 6.— *continued.*

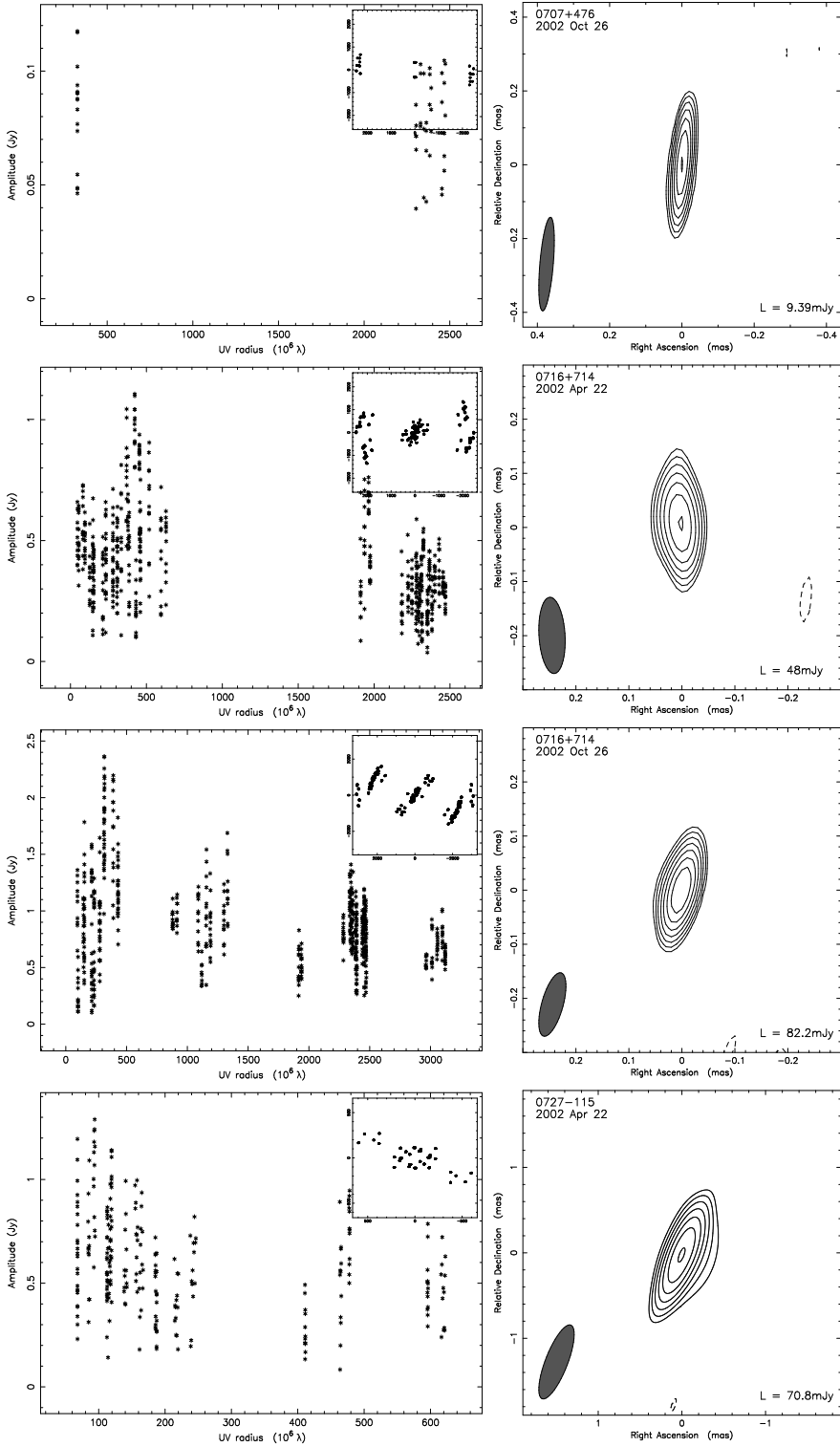


Fig. 6.— *continued.*

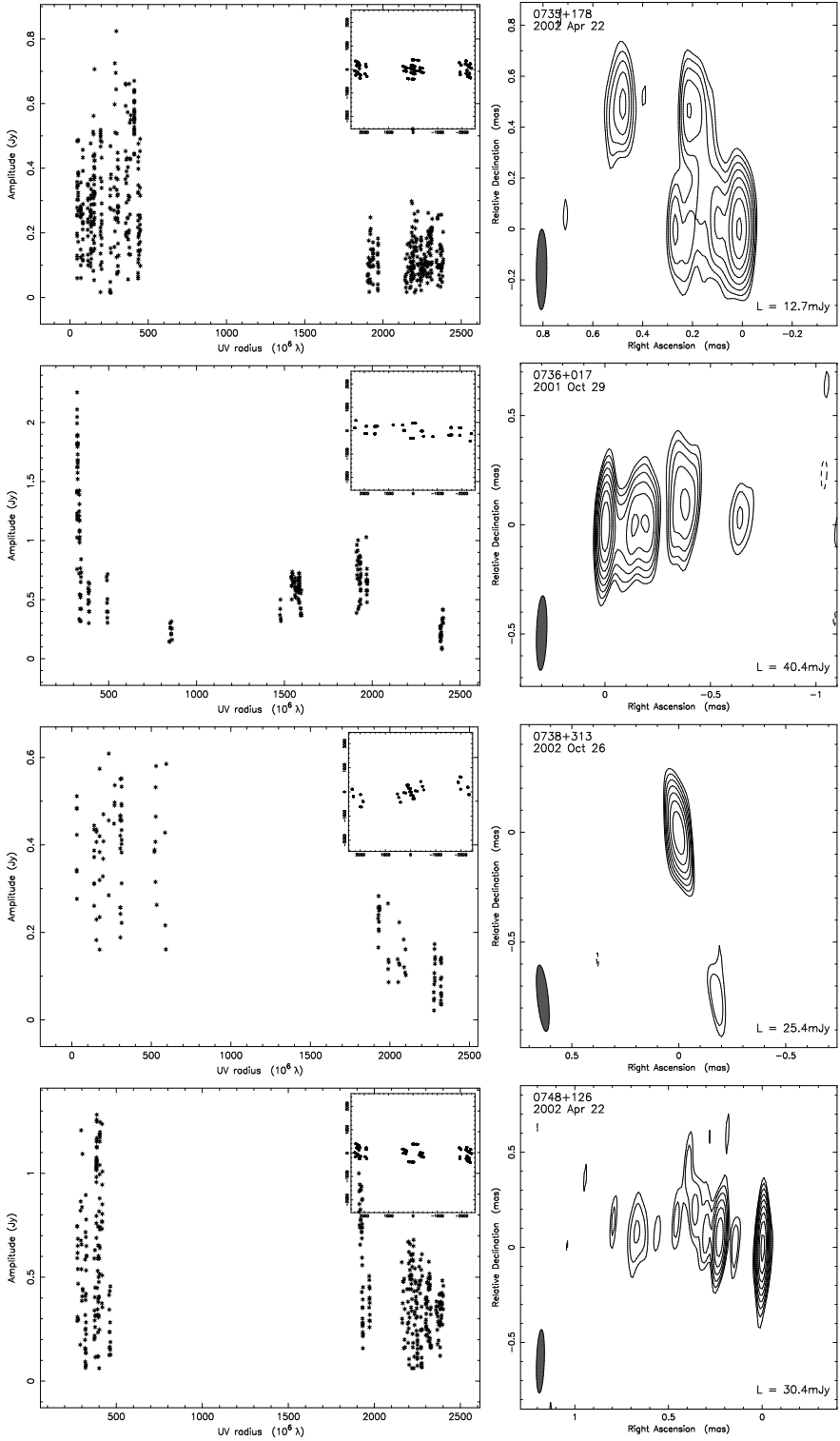


Fig. 6.— *continued.*

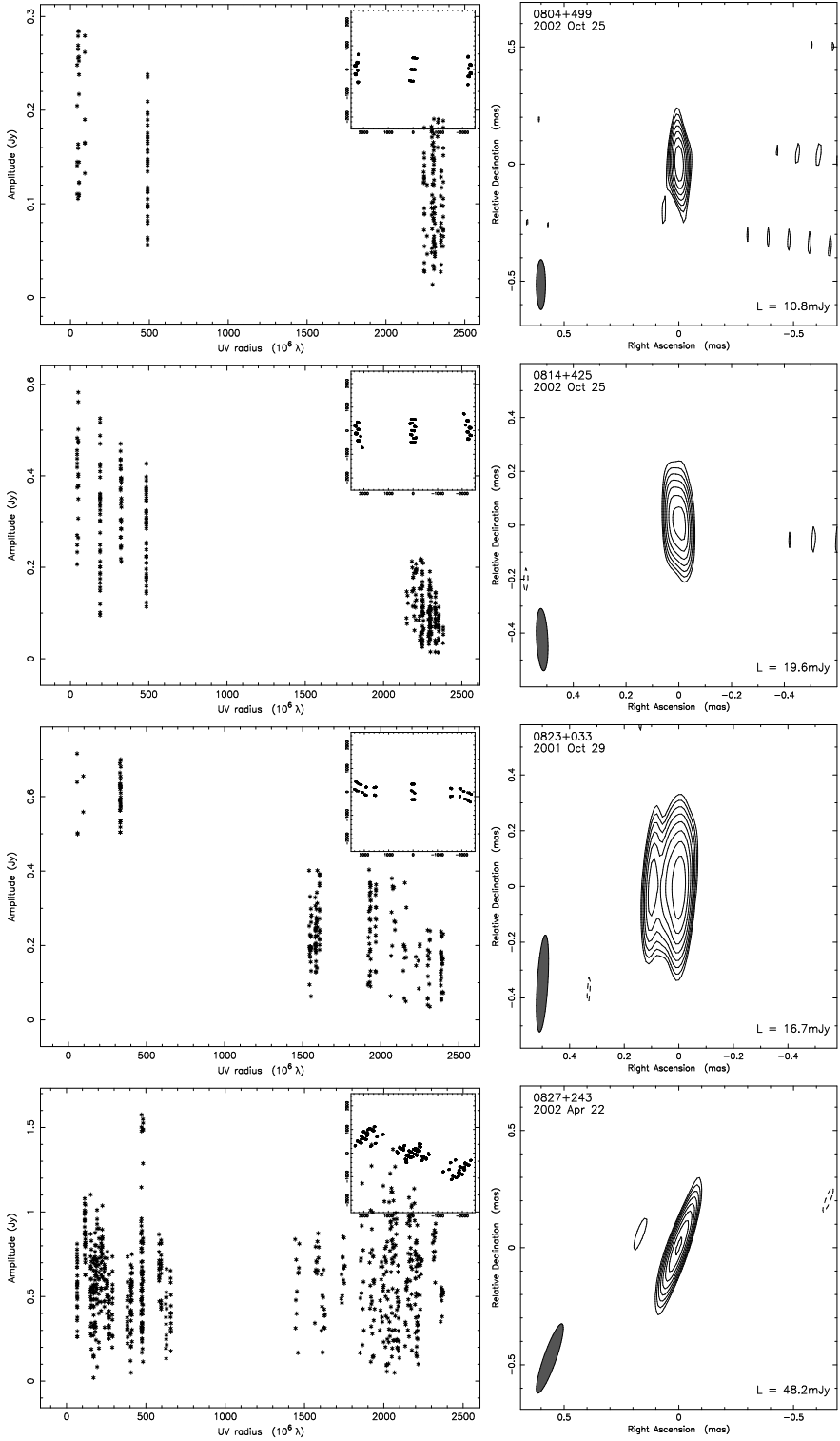


Fig. 6.— *continued.*

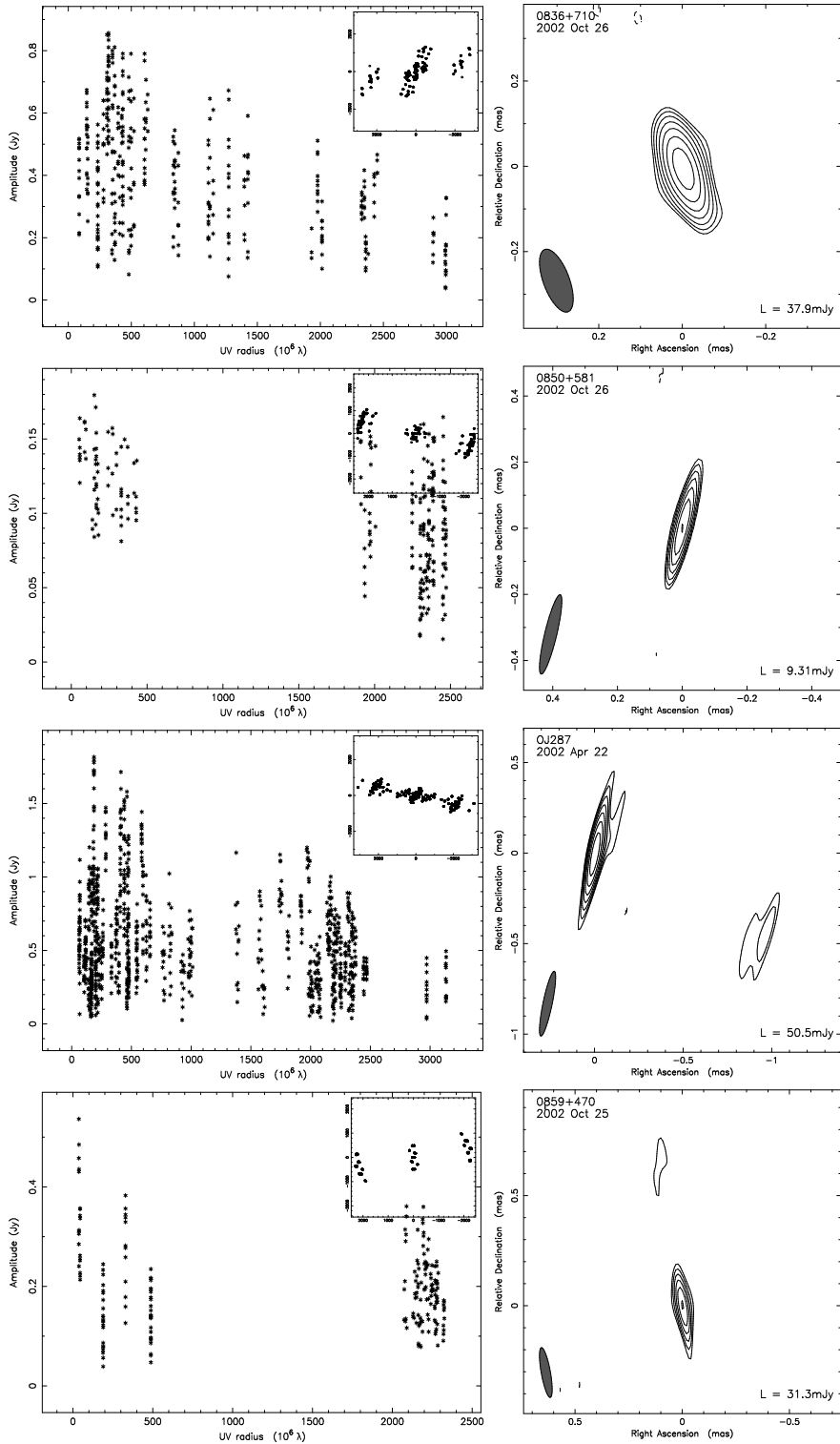


Fig. 6.— *continued.*

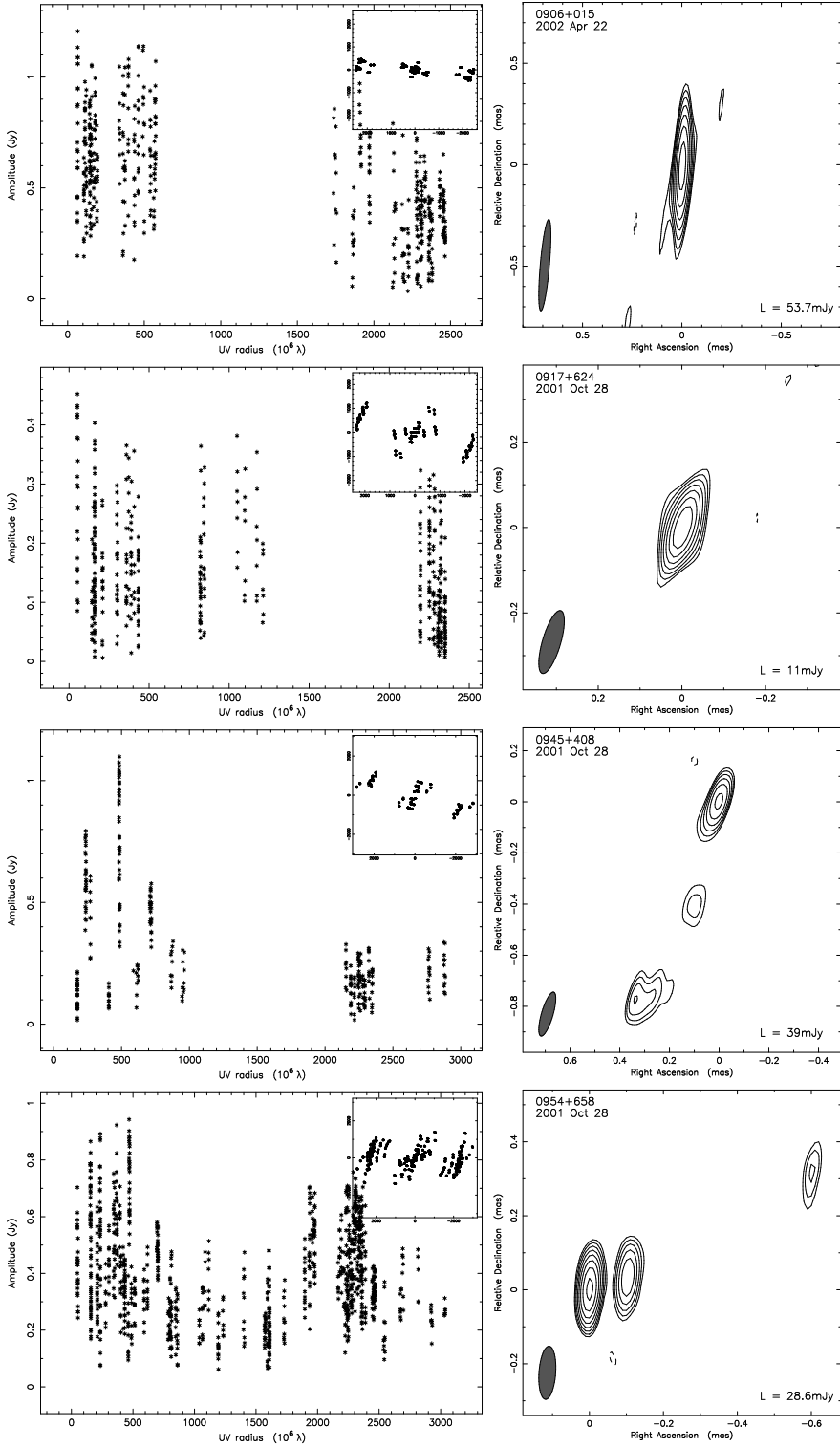


Fig. 6.— *continued.*

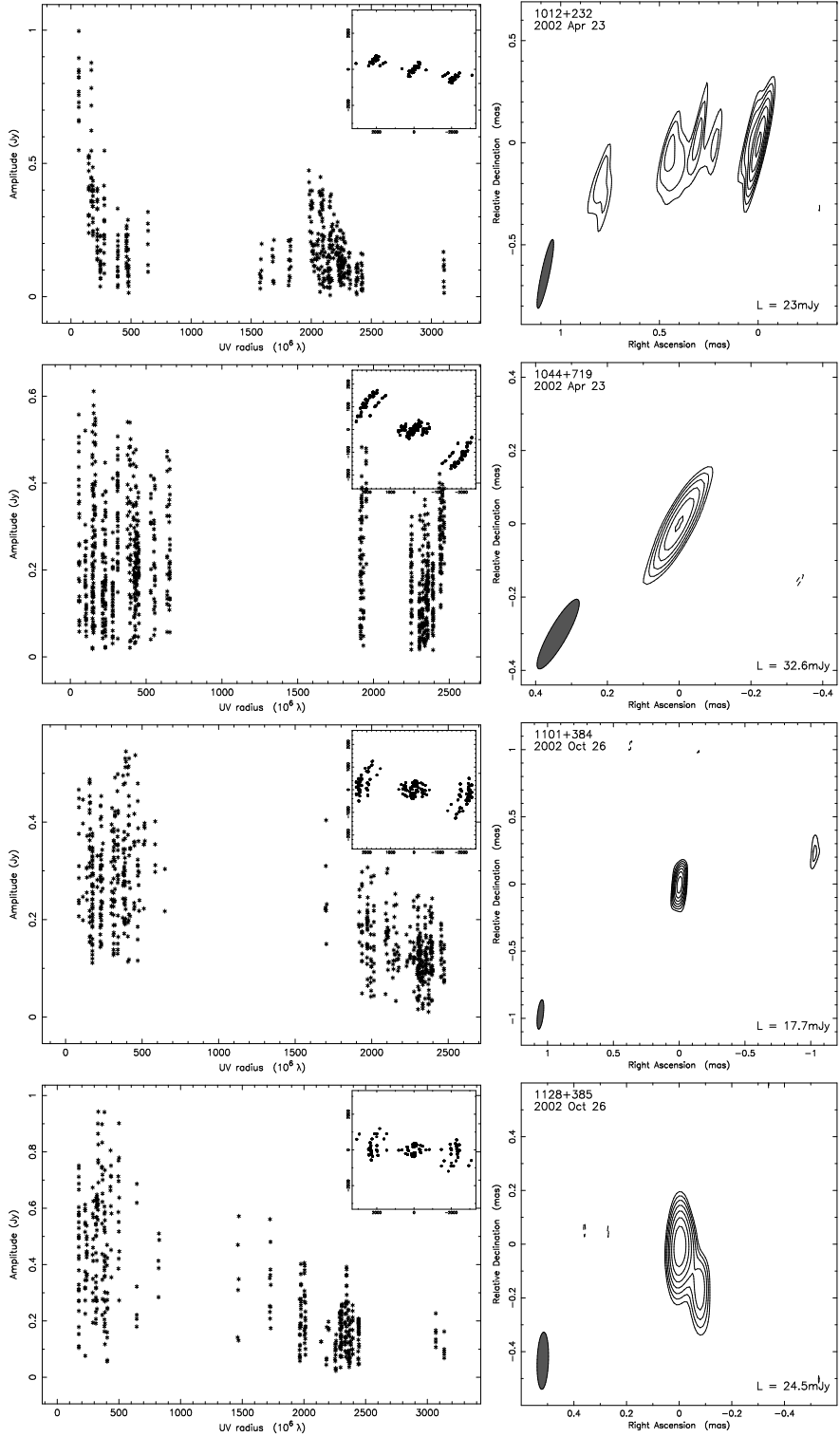


Fig. 6.— *continued.*

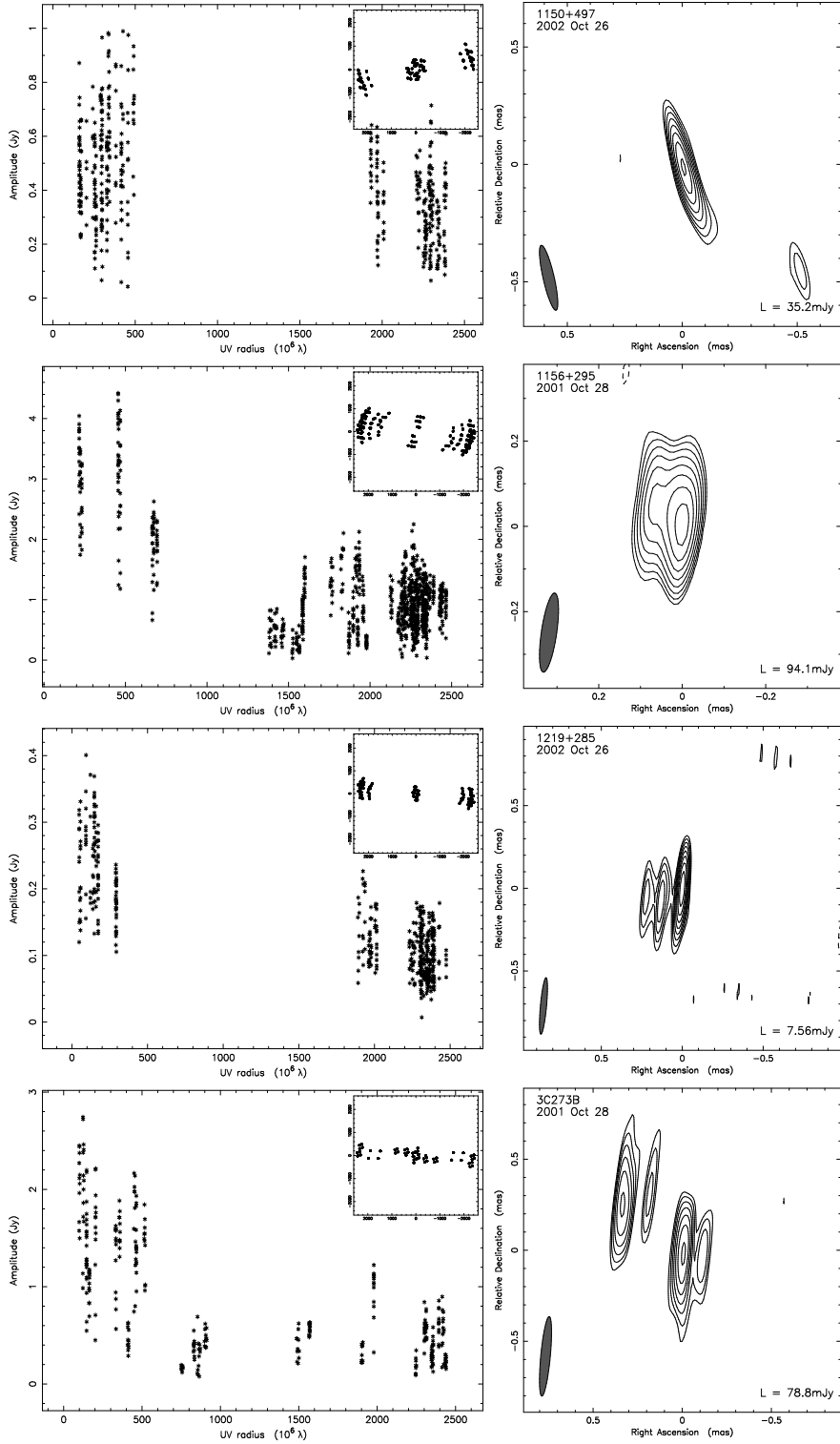


Fig. 6.— *continued.*

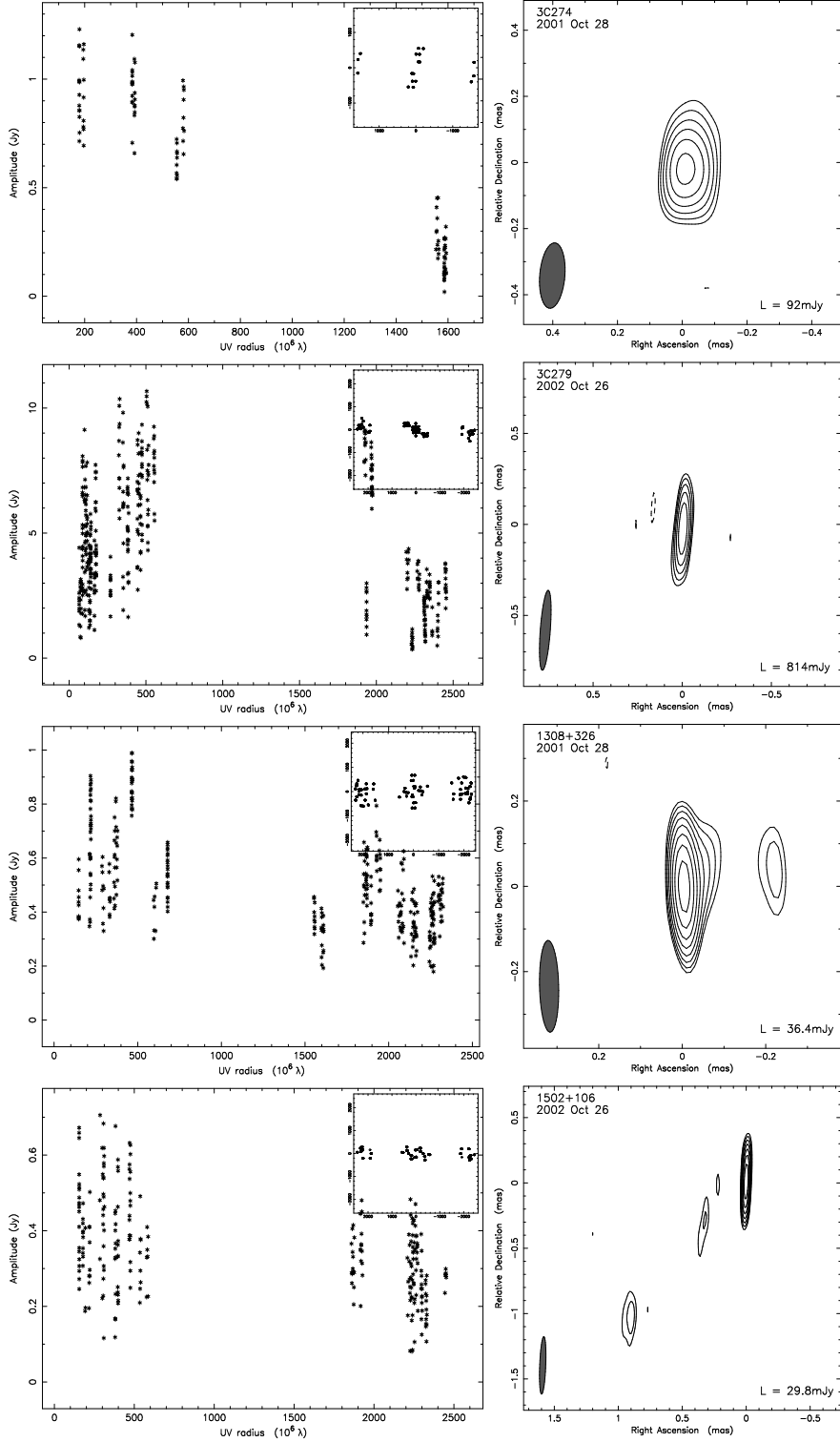


Fig. 6.— *continued.*

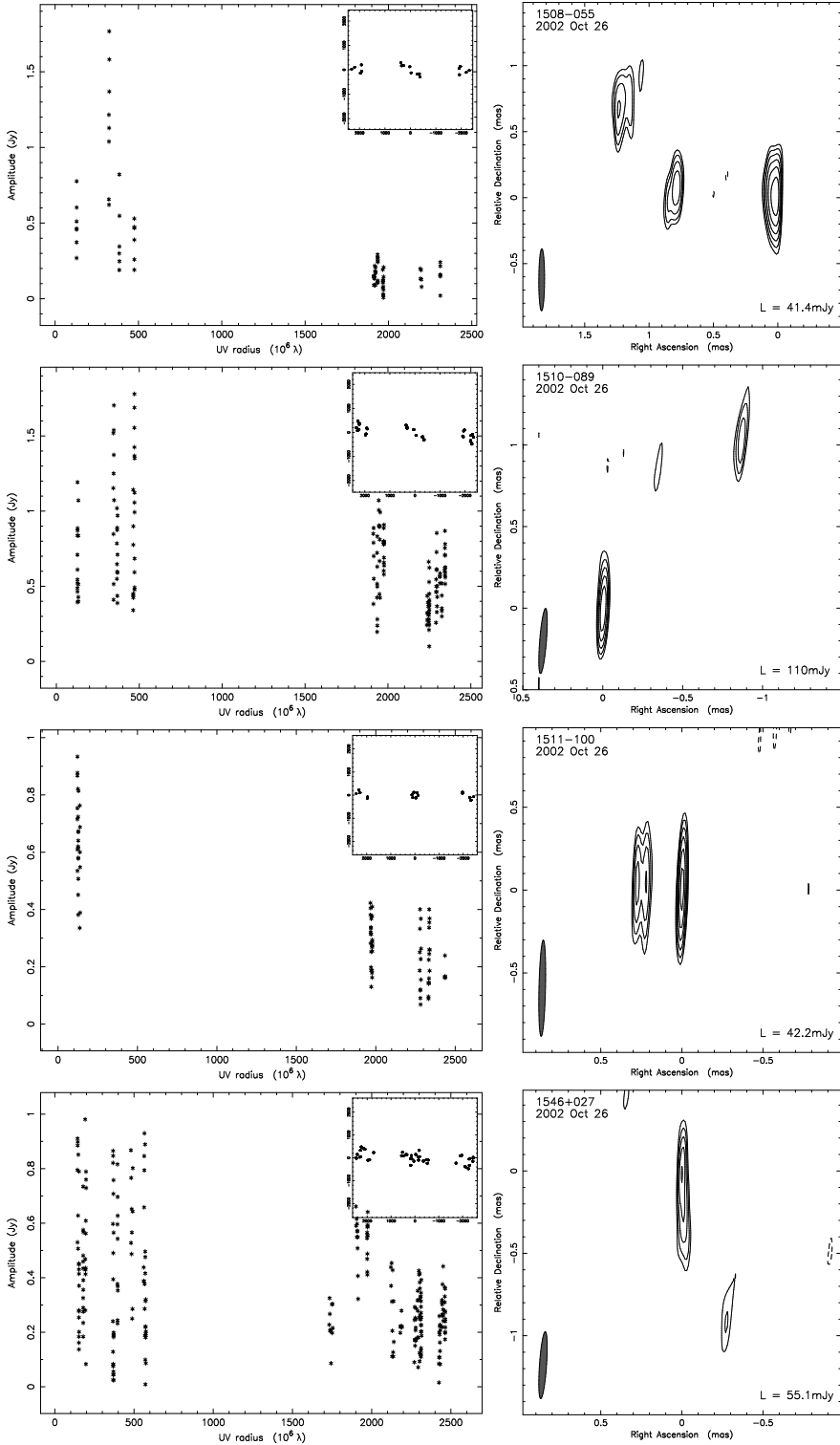


Fig. 6.— *continued.*

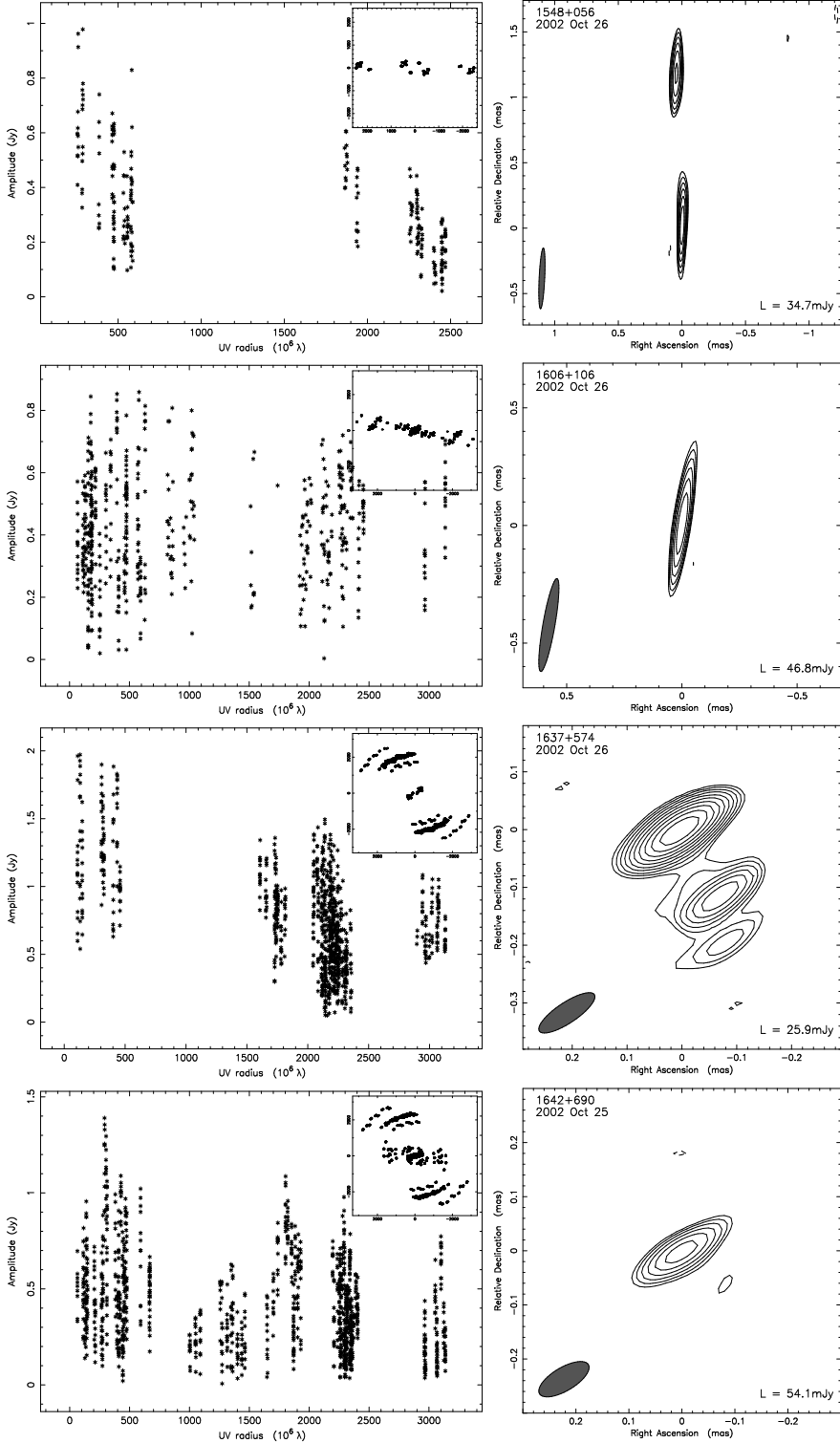


Fig. 6.— *continued.*

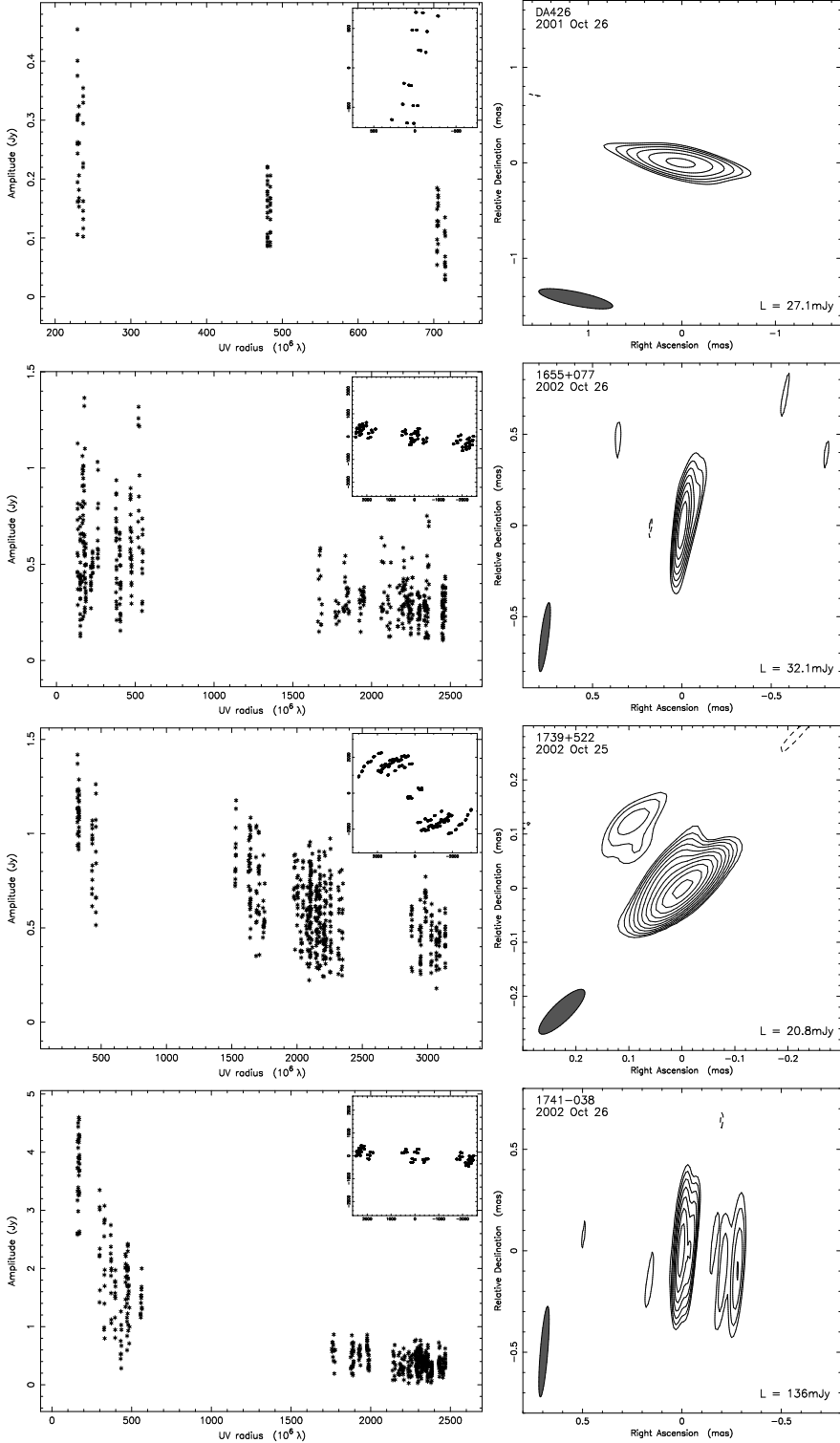


Fig. 6.— *continued.*

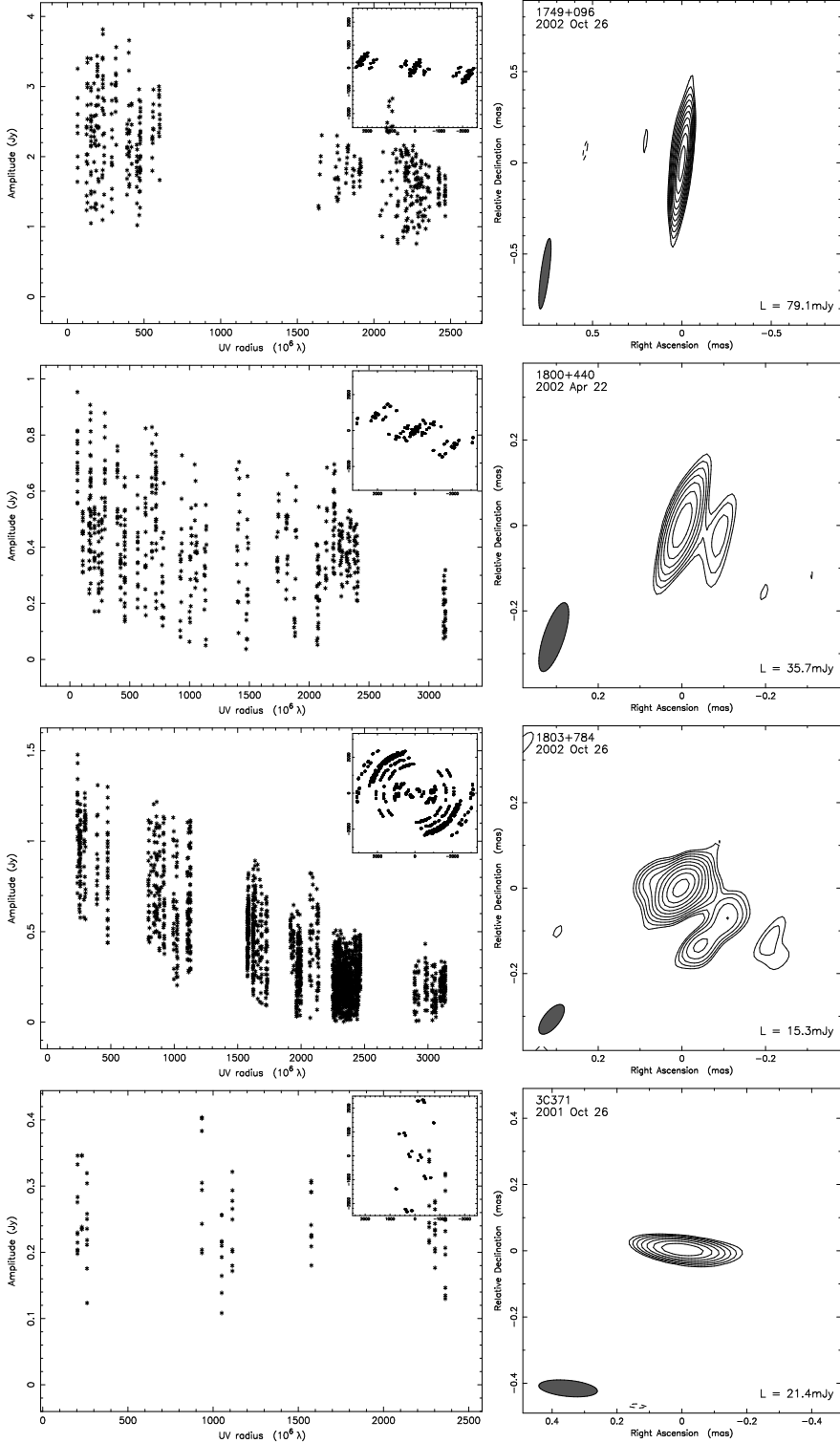


Fig. 6.— *continued.*

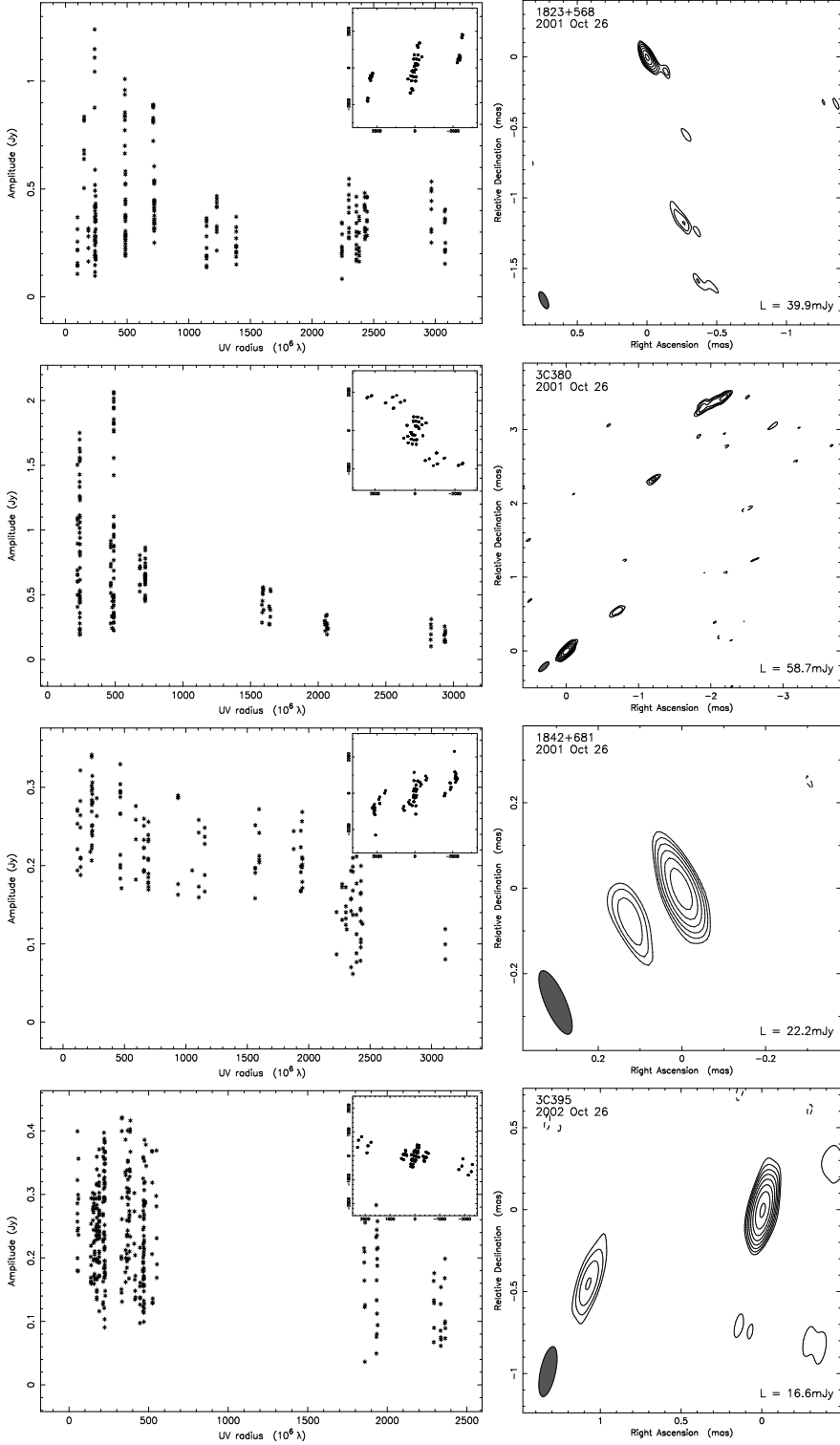


Fig. 6.— *continued.*

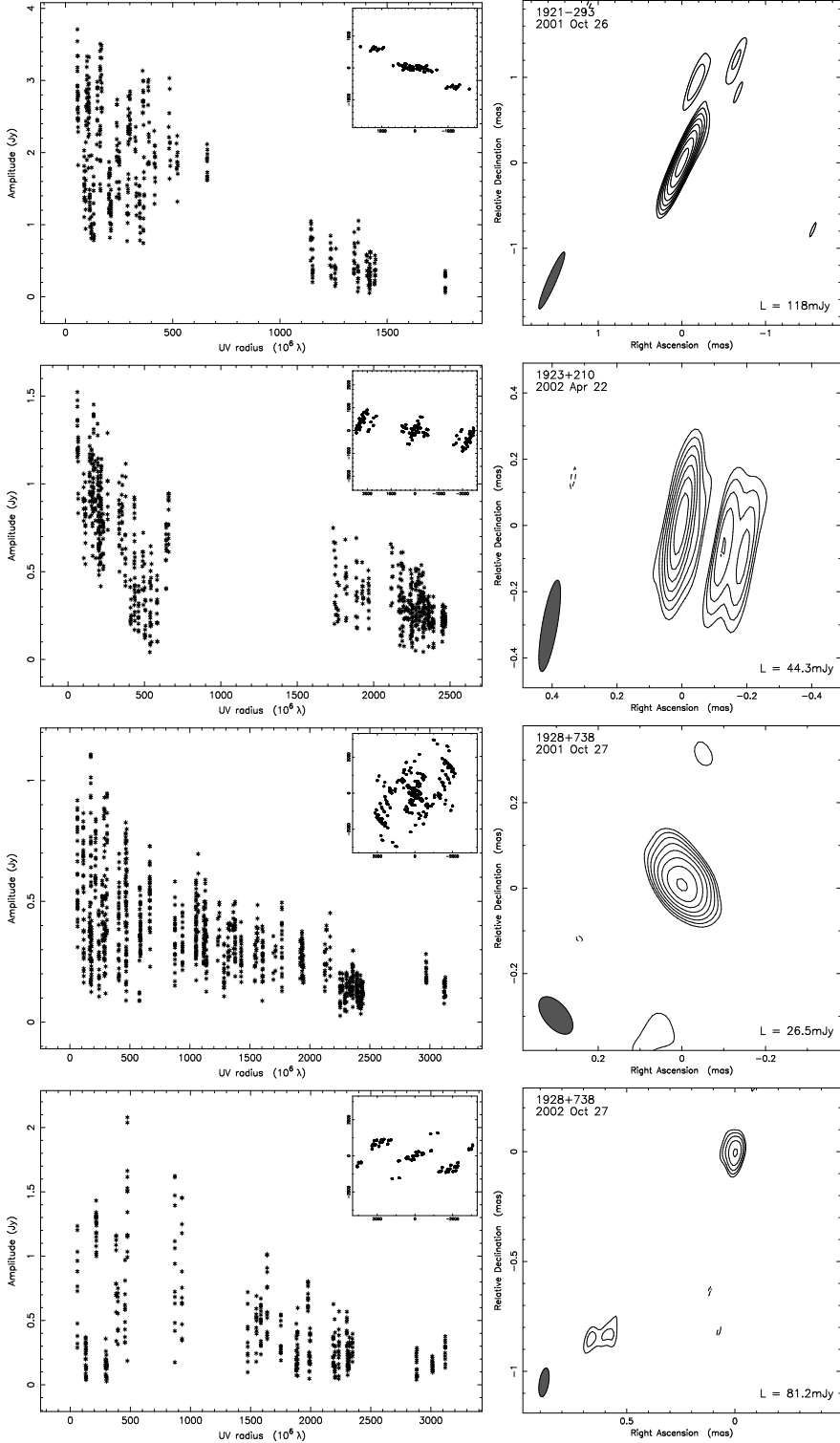


Fig. 6.— *continued.*

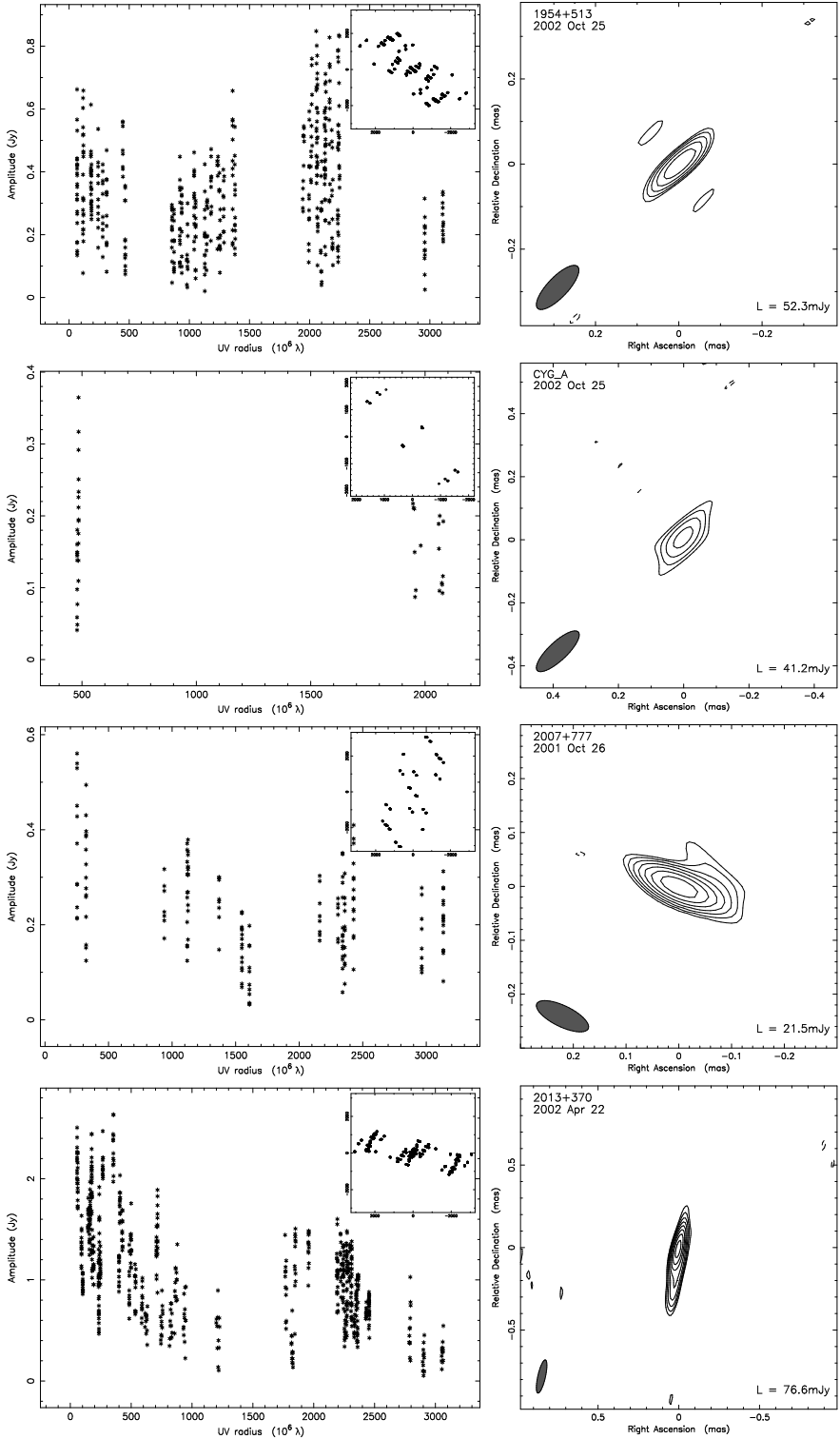


Fig. 6.— *continued.*

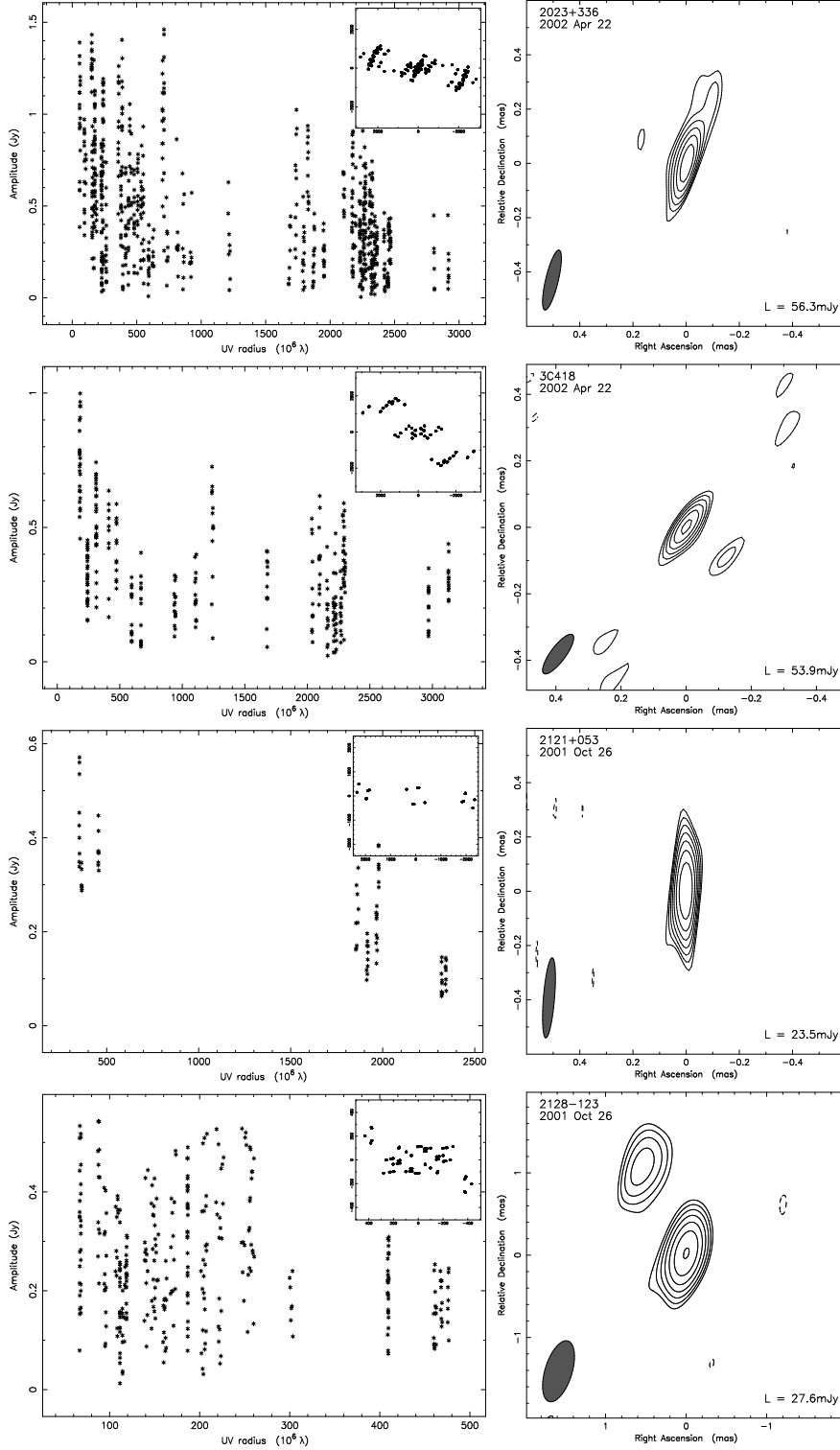


Fig. 6.— *continued.*

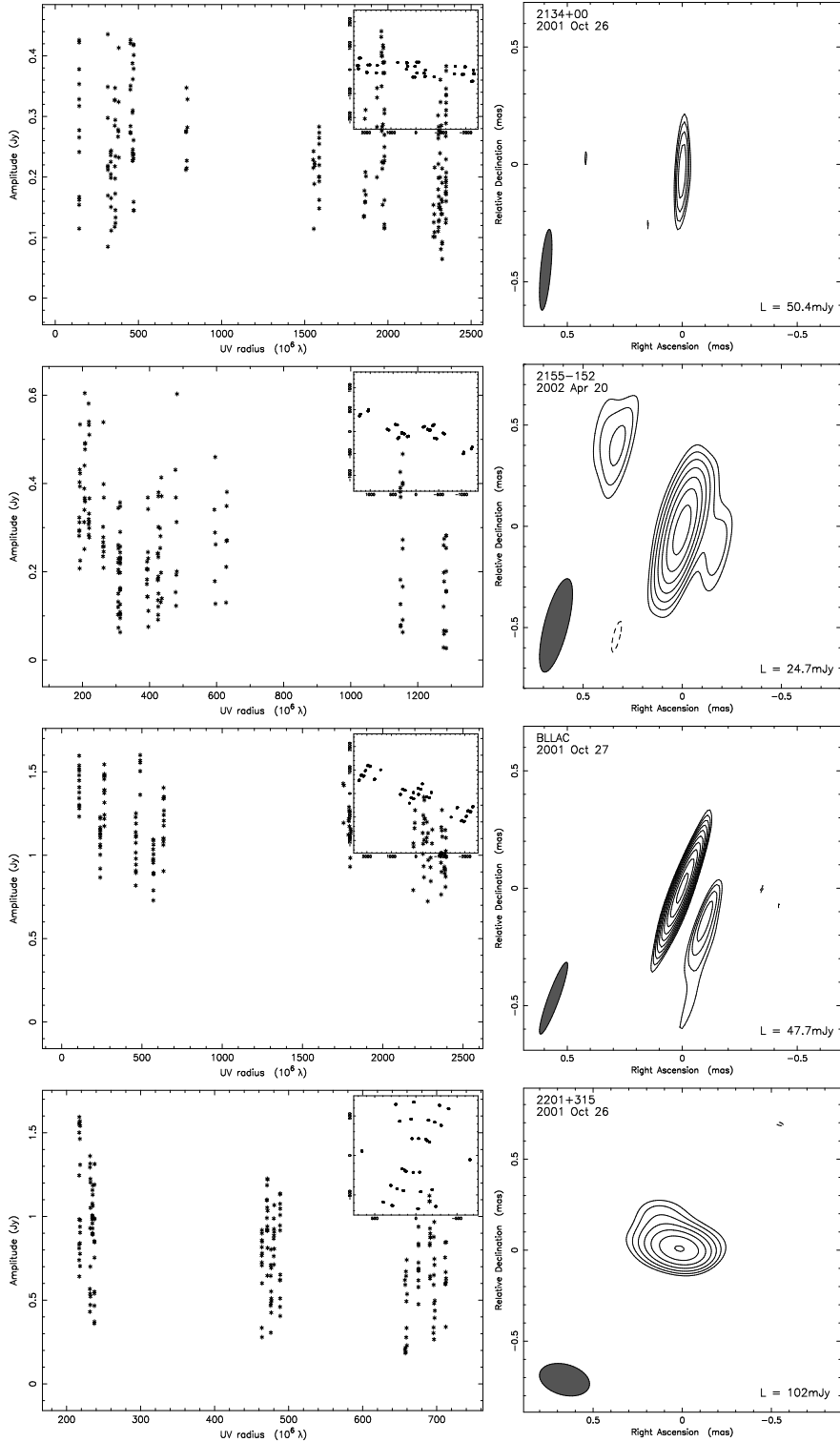


Fig. 6.— *continued.*

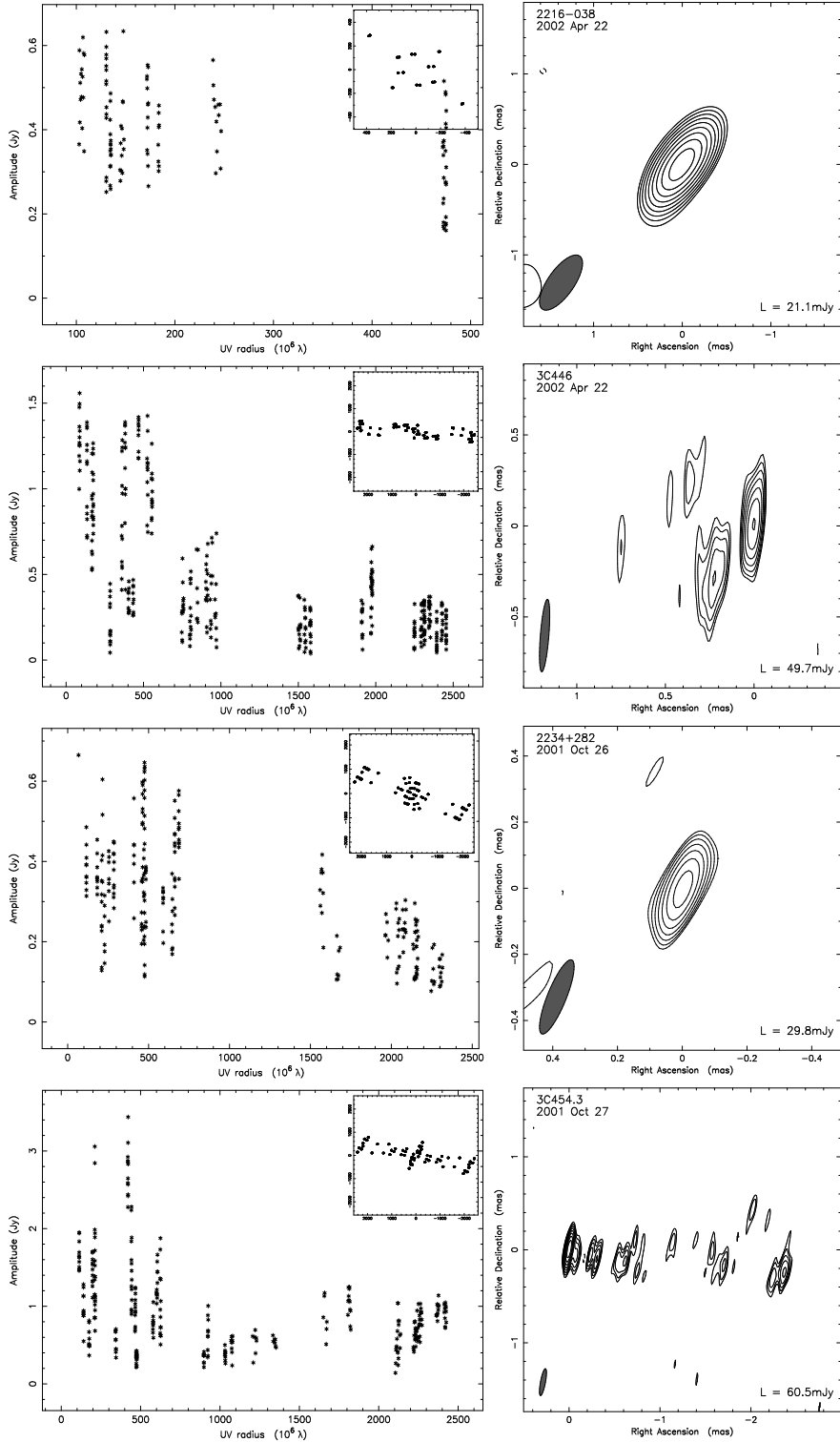


Fig. 6.— *continued.*

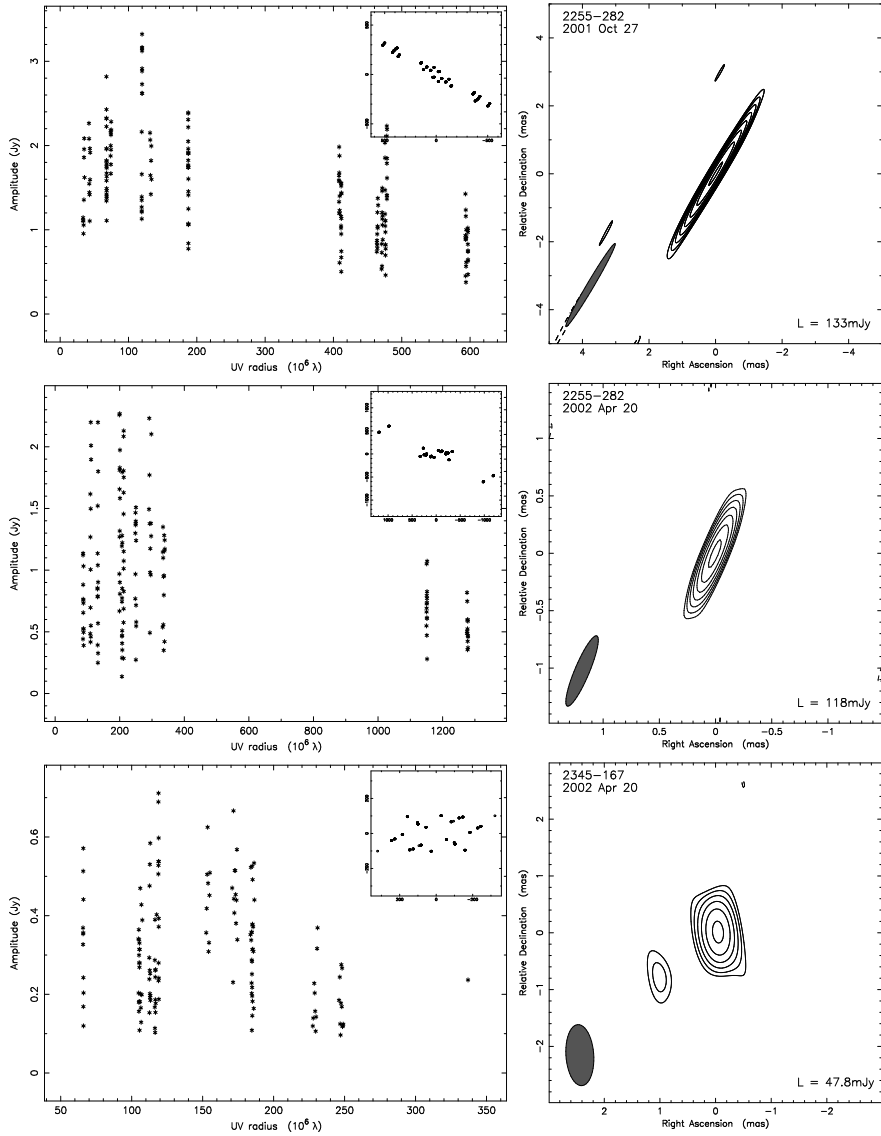


Fig. 6.— *continued.*

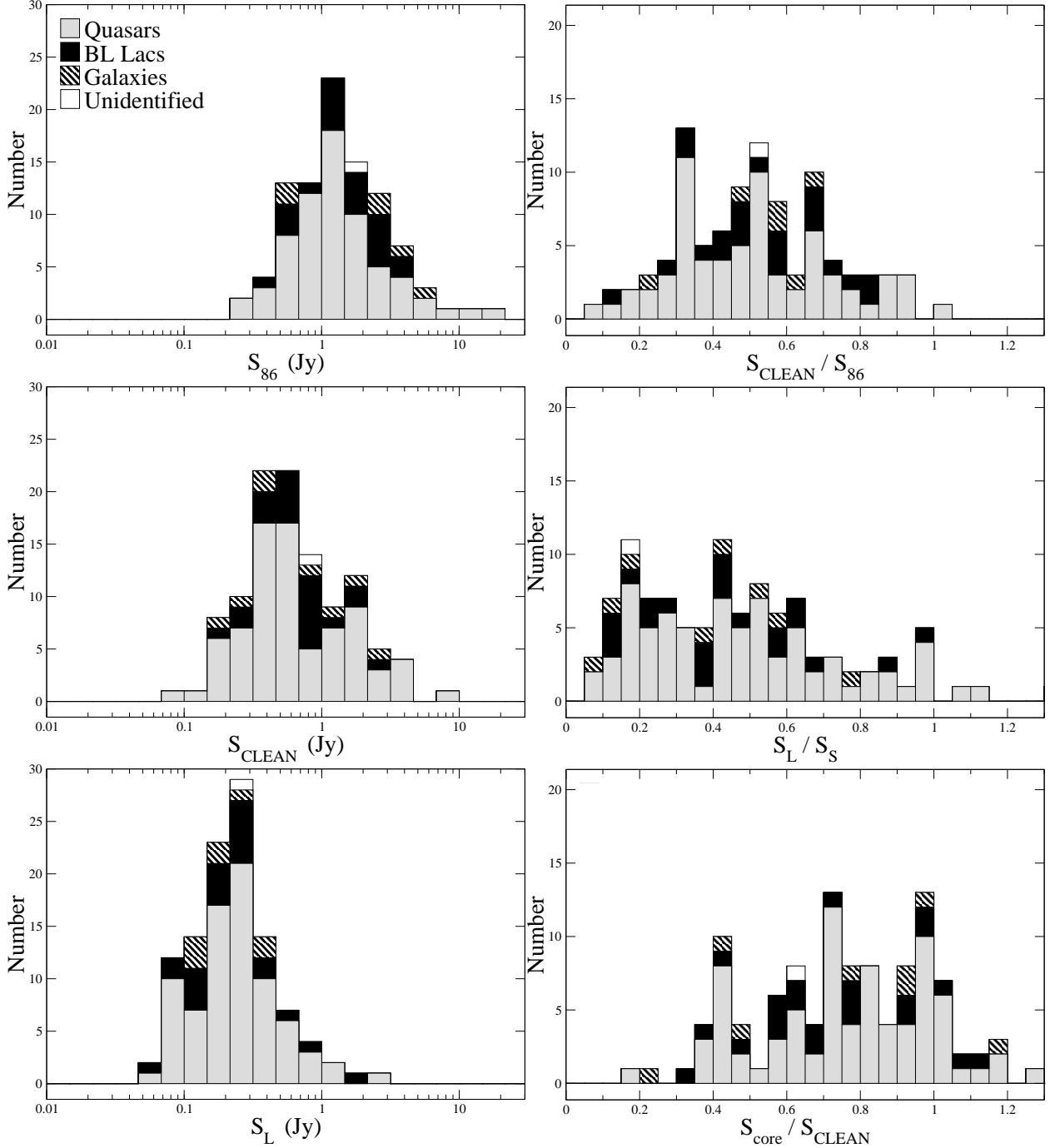


Fig. 7.— Distributions of the total flux density, S_{86} (top left), the CLEAN flux density, S_{CLEAN} (middle left), the correlated flux density on the longest baseline, S_L (bottom left), compactness indices on milliarcsecond scales S_{CLEAN}/S_{86} (top right) and sub-milliarcsecond scales S_L/S_S (middle right), and the core dominance $S_{\text{core}}/S_{\text{CLEAN}}$ of the imaged sources. In the top left panel, sources with the total flux density not available are excluded.

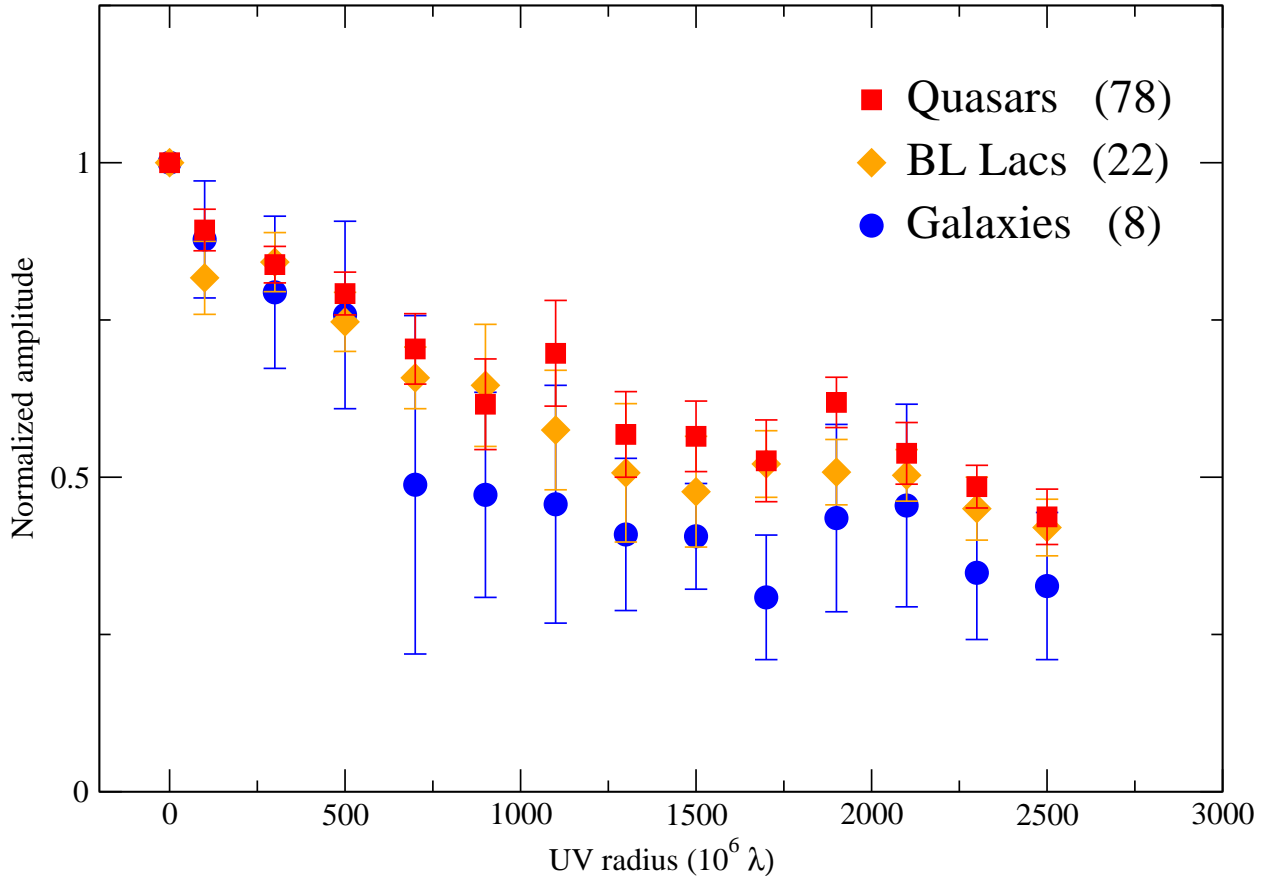


Fig. 8.— Normalized mean amplitude of the visibility function in terms of uv -radius for the survey sample. The visibility amplitude is normalized by the CLEAN flux density S_{CLEAN} for each source (which corresponds to points at $0 M\lambda$), binned with $200 M\lambda$ wide bins ranging from 0 to $2600 M\lambda$, and averaged. Not all bins are sampled for all sources.

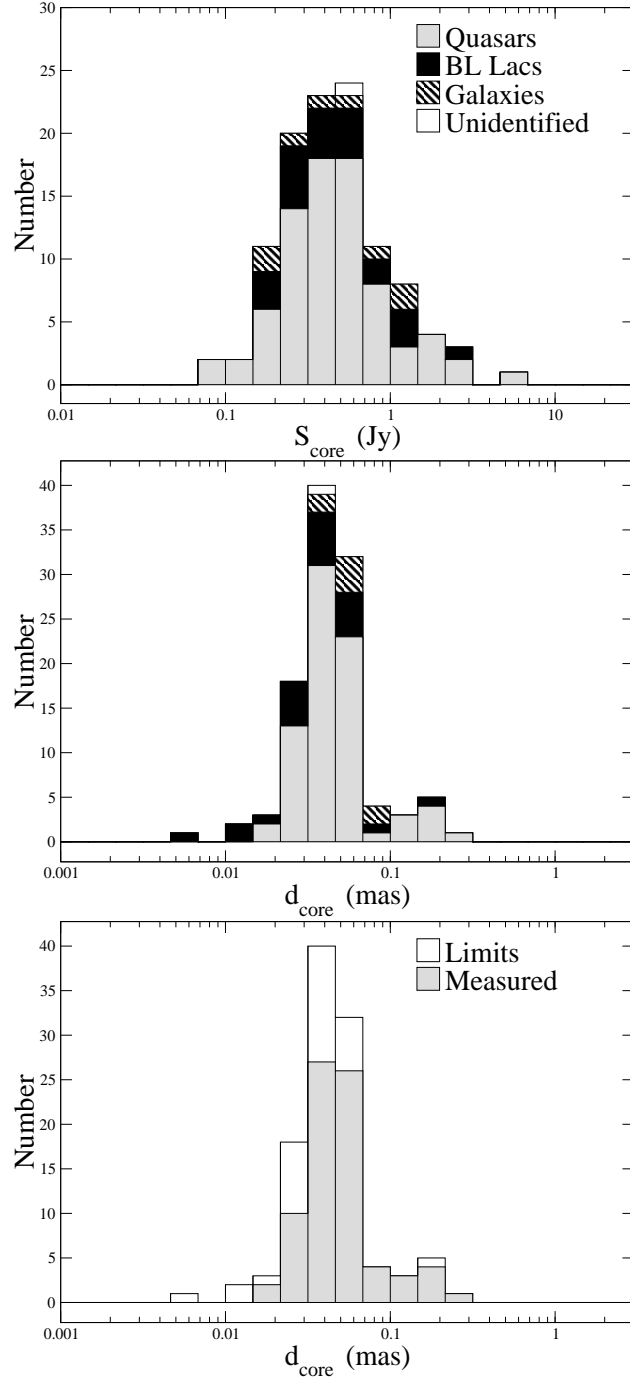


Fig. 9.— Distributions of the flux density (top panel) and the angular size (middle and bottom panel) of the core components for the imaged sources.

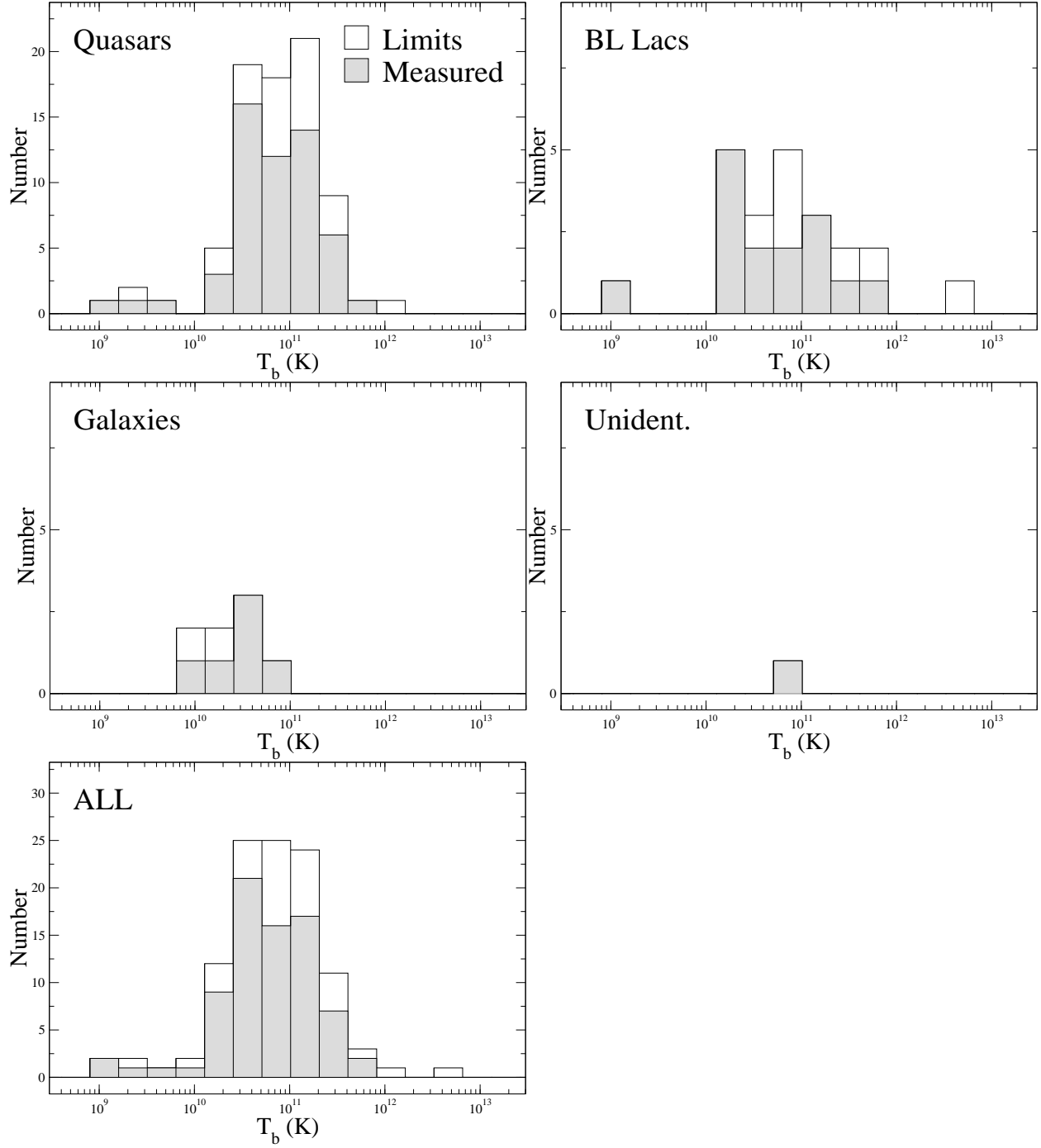


Fig. 10.— Distributions of the measured brightness temperature of the core component in the source frame. The brightness temperature is binned with a size of a factor of 2 in brightness temperature from 1×10^8 K to the maximum value of each sample.

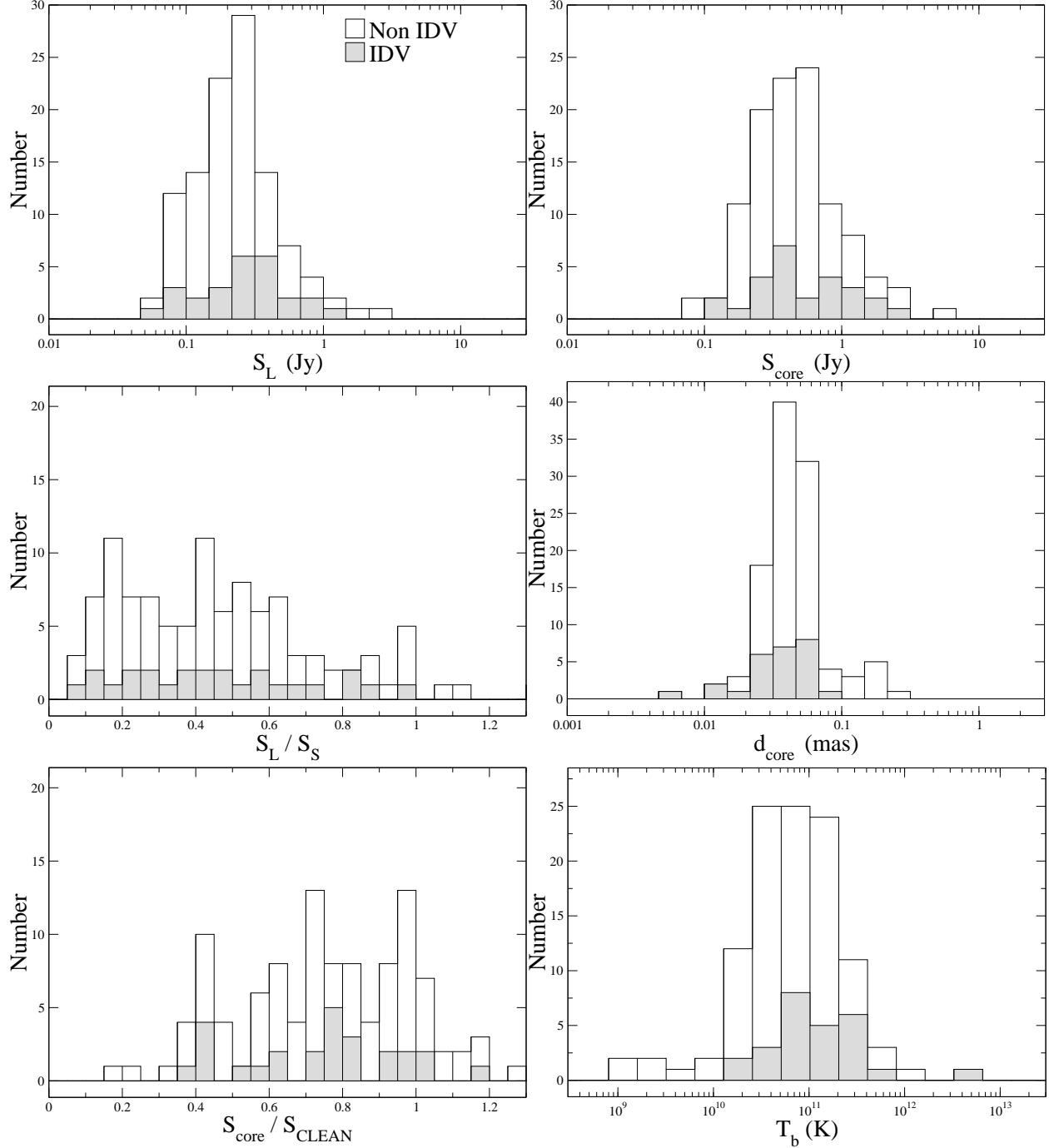


Fig. 11.— Distributions of the correlated flux density at the longest baseline S_L (top left), the compactness index S_L/S_S (middle left), the core dominance S_{core}/S_{CLEAN} (bottom left), the core flux density S_{core} (top right), the size of core component d_{core} (middle right), and the brightness temperature T_b (bottom right) for IDV selected and non-IDV selected sources (see text for reference).

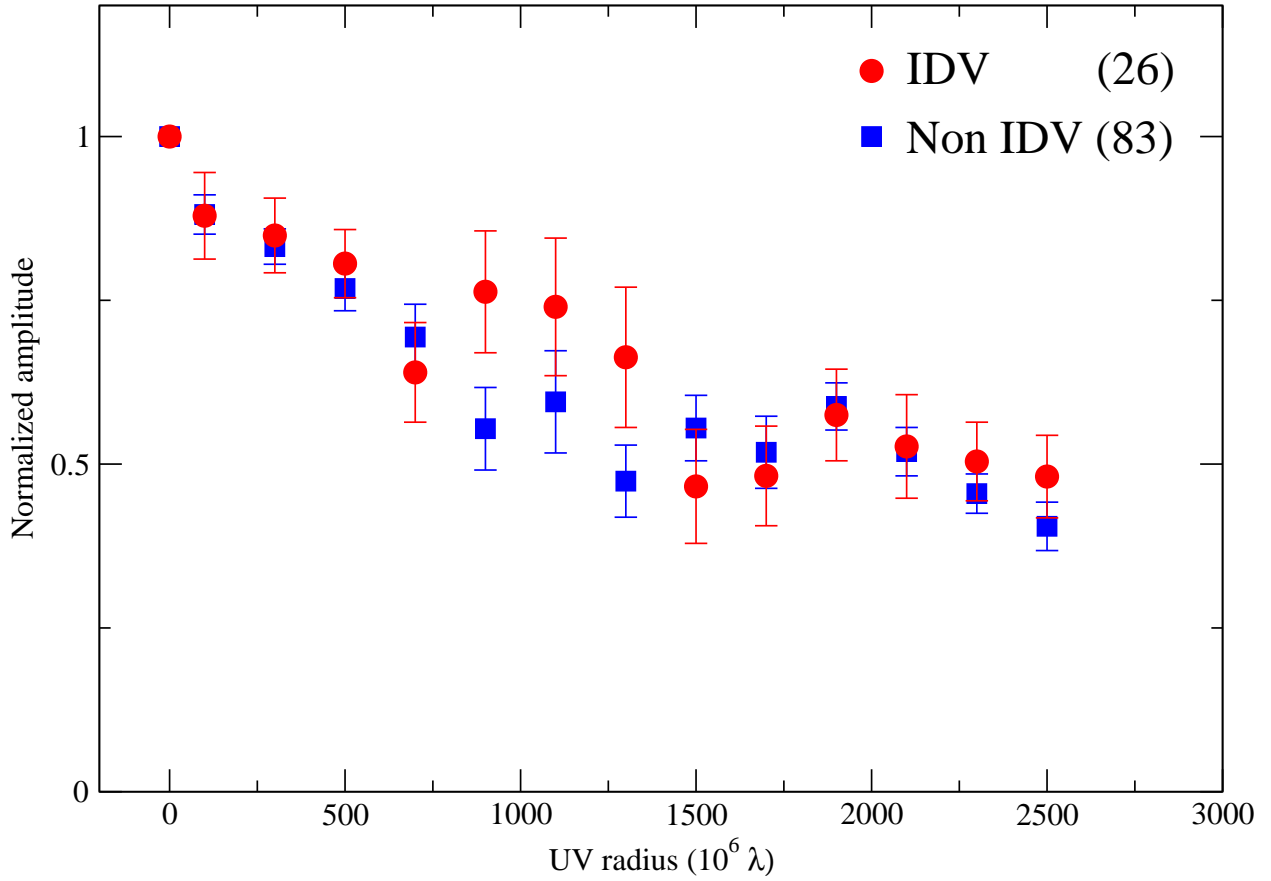


Fig. 12.— Normalized mean amplitude of the visibility function in terms of uv -radius for IDV and non-IDV sources (see text for details). The visibility amplitude is normalized by the CLEAN flux density S_{CLEAN} for each source (which corresponds to a point at $0 M\lambda$), binned with $200 M\lambda$ wide bins ranging from 0 to $2600 M\lambda$, and averaged. Not all bins are sampled for all sources.

Table 1. VLBI Surveys at 86 GHz

Survey (1)	N_{ant} (2)	ΔS (Jy) (3)	ΔI_m (mJy/beam) (4)	D_{img} (5)	N_{obs} (6)	N_{det} (7)	N_{img} (8)
Beasley et al. (1997)	3	~0.5	45	12	...
Lonsdale et al. (1998)	2–5	~0.7	79	14	...
Rantakyro et al. (1998)	6–9	~0.5	~30	70	67	16	12
Lobanov et al. (2000)	3–5	~0.4	~20	100	28	26	17
Total number of unique objects:					124	44	24
Properties of this survey							
	12	~0.2	≤ 10	50	127	121	109

Note. — **Columns:** 1 - references; 2 - number of participating antennas; 3 - average baseline sensitivity; 4 - average image sensitivity; 5 - typical dynamic range of images; 6 - number of sources observed; 7 - number of objects detected; 8 - number of objects imaged.

Table 2. Source List

Source (1)	Name (2)	Epoch (3)	α_{2000} (4)	δ_{2000} (5)	Status (6)	z (7)	Type (8)	m_v (9)	$S_{86\text{ GHz}}$ (10)
0003–066	NRAO 5	C	00 06 13.89289	−06 23 35.3356	++	0.347	B	19.5	2.16
0007+106	III Zw 2	C	00 10 31.00587	+10 58 29.5038	++	0.089	G	15.4	0.60
0016+731		B	00 19 45.78642	+73 27 30.0174	++	1.781	Q	18.0	0.84
0048–097		C	00 50 41.31739	−09 29 05.2103	++	...	B	17.4	0.60
0106+013	4C 01.02	A	01 08 38.77104	+01 35 00.3232	++	2.107	Q	18.3	1.36
0119+041		C	01 21 56.86169	+04 22 24.7343	++	0.637	Q	19.5	0.68
0119+115		C	01 21 41.59504	+11 49 50.4131	++	0.570	Q	19.5	0.68
0133+476		A,B	01 36 58.59481	+47 51 29.1001	++	0.859	Q	18.0	4.25 [†]
0149+218		A,C	01 52 18.05900	+22 07 07.6997	++	1.32	Q	20.8	0.98 [†]
0201+113		C	02 03 46.65706	+11 34 45.4096	++	3.61	Q	20.0	0.39
0202+149	4C 15.05	A	02 04 50.41402	+15 14 11.0453	++	0.405	Q	22.1	...
0202+319		C	02 05 04.92537	+32 12 30.0956	++	1.466	Q	18.2	1.01
0212+735		A,B	02 17 30.81336	+73 49 32.6218	++	2.367	Q	19.0	0.78 [†]
0218+357		C	02 21 05.47330	+35 56 13.7910	++	0.944	Q	20.0	0.58
0221+067		C	02 24 28.42819	+06 59 23.3416	++	0.511	Q	19.0	0.59
0224+671	4C 67.05	B	02 28 50.05146	+67 21 03.0292	++	0.523	Q	19.5	1.34
0234+285	4C 28.07	A,B,C	02 37 52.40568	+28 48 08.9901	++	1.207	Q	18.9	3.11 [†]
0235+164		A	02 38 38.93006	+16 36 59.2789	++	0.940	B	19.0	1.62
0238–084	NGC 1052	B,C	02 41 04.79852	−08 15 20.7518	++	0.005	G	12.1	0.63
0300+470		B	03 03 35.24222	+47 16 16.2754	++	...	B	17.2	3.11
0316+413	3C 84	A,B,C	03 19 48.16010	+41 30 42.1030	++	0.017	G	12.6	4.71 [†]
0333+321	NRAO 140	A	03 36 30.10760	+32 18 29.3430	++	1.263	Q	17.5	1.77
0336–019	CTA 26	A	03 39 30.93771	−01 46 35.8040	++	0.852	Q	18.4	2.11
0355+508	NRAO 150	A,C	03 59 29.74726	+50 57 50.1615	++	...	Q	...	7.18 [†]
0415+379	3C 111	B,C	04 18 21.27700	+38 01 35.9000	++	0.049	G	18.0	2.37 [†]
0420+022		C	04 22 52.21464	+02 19 26.9319	++	2.277	Q	19.5	0.48
0420–014		B	04 23 15.80072	−01 20 33.0653	++	0.915	Q	17.8	5.83
0422+004		B	04 24 46.84205	+00 36 06.3298	++	0.310	B	17.0	1.46
0430+052	3C 120	B,C	04 33 11.09553	+05 21 15.6194	++	0.033	G	14.2	3.19 [†]
0440–003	NRAO 190	C	04 42 38.66076	−00 17 43.4191	++	0.844	Q	19.2	0.88
0458–020	4C −02.19	B	05 01 12.80988	−01 59 14.2562	++	2.291	Q	18.4	1.12
0521–365		C	05 22 57.98463	−36 27 30.8516	++	0.055	G	14.5	...
0528+134		A	05 30 56.41665	+13 31 55.1484	++	2.07	Q	20.0	2.02
0529+075		A	05 32 39.02004	+07 32 43.3466	++	1.254	Q	19.0	1.13
0552+398	DA 193	A	05 55 30.80564	+39 48 49.1654	++	2.363	Q	18.0	1.34
0605–085		A	06 07 59.69905	−08 34 49.9798	+m	0.872	Q	18.5	1.28
0607–157		B	06 09 40.94953	−15 42 40.6726	++	0.324	Q	17.0	...
0642+449		B	06 46 32.02598	+44 51 16.5901	++	3.408	Q	18.5	1.67
0707+476		C	07 10 46.10490	+47 32 11.1426	++	1.292	Q	18.2	0.27
0710+439		C	07 13 38.16412	+43 49 17.2069	−	0.518	G	19.7	0.22
0716+714		B,C	07 21 53.44846	+71 20 36.3633	++	...	B	15.5	3.67 [†]
0727–115		B	07 30 19.11247	−11 41 12.6004	++	1.591	Q	22.5	...
0735+178		B	07 38 07.39374	+17 42 18.9982	++	0.424	B	14.9	1.23
0736+017		A	07 39 18.03380	+01 37 04.6180	++	0.191	Q	16.5	2.24
0738+313		C	07 41 10.70330	+31 12 00.2286	++	0.630	Q	16.7	0.47

Table 2—Continued

Source (1)	Name (2)	Epoch (3)	α_{2000} (4)	δ_{2000} (5)	Status (6)	z (7)	Type (8)	m_v (9)	$S_{86\text{ GHz}}$ (10)
0748+126		B	07 50 52.04573	+12 31 04.8281	++	0.889	Q	17.8	1.80
0804+499		C	08 08 39.66627	+49 50 36.5304	++	1.432	Q	19.1	0.38
0814+425		C	08 18 15.99961	+42 22 45.4149	++	0.530	B	18.5	0.50
0823+033		A	08 25 50.33800	+03 09 24.5100	++	0.506	B	18.5	1.02
0827+243		B	08 30 52.08619	+24 10 59.8204	++	0.941	Q	17.3	2.16
0834-201		C	08 36 39.21522	-20 16 59.5038	+m	2.752	Q	19.4	...
0836+710	4C 71.07	C	08 41 24.36528	+70 53 42.1730	++	2.218	Q	16.5	1.16
0850+581		C	08 54 41.99638	+57 57 29.9392	++	1.322	Q	18.2	0.26
0851+202	OJ 287	B	08 54 48.87492	+20 06 30.6408	++	0.306	B	14.0	2.71
0859+470	OJ 499	C	09 03 03.99010	+46 51 04.1375	++	1.462	Q	19.4	0.42
0906+015		B	09 09 10.09159	+01 21 35.6176	++	1.018	Q	17.3	2.43
0917+624		A	09 21 36.23053	+62 15 52.1763	++	1.446	Q	19.5	1.01
0945+408	4C 40.24	A	09 48 55.33817	+40 39 44.5872	++	1.252	Q	17.9	0.95
0954+658		A	09 58 47.24428	+65 33 54.8108	++	0.367	B	16.7	1.16
1012+232		B	10 14 47.06544	+23 01 16.5709	++	0.565	Q	17.5	1.01
1044+719		B	10 48 27.61991	+71 43 35.9382	++	1.150	Q	19.0	0.87
1101+384	Mk 421	C	11 04 27.31394	+38 12 31.7991	++	0.031	B	13.3	0.58
1128+385		C	11 30 53.28261	+38 15 18.5470	++	1.733	Q	18.6	0.97
1150+497	4C 49.22	C	11 53 24.46664	+49 31 08.8301	++	0.334	Q	17.4	1.02
1156+295	4C 29.45	A	11 59 31.83390	+29 14 43.8295	++	0.729	Q	17.0	4.42
1219+285		C	12 21 31.69051	+28 13 58.5002	++	0.102	B	16.5	0.36
1226+023	3C 273B	A	12 29 06.69973	+02 03 08.5982	++	0.158	Q	12.9	10.81
1228+126	3C 274	A	12 30 49.42338	+12 23 28.0439	++	0.004	G	9.6	4.16
1253-055	3C 279	C	12 56 11.16656	-05 47 21.5246	++	0.538	Q	17.8	16.90
1308+326		A	13 10 28.66372	+32 20 43.7818	++	0.997	Q	19.0	1.44
1418+546		C	14 19 46.59741	+54 23 14.7872	+	0.152	B	15.9	0.93
1458+718	3C 309.1	C	14 59 07.58386	+71 40 19.8677	-	0.904	Q	16.8	0.65
1502+106		C	15 04 24.97978	+10 29 39.1986	++	1.833	Q	18.6	0.82
1504+377		C	15 06 09.52995	+37 30 51.1324	+	0.674	G	21.2	0.51
1508-055		C	15 10 53.59143	-05 43 07.4171	++	1.191	Q	17.2	...
1510-089		C	15 12 50.53292	-09 05 59.8296	++	0.360	Q	16.5	2.10
1511-100		C	15 13 44.89341	-10 12 00.2646	++	1.513	Q	18.5	0.81
1546+027		C	15 49 29.43683	+02 37 01.1632	++	0.412	Q	17.3	1.04
1548+056		C	15 50 35.26924	+05 27 10.4482	++	1.422	Q	17.7	1.71
1606+106		C	16 08 46.20318	+10 29 07.7758	++	1.226	Q	18.5	1.26
1611+343		A	16 13 41.06416	+34 12 47.9093	+m	1.401	Q	17.5	1.83
1633+382	4C 38.41	A	16 35 15.49297	+38 08 04.5006	+m	1.807	Q	17.7	5.81
1637+574		C	16 38 13.45630	+57 20 23.9790	++	0.751	Q	17.0	1.70
1638+398	NRAO 512	C	16 40 29.63277	+39 46 46.0285	+	1.666	Q	18.5	0.50
1641+399	3C 345	A	16 42 58.80995	+39 48 36.9939	+m	0.594	Q	16.6	6.33
1642+690		C	16 42 07.84853	+68 56 39.7564	++	0.751	Q	19.2	1.36
1652+398	DA 426	A	16 53 52.22700	+39 45 36.4500	++	0.033	B	14.2	...
1655+077		C	16 58 09.01145	+07 41 27.5407	++	0.621	Q	20.8	1.00
1739+522		C	17 40 36.97785	+52 11 43.4074	++	1.379	Q	18.5	1.45
1741-038		C	17 43 58.85614	-03 50 04.6168	++	1.057	Q	18.6	4.16

Table 2—Continued

Source (1)	Name (2)	Epoch (3)	α_{2000} (4)	δ_{2000} (5)	Status (6)	z (7)	Type (8)	m_v (9)	$S_{86\text{ GHz}}$ (10)
1749+701	4C 09.57	A	17 48 32.84008	+70 05 50.7705	–	0.770	B	17.0	...
1749+096		C	17 51 32.81857	+09 39 00.7285	++	0.320	B	16.8	4.03
1800+440		B	18 01 32.31485	+44 04 21.9003	++	0.663	Q	17.5	1.07
1803+784		A,C	18 00 45.68364	+78 28 04.0206	++	0.680	B	17.0	1.48
1807+698	3C 371	A	18 06 50.68063	+69 49 28.1087	++	0.050	B	14.4	1.54
1823+568	4C 56.27	A	18 24 07.06809	+56 51 01.4939	++	0.663	B	18.4	1.30
1828+487	3C 380	A	18 29 31.72483	+48 44 46.9515	++	0.692	Q	16.8	1.96
1842+681		A	18 42 33.64129	+68 09 25.2314	++	0.475	Q	17.9	0.74
1901+319	3C 395	C	19 02 55.93886	+31 59 41.7020	++	0.635	Q	17.5	0.59
1921–293		A	19 24 51.05590	–29 14 30.1210	++	0.352	Q	17.0	...
1923+210		B	19 25 59.60537	+21 06 26.1621	++	...	U	16.1	1.73
1928+738		A,C	19 28 00.00000	+73 00 00.0000	++	0.303	Q	16.5	2.52 [†]
1954+513		C	19 55 42.73827	+51 31 48.5462	++	1.223	Q	18.5	0.66
1957+405	Cyg A	C	19 59 28.35400	+40 44 02.1200	++	0.056	G	17.0	...
2005+403		A	20 07 44.94499	+40 29 48.6113	+m	1.736	Q	19.5	1.25
2007+777		A	20 05 30.99883	+77 52 43.2493	++	0.342	B	16.5	0.92
2013+370		B	20 15 28.71260	+37 10 59.6940	++	...	B	21.6	2.89
2021+614		C	20 22 06.68167	+61 36 58.8047	–	0.227	G	19.5	0.58
2023+336		B	20 25 10.84209	+33 43 00.2145	++	0.219	B	...	1.77
2030+407	Cyg X-3	A,B	20 32 25.76740	+40 57 28.2794	–	...	S
2031+405	MWC 349	A	20 30 56.85000	+40 29 20.2000	–	...	U	...	1.17
2037+511	3C 418	B	20 38 37.03475	+51 19 12.6626	++	1.687	Q	20.0	1.44
2121+053		A	21 23 44.51727	+05 35 22.0971	++	1.941	Q	17.5	...
2128–123		A	21 31 35.26150	–12 07 04.7980	++	0.501	Q	15.5	...
2131–021		C	21 34 10.30961	–01 53 17.2393	+	1.285	B	18.7	1.15
2134+004	DA 553	A	21 36 38.58615	+00 41 54.2195	++	1.932	Q	17.1	2.03
2136+141		C	21 39 01.30926	+14 23 35.9921	+m	2.427	Q	18.5	1.03
2155–152		B	21 58 06.28190	–15 01 09.3280	++	0.672	Q	17.5	...
2200+420	BL Lac	A	22 02 43.29138	+42 16 39.9899	++	0.069	B	14.5	3.57
2201+315	4C 31.63	A	22 03 14.97564	+31 45 38.2749	++	0.298	Q	15.5	2.97
2209+236		C	22 12 05.96631	+23 55 40.5438	+m	1.125	Q	19.0	0.68
2216–038		B	22 18 52.03772	–03 35 36.8794	++	0.901	Q	16.5	0.97
2223–052	3C 446	B	22 25 47.25929	–04 57 01.3907	++	1.404	Q	17.2	3.90
2234+282		A	22 36 22.47100	+28 28 57.4200	++	0.795	Q	19.1	1.03
2251+158	3C 454.3	A	22 53 57.74786	+16 08 53.5655	++	0.859	Q	16.1	5.97
2255–282		A,B	22 58 05.96289	–27 58 21.2568	++	0.927	Q	16.8	...
2345–167		B	23 48 02.60851	–16 31 12.0220	++	0.576	Q	17.5	...

Note. — Column designation: 1 - IAU source name; 2 - common name; 3 - observing epochs: **A** - October 2001; **B** - April 2002; **C** - October 2002; 4 , 5 - source coordinates; 6 - status: “–” - not detected; “+” - detected; “+m” - detected and only model fitted; “++” - detected and imaged; 7 - redshift; 8 - optical class: **Q** - quasar; **B** - BL Lac object; **G** - radio galaxy; **S** - star; **U** - unidentified; 9 - optical magnitude; 7 , 8 - information obtained from Véron-Cetty & Véron (2006); 9 - information obtained from NASA/IPAC Extragalactic Database, <http://nedwww.ipac.caltech.edu>; 10 - total flux density [Jy] (obtained from pointing and calibration scan measurements made at Pico Veleta); [†]: mean value of measurements on multiple epochs.

Table 3. Log of Survey Observations

Epoch (1)	Code (2)	Bit Rate (Mbit/s) (3)	Frequency Channels (4)	Sampling (5)	Bandwidth (MHz) (6)	Source (7)	Telescopes (8)
2001 Oct 26-29	A	256	16	1	128	48	VLBA + (Eb,PV,On,Mh,HA)
2002 Apr 20-23	B	256	16	1	128	35	VLBA + (Eb,PV,On,HA)
2002 Oct 24-27	C	256	8	2	64	60	VLBA + (Eb,PV,PdB,HA)

Note. — Column designation: 1 - observation epoch; 2 - code of each epoch; 3 - total recorded bit rate in Mega-bits per second; 4 - number of baseband channels; 5 - sampling mode [bit]; 6 - total observing bandwidth; 7 - number of sources observed (12 of the 127 observed sources were observed during more than one session); 8 - telescopes participating: **VLBA** - Fort Davis, Hancock, North Liberty, Owens Valley, Pie Town, Mauna Kea, Los Alamos, Kitt Peak; **Eb** - Effelsberg; **PV** - Pico Veleta; **On** - Onsala ; **Mh** - Metsähovi; **PdB** - Plateau de Bure ; **HA** - Haystack.

Table 4. Participating telescopes

Name (1)	code (2)	<i>D</i> (m) (3)	<i>G</i> (K/Jy) (4)	<i>T</i> _{sys} (K) (5)	η_A (6)	<i>SEFD</i> (K) (7)	$\Delta^{256,30s}$ (mJy) (8)	Threshold (mJy) (9)
Effelsberg	Eb	100	0.140	130	0.07	929	20	143
Haystack	HA	37	0.058	200	0.15	3448	39	273
Plateau de Bure	PdB	6 × 15	0.180	120	0.65	667	17	121
Pico Veleta	PV	30	0.140	120	0.55	857
Onsala	On	20	0.053	250	0.45	4717	45	321
Metsähovi	Mh	14	0.017	300	0.30	17647	89	621
Fort Davis	Fd	25	0.034	120	0.17	3529	40	278
Hancock	Hn	25	0.035	120	0.17	3429	39	274
North Liberty	Nl	25	0.055	270	0.17	4909	47	328
Owens Valley	Ov	25	0.020	100	0.17	5000	47	331
Pietown	Pt	25	0.024	100	0.17	4167	43	302
Kitt Peak	Kp	25	0.025	110	0.17	4400	44	310
Los Alamos	La	25	0.051	160	0.17	3137	37	262
Mauna Kea	Mk	25	0.023	100	0.17	4348	44	308

Note. — Column designation: 1 - name of the participating telescope; 2 - abbreviation of the telescope name; 3 - diameter; 4 - typical zenith gain; 5 - system temperature; 6 - aperture efficiency; 7 - typical zenith SEFD obtained from the formula, $SEFD = T_{\text{sys}}/G$; 8 - baseline sensitivity on baseline to Pico Veleta, assuming a recording rate of 256 Mbps and a fringe-fit interval of 30 seconds; 9 - 7σ detection threshold.

Table 5. Average antenna gain corrections

Telescope (1)	Session A (2)	Session B (3)	Session C (4)
Eb	0.998 ± 0.129	1.079 ± 0.183	1.354 ± 0.555
HA	1.160 ± 0.179	1.155 ± 0.315	1.180 ± 0.350
PdB	0.964 ± 0.150
PV	0.971 ± 0.157	0.938 ± 0.156	0.952 ± 0.192
On	1.033 ± 0.110	0.956 ± 0.121	...
Mh
Fd	1.215 ± 0.216	1.213 ± 0.298	1.080 ± 0.321
Hn	1.055 ± 0.235
Nl	0.996 ± 0.136	1.003 ± 0.116	1.002 ± 0.231
Ov	1.053 ± 0.158	1.107 ± 0.181	1.079 ± 0.221
Pt	1.139 ± 0.286	1.131 ± 0.284	1.046 ± 0.183
Kp	1.104 ± 0.172	1.059 ± 0.150	1.123 ± 0.259
La	1.009 ± 0.163	1.058 ± 0.266	1.076 ± 0.182
Mk	1.191 ± 0.240	1.543 ± 0.499	1.241 ± 0.268

Note. — Column designation: 1 - abbreviation for the name of telescopes; 2 - average and rms of antenna gains for observing session A; 3 - average and rms of antenna gains for observing session B; 4 - average and rms of antenna gains for observing session C.

Table 6. Image parameters

Name (1)	Obs (2)	S_{86} (3)	S_S (4)	B_S (5)	S_L (6)	B_L (7)	B_a (8)	B_b (9)	B_{PA} (10)	S_t (11)	S_p (12)	σ (13)	ξ_r (14)
0003-066	C	2.16	0.71 ± 0.30	60	0.29 ± 0.16	2450	461	49	-6.2	613	209	17	0.86
0007+106	C	0.60	0.59 ± 0.00	10	0.35 ± 0.06	2470	457	54	-2.7	372	181	9	1.00
0016+731	B	0.84	0.48 ± 0.13	60	0.25 ± 0.08	3130	75	51	-11.6	434	181	8	0.91
0048-097	C	0.60	0.43 ± 0.13	60	0.11 ± 0.06	2440	466	42	-3.3	486	163	6	0.75
0106+013	A	1.36	0.49 ± 0.06	100	0.24 ± 0.05	2390	900	45	-8.6	447	354	15	0.62
0119+041	C	0.68	0.20 ± 0.06	70	0.20 ± 0.09	2390	602	79	-9.9	233	227	9	0.77
0119+115	C	0.68	0.34 ± 0.12	60	0.16 ± 0.06	2390	400	44	-7.1	232	176	10	0.63
0133+476	A	3.96	1.99 ± 0.86	60	0.09 ± 0.03	3140	170	51	-16.4	2148	675	17	0.80
	B	4.53	0.70 ± 0.39	30	1.36 ± 0.54	2430	206	43	5.1	4164	881	20	0.79
0149+218	A	0.96	0.38 ± 0.14	130	0.07 ± 0.04	2450	266	39	-7.1	425	230	12	0.68
	C	0.99	0.41 ± 0.12	50	0.06 ± 0.03	2420	262	50	-5.4	529	278	10	0.77
0201+113	C	0.39	0.27 ± 0.10	60	0.16 ± 0.05	2470	455	47	-2.6	212	159	8	0.66
0202+149	A	...	0.32 ± 0.08	140	0.21 ± 0.04	2470	381	44	-6.0	370	193	9	0.81
0202+319	C	1.01	0.59 ± 0.16	60	0.10 ± 0.05	3140	230	44	-15.3	684	263	8	0.84
0212+735	A	0.77	0.16 ± 0.06	60	0.11 ± 0.03	2960	109	48	-44.5	174	136	4	0.87
	B	0.79	0.33 ± 0.14	230	0.20 ± 0.07	670	1354	151	-65.3	430	229	11	0.49
0218+357	C	0.58	0.14 ± 0.04	60	0.11 ± 0.03	3140	229	43	-17.2	182	109	4	0.90
0221+067	C	0.59	0.42 ± 0.06	110	0.11 ± 0.02	2470	582	68	-0.2	357	272	25	0.59
0224+671	B	1.34	0.27 ± 0.10	40	0.29 ± 0.06	2380	183	50	38.5	362	209	9	1.04
0234+285	A	2.98	2.07 ± 0.30	210	0.13 ± 0.07	2380	215	37	-3.3	2110	549	12	0.95
	B	3.24	2.44 ± 0.48	210	0.17 ± 0.06	2310	218	42	2.9	2691	1073	25	0.74
	C	...	1.47 ± 0.20	60	0.24 ± 0.04	2460	466	53	-6.4	1662	931	38	0.75
0235+164	A	1.62	0.99 ± 0.30	410	0.45 ± 0.06	2470	298	37	2.1	966	482	22	0.73
0238-084	B	...	0.27 ± 0.06	250	0.08 ± 0.02	2420	425	35	-6.2	246	155	8	0.74
	C	0.63	0.33 ± 0.11	60	0.12 ± 0.00	2430	1001	51	-4.7	307	247	9	0.67
0300+470	B	3.11	0.91 ± 0.15	240	0.13 ± 0.05	2460	178	36	-9.5	953	377	4	0.99
0316+413	A	4.76	1.84 ± 0.28	60	0.21 ± 0.07	2470	203	43	-15.6	2849	426	20	1.20
	B	4.80	1.23 ± 0.51	30	0.22 ± 0.09	2380	353	61	-1.1	1530	419	12	0.76
	C	4.56	0.90 ± 0.20	60	0.17 ± 0.06	3140	187	47	-23.7	1347	339	8	0.94
0333+321	A	1.77	0.42 ± 0.16	210	0.34 ± 0.07	2440	211	42	-2.6	624	273	16	0.98
0336-019	A	2.11	1.09 ± 0.60	300	0.22 ± 0.03	2280	368	52	-3.4	1971	461	14	0.69
0355+508	A	6.76	3.86 ± 0.79	60	0.27 ± 0.06	3140	150	47	-28.6	4198	653	47	0.82
	C	7.59	4.03 ± 0.40	70	1.36 ± 0.54	1470	697	90	-31.3	4140	2487	95	1.01
0415+379	B	2.17	0.56 ± 0.26	90	0.18 ± 0.06	2460	203	44	-7.9	2696	508	24	0.77
	C	2.57	1.53 ± 0.23	60	0.13 ± 0.07	3120	220	42	-16.7	1445	375	30	0.69
0420+022	C	0.48	0.33 ± 0.15	60	0.10 ± 0.04	2470	684	51	-0.7	234	161	7	0.76
0420-014	B	5.83	1.42 ± 0.89	50	0.48 ± 0.12	2470	445	48	-5.8	1866	879	43	0.84
0422+004	B	1.46	0.62 ± 0.25	60	0.37 ± 0.09	2460	438	48	-5.3	667	409	12	0.92
0430+052	B	4.05	0.14 ± 0.08	100	0.20 ± 0.05	2460	359	43	-5.7	3585	555	26	0.71
	C	2.32	0.87 ± 0.12	60	0.39 ± 0.07	2460	594	56	-0.8	1523	542	16	0.77
0440-003	C	0.88	0.37 ± 0.12	70	0.31 ± 0.06	2470	497	56	-2.4	481	337	12	0.87
0458-020	B	1.12	0.50 ± 0.18	50	0.17 ± 0.04	2460	433	49	-5.4	501	357	9	0.77
0521-365	C	...	0.43 ± 0.17	40	0.22 ± 0.09	1400	1196	150	-13.5	330	297	18	0.53
0528+134	A	2.02	0.54 ± 0.06	140	0.29 ± 0.05	2410	336	50	-1.3	1051	391	6	0.82

Table 6—Continued

Name (1)	Obs (2)	S_{86} (3)	S_S (4)	B_S (5)	S_L (6)	B_L (7)	B_a (8)	B_b (9)	B_{PA} (10)	S_t (11)	S_p (12)	σ (13)	ξ_r (14)
0529+075	A	1.13	0.29 ± 0.07	270	0.25 ± 0.07	2250	840	52	2.9	267	260	20	0.68
0552+398	A	1.34	0.72 ± 0.12	60	0.15 ± 0.03	2470	248	41	-9.9	778	348	11	0.77
0607-157	B	...	1.00 ± 0.40	60	0.41 ± 0.14	1350	718	127	-23.9	1188	798	16	0.84
0642+449	B	1.67	1.16 ± 0.11	60	0.18 ± 0.05	2470	214	43	-6.1	1295	486	7	0.73
0707+476	C	0.27	0.08 ± 0.02	330	0.08 ± 0.02	2470	255	37	-4.9	75	72	3	0.67
0716+714	B	1.16	0.51 ± 0.10	50	0.29 ± 0.04	2470	141	49	3.5	565	369	12	0.92
	C	2.51	0.61 ± 0.43	100	0.61 ± 0.06	3120	122	40	-15.9	1020	865	29	0.89
0727-115	B	...	0.65 ± 0.24	70	0.45 ± 0.15	620	928	265	-21.8	675	545	25	0.69
0735+178	B	1.23	0.30 ± 0.11	50	0.12 ± 0.05	2390	315	42	-0.5	629	141	5	0.71
0736+017	A	2.24	1.36 ± 0.48	320	0.24 ± 0.09	2400	341	49	-1.9	1990	577	18	0.79
0738+313	C	0.47	0.41 ± 0.08	30	0.08 ± 0.04	2320	303	51	6.1	439	254	8	0.81
0748+126	B	1.80	0.52 ± 0.20	270	0.33 ± 0.09	2400	333	42	-2.0	1628	506	14	0.84
0804+499	C	0.38	0.20 ± 0.07	40	0.10 ± 0.04	2360	213	40	0.0	175	113	4	0.71
0814+425	C	0.50	0.39 ± 0.10	40	0.05 ± 0.01	2380	232	43	2.8	409	178	7	0.74
0823+033	A	1.02	0.59 ± 0.09	60	0.15 ± 0.05	2400	348	39	-3.6	590	239	8	0.71
0827+243	B	2.16	0.55 ± 0.16	70	0.50 ± 0.06	2380	314	54	-19.7	720	535	13	1.02
0836+710	C	1.16	0.39 ± 0.11	90	0.16 ± 0.09	3000	156	62	21.1	451	361	14	0.85
0850+581	C	0.26	0.14 ± 0.01	50	0.09 ± 0.03	2470	247	37	-13.8	165	72	4	0.83
0851+202	B	2.71	0.60 ± 0.20	60	0.29 ± 0.12	3140	366	52	-12.0	901	505	19	0.83
0859+470	C	0.42	0.33 ± 0.09	40	0.14 ± 0.03	2330	230	43	10.5	306	174	8	0.88
0906+015	B	2.43	0.73 ± 0.29	60	0.36 ± 0.09	2470	452	46	-5.1	649	488	16	0.86
0917+624	A	1.01	0.27 ± 0.12	50	0.07 ± 0.04	2350	154	44	-16.8	142	116	6	0.92
0945+408	A	0.95	0.11 ± 0.06	170	0.22 ± 0.07	2890	180	46	-16.8	798	229	13	0.93
0954+658	A	1.16	0.43 ± 0.12	50	0.27 ± 0.02	3040	144	45	-4.0	784	336	8	0.95
1012+232	B	1.01	0.77 ± 0.11	60	0.09 ± 0.05	3110	345	41	-12.4	693	191	7	0.99
1044+719	B	0.87	0.26 ± 0.14	60	0.30 ± 0.06	2470	218	49	-30.2	204	181	8	0.92
1101+384	C	0.58	0.33 ± 0.09	90	0.12 ± 0.03	2470	220	44	-6.8	407	169	5	0.84
1128+385	C	0.97	0.44 ± 0.19	170	0.10 ± 0.03	3140	213	43	-2.0	482	258	10	0.74
1150+497	C	1.02	0.46 ± 0.14	160	0.33 ± 0.14	2390	284	48	13.1	616	392	11	0.92
1156+295	A	4.42	2.97 ± 0.62	220	0.93 ± 0.21	2470	188	37	-8.5	3006	1176	28	0.97
1219+285	C	0.36	0.23 ± 0.06	50	0.09 ± 0.01	2470	343	38	-5.3	179	104	3	0.75
1226+023	A	10.81	2.05 ± 0.33	100	0.32 ± 0.17	2440	439	54	-5.5	2160	630	27	0.65
1228+126	A	4.16	0.94 ± 0.16	180	0.16 ± 0.07	1590	198	78	-4.8	897	568	35	0.61
1253-055	C	16.90	2.32 ± 0.83	70	3.04 ± 0.54	2460	440	56	-4.3	8653	4286	158	1.29
1308+326	A	1.44	0.45 ± 0.07	150	0.44 ± 0.05	2330	215	46	1.4	734	466	12	0.76
1502+106	C	0.82	0.45 ± 0.12	150	0.28 ± 0.02	2450	440	47	-2.3	564	298	11	0.76
1508-055	C	...	0.49 ± 0.15	130	0.16 ± 0.07	2310	469	45	-0.3	1192	285	16	0.62
1510-089	C	2.10	0.67 ± 0.24	130	0.66 ± 0.10	2350	400	42	-4.7	1864	576	46	0.69
1511-100	C	0.81	0.64 ± 0.15	120	0.18 ± 0.03	2440	580	40	-1.3	598	264	16	0.67
1546+027	C	1.04	0.50 ± 0.26	140	0.28 ± 0.07	2470	407	44	-4.0	436	220	19	0.74
1548+056	C	1.71	0.63 ± 0.16	260	0.18 ± 0.07	2470	464	44	-2.8	551	248	12	0.84
1606+106	C	1.26	0.37 ± 0.10	70	0.53 ± 0.11	3140	401	52	-10.1	397	344	16	0.98
1637+574	C	1.70	1.13 ± 0.37	110	0.61 ± 0.08	3130	118	36	-58.1	1186	741	12	1.10
1642+690	C	1.36	0.50 ± 0.11	60	0.23 ± 0.09	3140	107	43	-59.9	512	360	12	1.11
1652+398	A	...	0.24 ± 0.09	230	0.10 ± 0.05	720	805	145	78.7	245	159	10	0.57

Table 6—Continued

Name (1)	Obs (2)	S_{86} (3)	S_S (4)	B_S (5)	S_L (6)	B_L (7)	B_a (8)	B_b (9)	B_{PA} (10)	S_t (11)	S_p (12)	σ (13)	ξ_r (14)
1655+077	C	1.00	0.49 ± 0.22	130	0.27 ± 0.08	2470	381	44	-7.4	569	330	11	0.85
1739+522	C	1.45	1.12 ± 0.11	320	0.45 ± 0.08	3140	115	35	-46.6	1030	693	8	0.96
1741-038	C	4.16	3.73 ± 0.58	160	0.34 ± 0.13	2470	448	38	-4.7	3210	1293	41	0.87
1749+096	C	4.03	2.37 ± 0.50	70	1.47 ± 0.14	2470	390	46	-7.6	2388	1978	26	0.89
1800+440	B	1.07	0.71 ± 0.11	60	0.18 ± 0.07	3140	170	49	-18.8	508	357	11	1.00
1803+784	C	1.48	1.00 ± 0.19	240	0.21 ± 0.06	3140	85	38	-39.4	996	382	5	0.89
1807+698	A	1.54	0.25 ± 0.05	200	0.22 ± 0.07	2360	181	49	84.7	231	225	7	0.75
1823+568	A	1.30	0.21 ± 0.08	100	0.29 ± 0.09	3080	130	50	24.5	1000	332	14	0.91
1828+487	A	1.96	0.87 ± 0.45	220	0.18 ± 0.04	2940	182	65	-47.2	1995	587	19	0.76
1842+681	A	0.74	0.24 ± 0.03	120	0.10 ± 0.02	3110	162	50	24.1	259	159	7	0.79
1901+319	C	0.59	0.27 ± 0.06	50	0.12 ± 0.05	2370	312	94	-12.3	248	185	6	0.70
1921-293	A	...	2.78 ± 0.41	60	0.22 ± 0.11	1770	727	102	-24.0	2896	1477	44	0.67
1923+210	B	1.73	1.22 ± 0.17	60	0.23 ± 0.04	2470	280	46	-10.1	919	443	13	0.93
1928+738	A	2.60	0.62 ± 0.18	60	0.14 ± 0.03	3130	106	57	41.1	487	294	9	0.86
	C	2.43	0.75 ± 0.33	60	0.27 ± 0.07	3120	132	43	-9.6	1383	325	24	0.85
1954+513	C	0.66	0.35 ± 0.13	70	0.25 ± 0.05	3110	137	49	-44.4	354	276	13	1.06
1957+405	C	...	0.17 ± 0.08	480	0.13 ± 0.04	2080	175	58	-45.5	192	133	22	0.57
2007+777	A	0.92	0.37 ± 0.13	250	0.21 ± 0.06	3130	108	39	64.8	352	215	6	1.00
2013+370	B	2.89	2.07 ± 0.21	60	0.29 ± 0.10	3070	206	47	-13.0	2083	958	26	0.89
2023+336	B	1.77	0.98 ± 0.27	60	0.18 ± 0.12	2920	227	48	-13.7	825	402	19	0.82
2037+511	B	1.44	0.74 ± 0.14	180	0.31 ± 0.06	3130	146	46	-37.3	596	317	16	0.87
2121+053	A	...	0.39 ± 0.10	350	0.11 ± 0.02	2350	296	42	-4.7	391	247	14	0.62
2128-123	A	...	0.31 ± 0.13	70	0.17 ± 0.05	480	772	335	-17.8	338	212	10	0.72
2134+004	A	2.03	0.28 ± 0.10	140	0.25 ± 0.08	2350	346	44	-5.3	186	187	18	0.68
2155-152	B	...	0.38 ± 0.10	190	0.16 ± 0.09	1280	476	119	-14.7	369	224	7	0.74
2200+420	A	3.57	1.41 ± 0.11	110	0.96 ± 0.09	2400	326	48	-20.5	1495	1137	17	0.67
2201+315	A	2.97	1.02 ± 0.31	220	0.60 ± 0.19	710	287	169	75.3	1098	783	30	0.78
2216-038	B	0.97	0.50 ± 0.08	100	0.31 ± 0.11	480	722	294	-35.9	444	391	11	0.54
2223-052	B	3.90	1.29 ± 0.15	80	0.19 ± 0.07	2460	399	48	-4.7	1556	382	17	0.76
2234+282	A	1.03	0.66 ± 0.00	70	0.13 ± 0.03	2320	242	58	-22.5	365	271	13	0.77
2251+158	A	5.97	1.67 ± 0.17	110	0.92 ± 0.11	2430	292	55	-10.8	4084	865	18	0.86
2255-282	A	...	1.56 ± 0.40	30	0.84 ± 0.26	600	2856	207	-31.1	1861	1475	45	0.69
	B	...	0.73 ± 0.24	90	0.53 ± 0.13	1280	666	129	-23.3	1007	981	51	0.70
2345-167	B	...	0.33 ± 0.14	70	0.24 ± 0.00	340	1077	500	4.0	349	281	16	0.58

Note. — Column designation: 1 - source name; 2 - observing epochs: **A** - October 2001; **B** - April 2002; **C** - October 2002; 3 - total flux density [Jy] (obtained from pointing and calibration scan measurements made at Pico Veleta); 4,6 - correlated flux density [Jy] measured on baselines 5,7 [M λ]; 8-10 - restoring beam: 8 - major axis [μ as]; 9 - minor axis [μ as]; 10 - position angle of the major axis [°]; 11 - total CLEAN flux density [mJy]; 12 - peak flux density [mJy/beam]; 13 - off-source RMS in the image [mJy/beam]; 14 - quality of the residual noise in the image.

Table 7. Model fit parameters of sources

Name (1)	Obs (2)	S_{tot} (3)	S_{peak} (4)	d (5)	r (6)	θ (7)	T_b (8)
0003−066	C	210±89	193±60	< 40	> 2.9
		203±78	138±44	48±15	580±8	-3.0± 0.8	1.9±1.2
		88±42	87±30	< 46	804±8	5.1± 0.6	> 0.91
0007+106	C	185±93	196±67	< 53	> 1.2
		48±63	65±51	< 155	461±60	-138.3± 7.4	> 0.036
0016+731	B	312±293	197±157	< 28	> 18
		51±51	56±38	65±44	115±22	114.6±10.8	0.55±0.77
0048−097	C	268±73	179±41	42±10	2.5±1.1
		63±32	53±20	< 42	266±8	6.3± 1.7	> 0.6
		76±77	44±38	127±111	760±55	7.7± 4.2	0.077±0.14
0106+013	A	431±125	351±79	36±8	17±7.7
0119+041	C	217±98	228±71	< 65	> 1.4
0119+115	C	201±72	184±48	< 30	> 5.9
0133+476	A	971±180	689±104	47±7	13±4.1
		284±86	194±48	51±13	97±6	-70.2± 3.7	3.3±1.7
		464±336	154±106	212±146	822±73	-10.7± 5.1	0.32±0.43
0133+476	B	1771±725	1060±372	47±16	24±17
		670±581	179±150	206±172	1247±86	-1.9± 4.0	0.48±0.81
		267±236	171±127	194±144	1807±72	-14.3± 2.3	0.22±0.33
		301±313	95±94	317±314	2803±157	-26.1± 3.2	0.091±0.18
0149+218	A	208±190	138±105	498±380	3776±190	-29.9± 2.9	0.026±0.039
		427±149	184±59	66±21	3.7±2.4
		494±209	303±109	61±22	5.1±3.6
0201+113	C	160±26	159±18	< 15	> 51
		58±25	38±14	62±22	315±11	-20.8± 2.0	1.1±0.82
0202+149	A	246±119	183±71	< 34	> 4.8
		132±66	57±26	81±37	78±19	-93.6±13.4	0.46±0.43
0202+319	C	532±288	269±130	62±30	5.6±5.4
		116±81	80±46	< 36	89±10	65.1± 6.7	> 3.5
0212+735	A	162±20	137±13	29±3	11±2
		164±98	184±73	< 184	> 0.27
0218+357	C	359±345	77±72	457±429	668±214	113.5±17.8	0.095±0.18
		154±94	118±57	< 34	> 4.3
		355±89	299±57	48±9	3.8±1.5
0221+067	C	287±178	219±108	< 33	> 6.6
0234+285	A	1250±504	368±142	65±25	11±8.3
		80±84	69±55	< 55	84±22	128.1±14.6	> 0.96
		611±318	217±106	61±30	139±15	20.3± 6.1	6±5.8
0234+285	B	423±384	101±89	83±73	150±37	-161.5±13.7	2.2±3.9
		1312±349	604±146	66±16	11±5.3
		672±350	260±126	86±42	76±21	12.2±15.4	3.3±3.2
0234+285	C	505±303	302±155	61±31	121±16	-170.9± 7.4	4.9±5.1
		986±207	799±131	39±6	24±7.7
		485±50	392±31	42±3	240±2	-32.2± 0.4	10±1.6
		218±24	172±15	45±4	838±2	-17.8± 0.1	3.9±0.67

Table 7—Continued

Name (1)	Obs (2)	S_{tot} (3)	S_{peak} (4)	d (5)	r (6)	θ (7)	T_b (8)
0235+164	A	385±74	388±52	< 13	> 69
		678±401	158±91	83±48	68±24	-89.6±19.4	3.1±3.6
0238-084	B	267±86	142±40	47±13	2±1.1
0238-084	C	292±100	252±65	< 47	> 2.2
0300+470	B	965±317	260±82	73±23	3±1.9
		63±56	40±30	54±40	276±20	126.3± 4.2	0.35±0.54
0316+413	A	724±167	431±86	51±10	4.7±1.9
		247±109	192±67	41±14	161±7	140.3± 2.5	2.5±1.7
		813±383	198±91	238±109	438±55	175.9± 7.1	0.24±0.22
		305±173	122±64	119±63	1043±31	-149.7± 1.7	0.36±0.38
		476±425	91±80	387±339	1412±170	-160.1± 6.8	0.053±0.093
0316+413	B	474±59	394±38	46±4	3.7±0.72
		224±109	188±70	62±23	390±12	-177.4± 1.7	0.97±0.73
		272±130	152±63	275±114	853±57	-161.6± 3.8	0.06±0.05
		362±289	128±96	579±435	2729±218	-165.9± 4.6	0.018±0.027
0316+413	C	599±129	351±65	62±12	2.6±0.97
		138±40	125±27	28±6	250±3	160.4± 0.7	2.9±1.3
		207±111	90±44	144±71	505±35	168.7± 4.0	0.17±0.16
		44±44	51±33	< 64	749±21	-159.4± 1.6	> 0.18
		51±48	55±35	< 58	1052±19	-143.3± 1.0	> 0.25
0333+321	A	384±135	282±80	32±9	14±7.9
		208±169	88±66	56±42	72±21	-75.5±16.2	2.5±3.7
		147±153	58±56	72±70	144±35	-89.2±13.6	1.1±2
0336-019	A	832±138	499±71	67±10	5.6±1.6
		477±141	308±77	59±15	199±7	89.8± 2.1	4.2±2.1
		706±177	281±65	130±30	1011±15	58.9± 0.9	1.3±0.59
0355+508	A	1184±776	637±368	82±47	2.9±3.4
		239±251	277±190	< 60	152±21	66.3± 7.7	> 1.1
		415±236	440±172	< 32	248±6	136.4± 1.4	> 6.8
		209±251	249±192	< 70	363±27	49.1± 4.3	> 0.7
0355+508	C	2953±831	2557±544	63±13	12±5.2
		1064±629	769±368	173±83	370±41	89.8± 6.4	0.58±0.56
0415+379	B	1307±922	556±361	65±42	5.3±6.9
		374±264	198±123	87±54	272±27	74.3± 5.7	0.85±1.1
		147±205	161±152	119±112	1652±56	52.3± 1.9	0.18±0.36
0415+379	C	1104±741	455±282	68±42	4.1±5.1
		425±159	229±75	62±20	93±10	78.8± 6.3	1.9±1.3
0420+022	C	230±68	173±41	43±10	6.7±3.2
0420-014	B	1332±493	902±276	47±14	19±12
		156±137	177±103	< 86	799±25	-167.9± 1.8	> 0.66
0422+004	B	629±416	426±233	< 49	> 5.6
0430+052	B	805±279	526±153	42±12	7.7±4.5
		227±14	215±10	11±0	148±0	-114.8± 0.1	32±2.8
		747±231	322±91	77±22	294±11	-112.2± 2.1	2.1±1.2
		563±172	240±68	80±23	567±11	-112.6± 1.1	1.5±0.84

Table 7—Continued

Name (1)	Obs (2)	S_{tot} (3)	S_{peak} (4)	d (5)	r (6)	θ (7)	T_b (8)
0430+052	C	573±221	246±87	87±31	866±15	-115.2± 1.0	1.3±0.91
		1027±856	252±204	218±176	1176±88	-120.1± 4.3	0.37±0.59
		668±157	566±101	34±6	9.8±3.5
		331±137	224±77	91±31	67±16	-116.8±13.1	0.68±0.47
		96±87	113±66	< 113	664±33	-108.7± 2.9	> 0.13
		148±71	109±42	100±38	1374±19	-118.0± 0.8	0.25±0.19
0440-003	C	77±85	106±68	148±96	2645±48	-121.6± 1.0	0.06±0.083
		364±162	330±109	< 46	> 5.2
0458-020	B	62±54	70±40	< 98	309±28	-175.5± 5.2	> 0.2
		501±85	370±50	47±6	12±3.3
0521-365	C	331±27	303±18	79±5	0.92±0.11
0528+134	A	510±219	405±136	< 32	> 25
		268±103	160±53	58±19	98±10	120.5± 5.6	4±2.7
		85±23	87±16	< 23	217±2	70.0± 0.6	> 8
		114±69	73±37	69±35	815±18	35.7± 1.2	1.2±1.2
		259±51	260±36	< 27	> 13
		480±52	362±31	35±3	22±3.7
0529+075	A	128±37	102±23	26±6	48±3	68.9± 3.5	10±4.7
		127±80	57±33	85±49	224±25	112.0± 6.2	0.97±1.1
		965±137	814±88	85±9	2.9±0.63
		132±39	117±26	56±13	340±6	-53.1± 1.1	0.92±0.41
0642+449	B	42±49	65±41	< 270	399±85	72.6±12.0	> 0.013
		590±95	352±49	52±7	16±4.4
		585±180	164±49	290±86	173±43	98.4±13.9	0.5±0.3
0707+476	C	119±69	57±30	154±80	1197±40	87.6± 1.9	0.36±0.38
		83±9	72±6	21±2	7.1±1.1
		545±276	398±163	34±14	7.7±6.4
0716+714	B	1048±304	872±195	22±5	36±16
0727-115	B	640±66	573±44	142±11	1.4±0.21
0735+178	B	264±66	98±23	92±22	0.73±0.34
		142±40	108±24	31±7	107±3	88.8± 1.9	3.5±1.6
		103±35	60±18	50±15	267±7	78.3± 1.6	0.96±0.57
		121±54	55±22	77±31	435±16	29.3± 2.1	0.48±0.39
		122±27	56±11	71±14	698±7	43.5± 0.6	0.57±0.22
		832±352	589±203	40±14	10±7
0736+017	A	387±129	232±66	60±17	129±9	-94.6± 3.8	2.1±1.2
		329±144	215±79	50±18	200±9	-92.2± 2.6	2.6±1.9
		160±190	119±114	124±118	413±59	-67.2± 8.2	0.2±0.4
		426±207	262±108	58±24	3.4±2.8
0738+313	C	44±37	48±27	< 69	801±20	-167.6± 1.4	> 0.25
		571±138	496±90	23±4	33±12
		430±135	258±70	47±13	237±6	77.4± 1.5	6±3.3
0804+499	C	179±73	112±39	42±15	489±7	77.5± 0.8	3.1±2.2
		140±38	113±24	30±6	6.2±2.6
		311±98	171±47	58±16	2.3±1.3

Table 7—Continued

Name (1)	Obs (2)	S_{tot} (3)	S_{peak} (4)	d (5)	r (6)	θ (7)	T_b (8)
0823+033	A	374±161	211±79	43±16	5±3.8
		262±204	57±43	100±76	69±38	87.1±28.9	0.65±0.99
0827+243	B	598±222	557±151	< 30	> 21
0836+710	C	583±508	375±275	< 42	> 17
0850+581	C	104±30	77±18	35±8	3.2±1.5
0851+202	B	618±186	533±121	26±6	20±9
		150±118	116±72	144±89	1054±45	-118.5± 2.4	0.16±0.2
0859+470	C	222±59	180±37	27±6	12±5.1
		91±47	42±19	64±30	652±15	9.4± 1.3	0.9±0.84
0906+015	B	670±345	489±204	< 40	> 14
0917+624	A	135±68	114±44	37±14	4±3.1
0945+408	A	363±49	239±27	52±6	5±1.1
		246±175	139±86	118±73	852±36	159.2± 2.4	0.65±0.81
0954+658	A	325±187	282±122	< 28	> 9.5
		223±134	174±82	32±15	96±8	-80.2± 4.5	4.9±4.7
		96±70	69±41	78±46	665±23	-60.1± 2.0	0.35±0.42
1012+232	B	305±75	188±39	46±10	3.7±1.6
		239±65	109±27	65±16	324±8	100.4± 1.4	1.5±0.72
		112±43	42±15	86±31	593±15	118.3± 1.5	0.39±0.28
1044+719	B	204±96	180±63	< 30	> 8.3
1101+384	C	264±154	159±79	45±22	2.2±2.2
		46±25	26±12	71±33	1052±17	-80.6± 0.9	0.15±0.14
1128+385	C	504±266	273±127	53±25	8.1±7.5
		44±47	60±38	< 75	208±24	-156.9± 6.5	> 0.35
1150+497	C	455±165	376±105	27±8	14±7.7
		69±36	76±26	< 41	135±7	-155.7± 3.0	> 0.9
		78±52	63±33	79±41	651±21	-129.7± 1.8	0.27±0.29
1156+295	A	1629±388	919±191	42±9	26±11
		1143±379	517±156	49±15	79±7	66.7± 5.4	14±8.2
		177±143	191±105	< 45	88±12	11.1± 7.9	> 2.5
1219+285	C	155±22	107±12	37±4	2±0.48
		37±17	23±9	45±17	168±9	125.3± 2.9	0.33±0.25
1226+023	A	828±435	584±251	43±18	8.5±7.4
		698±404	291±155	141±75	121±38	-92.2±17.3	0.67±0.71
		377±300	279±178	107±68	420±34	54.0± 4.7	0.63±0.81
1228+126	A	1046±254	624±130	99±21	1.8±0.74
1253−055	C	5615±2493	4453±1549	< 40	> 89
1308+326	A	640±219	482±132	34±9	18±9.9
		106±41	86±26	36±11	336±5	-79.0± 0.9	2.7±1.6
1502+106	C	360±102	312±67	< 25	> 27
		77±25	61±15	43±11	519±5	127.2± 0.6	1.9±0.99
		92±57	52±28	148±81	1432±40	135.4± 1.6	0.2±0.21
1508−055	C	503±153	318±82	63±16	4.6±2.4
		270±201	207±122	67±40	776±20	88.6± 1.5	2.2±2.6
		199±171	154±105	80±54	1332±27	59.9± 1.2	1.1±1.5

Table 7—Continued

Name (1)	Obs (2)	S_{tot} (3)	S_{peak} (4)	d (5)	r (6)	θ (7)	T_b (8)
1510–089	C	668±414	538±260	< 46	> 7
		483±141	239±63	64±17	695±8	-6.4± 0.7	2.6±1.4
1511–100	C	336±84	271±52	31±6	14±5.6
		246±101	142±51	54±19	293±10	89.0± 1.9	3.5±2.5
1546+027	C	306±246	228±147	< 58	> 2.1
		223±111	142±60	46±19	333±10	-176.7± 1.7	2.4±2.1
1548+056	C	367±177	270±105	< 38	> 10
		241±130	168±74	59±26	1201±13	1.9± 0.6	2.8±2.4
1606+106	C	342±103	345±73	< 29	> 15
1637+574	C	1145±323	777±181	32±7	32±15
		148±56	119±35	29±9	58±4	-123.3± 4.2	5.1±3
		53±51	66±39	< 43	142±13	-146.7± 5.2	> 0.81
1642+690	C	597±396	389±216	33±18	16±18
1652+398	A	283±50	152±24	188±30	0.14±0.043
1655+077	C	459±157	337±93	35±10	10±5.5
		43±41	45±29	< 80	211±26	-26.1± 7.1	> 0.18
1739+522	C	979±292	688±168	29±7	45±22
		130±60	133±43	< 19	48±3	41.7± 3.7	> 14
1741–038	C	2404±860	868±292	66±22	19±13
		656±550	218±173	92±73	210±37	-122.9± 9.9	2.6±4.2
1749+096	C	2375±510	1977±326	29±5	61±20
1800+440	B	432±84	376±55	26±4	17±5.2
		57±53	72±42	< 60	101±17	-88.4± 9.7	> 0.43
1803+784	C	785±306	324±117	52±19	8±5.8
		296±371	47±58	92±114	132±57	-135.3±23.3	0.97±2.4
1807+698	A	218±66	228±48	< 19	> 10
1823+568	A	485±202	380±124	31±10	14±9.1
		212±97	118±47	111±44	503±22	-157.2± 2.5	0.47±0.38
		334±181	121±62	189±96	1129±48	-168.4± 2.4	0.26±0.26
		295±159	116±58	141±71	1551±35	-171.2± 1.3	0.41±0.41
1828+487	A	1183±331	708±170	112±27	2.6±1.3
		232±127	225±89	51±20	963±10	-55.1± 0.6	2.5±2
		952±571	333±189	210±119	3982±59	-31.4± 0.9	0.6±0.68
1842+681	A	204±94	158±57	30±11	5.5±4
		83±30	65±19	42±12	135±6	117.5± 2.6	1.1±0.66
1901+319	C	212±63	188±42	42±9	3.2±1.4
		59±36	44±21	232±113	1164±57	114.2± 2.8	0.029±0.029
1921–293	A	2069±549	1594±335	108±23	3.9±1.7
		328±234	272±150	214±118	1030±59	-12.0± 3.3	0.16±0.18
		313±230	264±148	250±140	1088±70	-37.3± 3.7	0.11±0.13
1923+210	B	574±160	415±94	41±9	5.6±2.5
		387±181	176±75	150±64	186±32	-114.7± 9.7	0.28±0.24
1928+738	A	349±137	256±81	40±13	4.7±3
		149±48	106±28	46±12	56±6	-6.7± 6.1	1.5±0.79
1928+738	C	656±395	461±227	51±25	5.4±5.4

Table 7—Continued

Name (1)	Obs (2)	S_{tot} (3)	S_{peak} (4)	d (5)	r (6)	θ (7)	T_b (8)
		618±554	264±218	166±137	1037±68	140.8± 3.8	0.48±0.79
1954+513	C	279±123	279±87	24±7	18±11
1957+405	C	178±65	144±41	33±9	2.8±1.6
2007+777	A	195±49	196±35	< 11	> 37
		108±85	48±34	76±54	71±27	-77.7±21.0	0.41±0.59
2013+370	B	1252±213	1005±133	34±5	18±4.7
		307±123	256±79	40±12	195±6	176.4± 1.8	3.2±1.9
2023+336	B	579±157	507±104	43±9	6.3±2.6
		176±87	154±57	89±33	294±17	-15.9± 3.2	0.44±0.33
2037+511	B	345±48	316±32	19±2	42±8.6
		116±88	90±54	69±41	152±21	-134.0± 7.7	1.1±1.3
2121+053	A	414±159	230±77	48±16	8.7±5.9
2128−123	A	237±23	212±15	158±11	0.23±0.034
		66±61	72±45	353±222	1210±111	26.9± 5.2	0.013±0.017
2134+004	A	220±147	184±94	< 48	> 4.6
2155−152	B	293±65	254±42	64±11	2±0.66
		104±33	66±18	168±46	720±23	35.1± 1.8	0.1±0.055
2200+420	A	1137±83	1136±58	< 6	> 550
		168±80	154±54	< 37	159±7	-138.8± 2.4	> 2.1
2201+315	A	817±349	700±227	59±19	5±3.3
		341±268	127±94	242±178	258±89	63.4±19.1	0.12±0.18
2216−038	B	458±72	407±48	157±19	0.58±0.14
2223−052	B	642±129	395±67	59±10	7.3±2.5
		283±87	205±51	47±12	347±6	146.6± 1.0	5.1±2.5
		183±75	111±39	65±23	480±11	146.8± 1.4	1.7±1.2
		139±80	66±34	72±37	736±19	91.2± 1.5	1.1±1.1
2234+282	A	405±179	278±101	52±19	4.4±3.2
2251+158	A	696±332	764±246	< 41	> 13
		138±145	189±117	< 97	105±30	-116.5±16.0	> 0.45
		238±159	267±119	< 57	247±13	-100.2± 2.9	> 2.2
		275±207	268±145	< 60	339±16	-105.2± 2.7	> 2.3
		124±167	172±135	< 131	618±52	-105.6± 4.8	> 0.22
		354±308	214±159	193±143	2323±72	-97.4± 1.8	0.29±0.43
2255−282	A	1868±330	1470±204	171±24	2±0.56
2255−282	B	993±403	981±283	< 77	> 5.3
2345−167	B	365±112	294±70	288±69	0.11±0.054
		59±57	79±46	< 512	1259±148	121.7± 6.7	> 0.0058

Note. — Column designation: 1 - source name; 2 - observing epoch: **A** - October 2001; **B** - April 2002; **C** - October 2002; 3 - model flux density of the component [mJy]; 4 - peak brightness of individual component measured in the image [mJy/beam]; 5 - size [μas]: italic numbers indicate upper limits; 6 - radius [μas]; 7 - position angle [°]; 8 - measured brightness temperature [$\times 10^{10}\text{K}$]: italic numbers indicate lower limits.

Table 8. Statistics of IDV- and non IDV-selected sources

Sample	Number	S_L [Jy]		S_L/S_S		$S_{\text{core}}/S_{\text{CLEAN}}$	
		Mean	Median	Mean	Median	Mean	Median
IDV	26	0.36 ± 0.06	0.26	0.53 ± 0.08	0.46	0.75 ± 0.04	0.78
non-IDV	83	0.31 ± 0.04	0.21	0.51 ± 0.04	0.44	0.76 ± 0.03	0.75
Sample	Number	S_{core} [Jy]		d_{core} [mas]		$\log(T_b$ [K])	
		Mean	Median	Mean	Median	Mean	Median
IDV	26	0.70 ± 0.11	0.42	0.039 ± 0.004	0.035	11.1 ± 0.1	11.1
non-IDV	83	0.62 ± 0.08	0.46	0.057 ± 0.005	0.043	10.8 ± 0.1	10.8

Note. — Each mean value is presented with its corresponding $1-\sigma$ error, assuming a normal distribution.